Study on Thermoelectric Properties of N-type Half-Heusler Compounds

---

A Dissertation Presented to

the Faculty of the Department of Chemistry

University of Houston

In Partial Fulfillment

of the Requirements for the Degree

Doctor of Philosophy

By

Hao Zhang

December 2016

Study on Thermoelectric Properties of N-type Half-Heusler Compounds

Hao Zhang

Prof. Zhifeng Ren

Department of Physics

Prof. Allan Jacobson

Department of Chemistry

Prof. Arnold Guloy

Department of Chemistry

Prof. Vassiliy Lubchenko

Department of Chemistry

Prof. Shuo Chen

Department of Physics

Dean, College of Natural Sciences and Mathematics

Acknowledgements

I am using this opportunity to express my gratitude to all the people who helped, supported and inspired me during my Ph.D study. First of all, I am extremely indebted to my research advisor, Prof. Zhifeng Ren who guided me with patience, enthusiasm, encouragement, and immense knowledge throughout the period of my doctoral work. He is absolutely all one can ask for as a mentor, not only because of his borderless knowledge that enlightens me all the time, but also the way he treats us with kindness, respect, and trust.

I would also like to express my sincere thanks to my dissertation committee members Prof. Allan Jacobson, Prof. Arnold Guloy, Prof. Vassiliy Lubchenko, and Prof. Shuo Chen who provided me with valuable suggestions and continuous supports. I would especially like to thank Prof. Shuo Chen for the instruction and guidance in the beginning of my research and helpful advice and discussions afterwards.

My sincere gratitude is also given to all the group members for providing a stimulating and friendly environment in which to learn and grow. I am thankful to Dr. Qian Zhang, Dr. Weishu Liu, Dr. Qing Jie, and Dr. Yumei Wang for their fruitful discussions and valuable suggestions to my researches. I would also like to thank Dr. Dezhi Wang, Mr. Jun Mao, Mr. Keshab Dahal, Mr. Zihang Liu, Ms. Jing Shuai, Ms. Yuan Liu, Mr. Ran He, Mr. Hui Wang and many others who helped me through daily research in every aspect along the way.

Last but not least, I am deeply grateful to my parents for their dedication and unconditional support during my PhD study and throughout my life. It is beyond any mere words could say about how much I owe to my beloved parents.

Study on Thermoelectric Properties of N-type Half-Heusler Compounds

---

An Abstract of a Dissertation

Presented to

the Faculty of the Department of Chemistry

University of Houston

In Partial Fulfillment

of the Requirements for the Degree

Doctor of Philosophy

By

Hao Zhang

December 2016

Abstract

Thermoelectric materials have been attracting intensive attentions for the ability of directly converting heat into electricity and vice versa, which can be potentially applied to waste-heat recovery and solid-state cooling. Among the various thermoelectric materials, half-Heusler compounds stand out for their high thermal stability, good mechanical strength, and low toxicity. In this dissertation, focus is placed on the n-type half-Heusler compounds. A series of experimental studies on the thermoelectric properties of n-type half-Heuslers are discussed, the goals of which consist of two aspects: (1) improving the thermoelectric properties of the conventional MNiSn (M refers to Hf, Zr, Ti or their combination) based n-type half-Heulsers; (2) exploring the thermoelectric properties of other unconventional half-Heulser compositions to search for new potential candidates for thermoelectric applications.

Three strategies are employed to improve the thermoelectric properties of the nanostructured half-Heusler $Hf_{0.25}Zr_{0.75}NiSn$. First, doping with adjacent elements to optimize the electrical properties is carried out. Different from the conventional Sb doping at the Sn site which may be not stable at high temperatures due to the high vapor pressure of Sb, Nb, V, and Ta doping at the Hf/Zr site is studied. Enhanced thermoelectric performance is achieved. Second, alloy effects have long been used as an effective approach to reduce the thermal conductivity. Thus the effects of further alloying Ti at the Zr site in $Hf_{0.25}Zr_{0.75}NiSn$ are studied. Finally, incorporating nanoinclusions is another way to improve the thermoelectric properties of a material. Here, InSb

nanoinclusions are introduced into the half-Heulser matrix, and the results are discussed. Besides, the thermal stability of the $Hf_{0.25}Zr_{0.75}NiSn_{0.99}Sb_{0.01}$ sample is studied as well.

To search for unconventional half-Heusler compositions, which may possess good thermoelectric properties, the half-Heusler compound VCoSb was studied at first. With VEC = 19, VCoSb is thought to be a metal, so it's never been studied as a thermoelectric material before. Here, the thermoelectric properties of VCoSb are reported for the first time. Another two half-Heusler compounds VFeSb and YNiSb are synthesized and their thermoelectric properties are studied too. Doping in VFeSb and YNiSb is also tried to optimize their thermoelectric performance.

Table of Contents

List of Figures

Lists of Tables

Chapter 1

Introduction

The world's demand for safe, clean, and sustainable energy has evoked growing interest in the development of thermoelectric materials. Thermoelectric phenomena, which involve the direct conversion between thermal energy and electricity, can be potentially applied to either waste-heat recovery or solid-state cooling. Compared to conventional power generators and cooling devices, thermoelectric devices have advantageous features such as no moving parts or vibrations, high level of reliability, long life time without maintenance, quiet and environmentally friendly, making them potential candidates as an alternative green energy source.

Thermoelectric effects were discovered in the early 19^{th} century when Seebeck first observed the Seebeck effect in 1821 [1]. After that, the Peltier effect which can be viewed as a reverse process of the Seebeck effect was discovered [2]. The relationship between Seebeck coefficient and Peltier coefficient was provided by Thomson, who also predicted and experimentally confirmed the Thomson effect in 1851 [3]. In the next several decades, due to the lack of high-thermopower materials, the only development is the Altenkirch's derivations of thermoelectric efficiency for power generation and refrigeration in 1909 [4] and 1911 [5]. Then in the 1950s, Ioffe found that doped semiconductors exhibited much better thermoelectric performance than pure semiconductors and metals [6]. Since then, a tremendous amount of researches on alloy based semiconductor materials were done, and thermoelectric power generation became

reasonably efficient and thermoelectric refrigeration became practical. During 1960 and 1990, although the thermoelectric field received little attention from the worldwide scientific research community, the thermoelectric in industrial field still grew steadily in applications for space exploration, laboratory equipment and medical physics [7]. In these applications, the reliability, energy availability, absence of moving parts and silent operation of thermoelectric devices outweigh their relatively high cost and low efficiency.

Until then, the thermoelectics have long been too inefficient to be cost effective for wide applications. In the early 1990s, a resurgence of interest in thermoelectric researches began, which was brought by the energy crisis and environmental issues associated with traditional energy materials such as oil and coal. Two primary approaches were taken for developing the next generation of thermoelectric materials. One is the exploration and discovery of new thermoelectric materials. The materials with complex crystal structures such as containing heavy-ion rattlers at partially filled structural sites could provide effective phonon scattering to reduce thermal conductivity without affecting electronic properties [8, 9]. “Phonon-glass electron-crystal”, first introduced by Slack is the general direction for those structures [10]. The other approach is focused on the creation of materials with low dimensional features, since theoretical predictions suggested that thermoelectric efficiency could be greatly enhanced through nanostructural engineering. The introduction of nanoscale constituents would increase the power factor by quantum size effect [11, 12] and in the meantime, reduce the thermal conductivity by increasing the phonon scattering at numerous interfaces of nanostructures [13]. Large enhancement of thermoelectric performance has been observed in Bi_2Te_3/Sb_2Te_3 superlattices and PbTe/PbSeTe quantum dot superlattices [14, 15]. Despite the high thermoelectric

performance of supperlattices, the fabrication technique for superlattices is too expensive and not scalable for mass production. Detailed studies suggest that superlattice structure is not a rigid requirement. In fact, any samples with large interface densities would be good candidates [16]. The above two approaches can also be combined. New bulk thermoelectric materials with nanostructures or using bulk materials as host materials embedded with nanoinclusions is employed to improve the thermoelectric performance [17, 18].

After these developments, the demand for high-performance materials has increased for power generation and solid-state cooling. To fulfill the increasing demand, cost-effective and scalable techniques to produce thermoelectric materials with higher efficiency will be needed. In this chapter, a brief review of thermoelectric phenomena, current challenges, and thermoelectric materials especially the half-Heusler compounds will be presented.

1.1 Principles of Thermoelectric

When a temperature gradient is applied to a conductor, an electric field is created, or conversely when an electrical current passes though the conductor, a temperature gradient occurs. These are the phenomena of thermoelectric effects. The thermoelectric effects encompass three correlated effects: the Seebeck effect, Peltier effect and Thomson effect. The physical principles of these effects and fundamental parameters of thermoelectrics will be reviewed and discussed in the following sections.

1.1.1 Seebeck Effect

The Seebeck effect is the direct conversion of temperature difference into electricity. It was discovered by Thomas Johann Seebeck in1821 [1]. When two different conductors are connected together and the two junctions are exposed to different temperatures, a voltage is generated. These connected conductors have long been used as thermocouples to measure temperatures. This is also the principle of thermoelectric power generation. Although the Seebeck effect is discovered for two different materials, it also applies to any single material. As illustrated in Figure 1.1.1, when a material is subjected to a temperature gradient, the charge carriers will diffuse from the hot side to the cold side, leading to the generation of a voltage. The Seebeck coefficient S is defined as:

$$S = -\frac{dV}{dT} \tag{1.1.1}$$

Where dV is the generated Seebeck voltage and dT is the temperature difference.

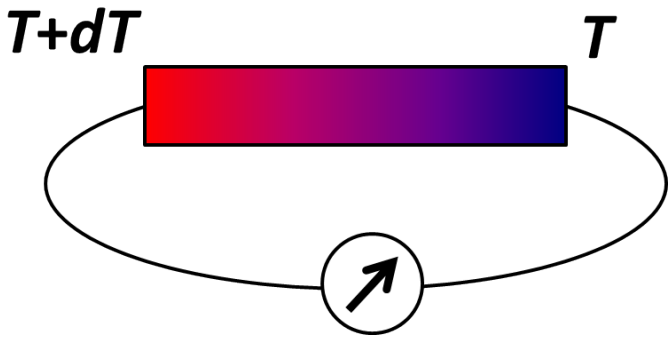

Figure 1.1.1 Illustration of Seebeck effect.

1.1.2 Peltier Effect

The Peltier effect was discovered by a French physicist Jean Charles Athanase Peltier in 1834 [2], and it can be viewed as a reverse process of the Seebeck effect. As illustrated in Figure 1.1.2, if an electric current passes through a junction consisting of two different materials, the junction is either heated or cooled depending on the direction of the current.

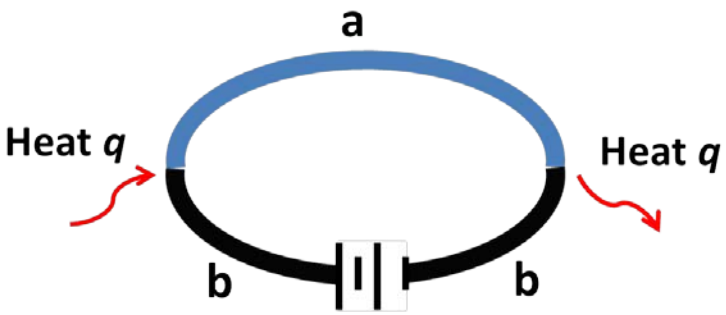

Figure 1.1.2 Peltier effect in two dissimilar materials a and b.

The Peltier coefficient π_{ab} of a pair of materials (a and b) is given by:

$$\pi_{ab} = \pi_a - \pi_b = \frac{q}{I} \tag{1.1.2}$$

Here π_a and π_b are Peltier coefficient of material a and b respectively. q is rate of heat change at the junction and I is the current flowing through the junction. The Peltier effect is a reversible process and depends on the direction of current flow. When holes are charge carriers (p-type), the heat is transported along the direction of the hole current. Similarly, when electrons are charge carries (n-type), the heat is transported along the direction of the electron current. The electrons move in the conduction band and the holes move in the valence band, both of which have energies different from the metal Fermi

energies at the junctions. As a result, the carriers either emit or absorb the energy at the junctions creating cooling or heating effects. Because heat is absorbed at one junction and emitted at another junction, the Peltier effect can be applied in the thermoelectric cooling.

1.1.3 Thomson Effect

The Thomson effect, predicted and observed by William Thomson in 1851, describes the heating or cooling of a current-carrying conductor with a temperature gradient [3]. When a current I pass through a homogeneous conductor, the rate of heat change per unit volume is:

$$q = -\beta I \Delta T \tag{1.1.3}$$

Where β is the Thomson coefficient, ΔT is the temperature gradient. The Thomson coefficient has the same unit as those of Seebeck coefficient. This equation neglects Joule heating and ordinary thermal conductivity.

1.1.4 The Kelvin Relationships

The above three thermoelectric coefficients: Seebeck coefficient (S), Peltier coefficient (π), and Thomson coefficient (β) are related to each other by the Kelvin relations [3]:

$$\pi = S \cdot T \tag{1.1.4}$$

$$\beta = T \frac{dS}{dT} \tag{1.1.5}$$

here T is the absolute temperature of the material.

1.2 Thermoelectric Device and Efficiency

Based on Seebeck effect and Peltier effect, thermoelectric materials can be made into devices for power generation and refrigeration respectively [7]. The basic component of thermoelectric device is the module, which consists of a pair of n-type and p-type legs, as illustrated in Figure 1.2.1. For power generation, one side of the module is heated, and the electrons of the n-type leg and the holes of the p-type leg will then diffuse from the hot side to the cold side, generating the output power. On the other side, when driven by an electrical current, the electrons and holes will bring heat from one side to the other side, resulting in Peltier cooling.

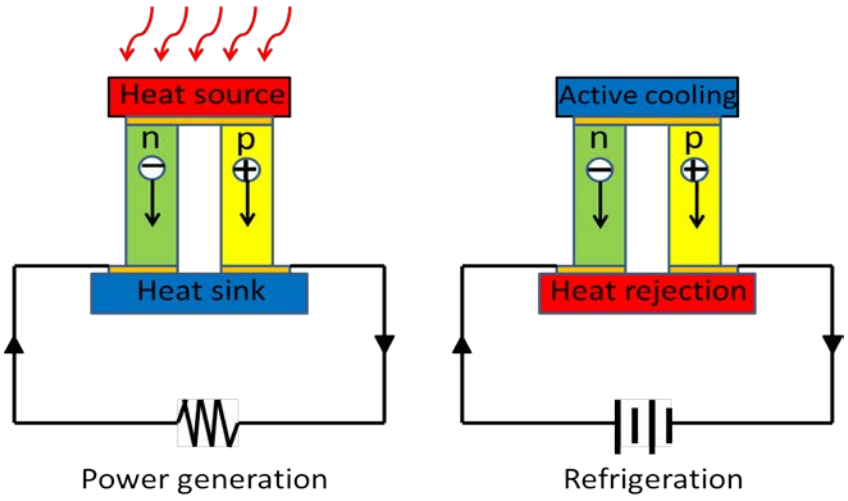

Figure 1.2.1 Thermoelectric power generation and refrigeration.

The power generation of thermoelectric device is a thermodynamic process, so the upper limit of its conversion efficiency is the Carnot efficiency [19, 20]. If there are no heat losses, the efficiency η is defined as the ratio of the electrical power delivered to the load to the heat absorbed at the hot junction.

$$\eta = \frac{w}{q} = \frac{I^2 R_L}{K(T_H - T_c) + SIT_H} \tag{1.2.1}$$

R_L is the resistance of the load, K is the thermal conductance, and T_H and Tc are the hot side and cold side temperature respectively. The efficiency varies with the resistance of the load. In 1957, Ioffe showed that the maximum efficiency is given by

$$\eta = \frac{(T_H - T_C)}{T_H} \frac{(1 + ZT)^{1/2} - 1}{(1 + ZT)^{1/2} + T_C/T_H} \tag{1.2.2}$$

Where

$$ZT = \frac{S^2 \sigma T}{\kappa} \tag{1.2.3}$$

ZT is called the thermoelectric figure of merit, in which S is the Seebeck coefficient, σ is the electrical conductivity, and κ is the thermal conductivity.

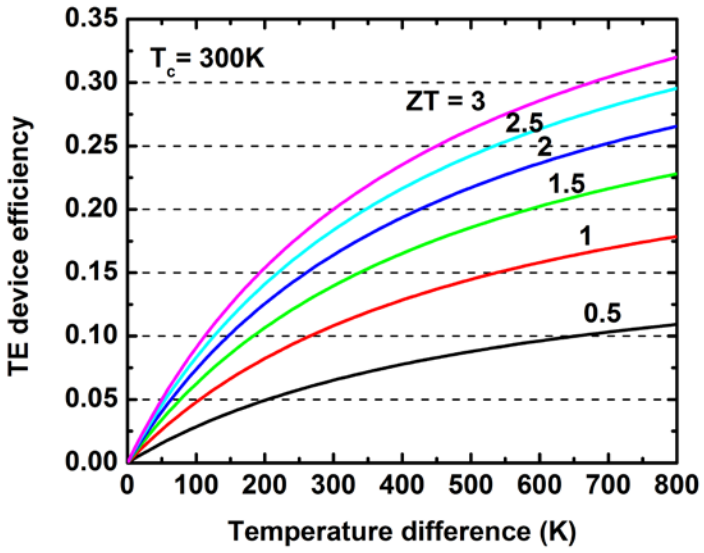

Figure 1.2.2 Efficiency of ideal thermoelectric power generation devices with different ZT values, as a function of the temperature gradient across the device.

A higher ZT value will lead to higher efficiency, as shown in Figure 1.2.2. The efficiency of the thermoelectric generator equals the Carnot efficiency only when ZT goes to infinity.

The efficiency of a thermoelectric refrigerator is given by the coefficient of performance (COP), which is defined as the cooling power produced divided by the input electrical energy:

$$\varphi = \frac{q}{w} \tag{1.2.4}$$

Where

$$q = ST_C I - \frac{1}{2} I^2 R - K(T_H - T_c) \tag{1.2.5}$$

$$w = S(T_H - T_C)I + I^2 R \tag{1.2.6}$$

The optimized COP with respect to electrical current is,

$$\varphi = \frac{T_C[(1+ZT)^{1/2} - T_H/T_C]}{(T_H - T_C)[(1+ZT)^{1/2} + 1]} \tag{1.2.7}$$

It shows that the COP of a refrigerator also depends on the figure of merit ZT, where a higher ZT leads to a better performance. For Peltier cooling purpose, another important quantity is the maximum temperature difference that can be achieved when the thermal load is zero. It is found that,

$$\Delta T_{max} = \frac{ZT_C{}^2}{2} \tag{1.2.8}$$

1.3 Thermoelectric Figure of Merit

As mentioned above, both the efficiency of power generation and coefficient of performance of cooling directly depend on ZT. Higher ZT will always contribute to a higher efficiency or better performance. Therefore, high ZT values are indicative of good thermoelectric materials. As shown in equation (1.2.3), ZT is proportional to the square of the Seebeck coefficient because the efficiency is proportional to the amount of power generated and the power is proportional to the square of the voltage created by the Seebeck effect. Also, ZT is proportional to electrical conductivity because high electrical conductivity reduces energy leakage by Joule heating within the material. In *ZT*, the $S^2\sigma$ is defined as power factor,

$$PF = S^2\sigma \tag{1.3.1}$$

The power factor is related to the power generation of a material, a large power factor represents a high power output.

On the other hand, ZT is inversely proportional to the thermal conductivity, because a high thermal conductivity enhances heat transfer through the sample, thereby preventing the temperature difference from being maintained. As a result, to achieve high ZT values, a large Seebeck coefficient, a high electrical conductivity and a low thermal conductivity are required. However, the three parameters are all interrelated to each other in bulk materials, so it is hard to independently change individual property without affecting the others. In the following sections, how the Seebeck coefficient, electrical conductivity and thermal conductivity are related to each other is discussed.

1.3.1 Carrier Concentration

The electrical conductivity (σ) is related to the carrier concentration (n) through the carrier mobility (μ):

$$\sigma = ne\mu \tag{1.3.2}$$

An increase of carrier concentration will lead to an increased electrical conductivity. On the other hand, in the kinetic definition, the Seebeck coefficient represents the energy difference between the average energy of carrier and the Fermi energy [21]. Increasing carrier concentration causes a simultaneous increase in Fermi energy as well as average energy of carriers. However, the Fermi energy will increase much faster than the average energy of carriers, resulting in a decrease in Seebeck coefficient. For metals or degenerate semiconductors (parabolic band, energy-independent scattering approximation) the Seebeck coefficient is given by,

$$S = \frac{8\pi^2 {k_B}^2}{3eh^2} m^* T \left(\frac{\pi}{3n}\right)^{\frac{2}{3}} \tag{1.3.3}$$

Where m^* is the effective mass of the carrier [22]. It clearly shows the relationship of Seebeck coefficient and carrier concentration.

The change of carrier concentration affects the thermal conductivity as well. The total thermal conductivity κ is the sum of the lattice thermal conductivity κ_l and the electronic thermal conductivity κ_e from the charge carriers.

$$\kappa = \kappa_l + \kappa_e \tag{1.3.4}$$

The electronic thermal conductivity κ_e is related to the electrical conductivity through the Wiedemann-Franz law,

$$\kappa_e = L\sigma T = ne\mu LT \tag{1.3.5}$$

where L is the Lorenz factor. Thus the increase of carrier concentration will also cause increased electronic thermal conductivity. Therefore, the compromise between large Seebeck coefficient, high electrical conductivity and low thermal conductivity in thermoelectric materials must be made to maximize the figure of merit ZT. Figure 1.3.1 summaries how these parameters are related to the carrier concentration [23]. The peak ZT is achieved at the carrier concentration between 10^{19} and 10^{20} per cm^3, so good thermoelectric materials are typically heavily doped semiconductors.

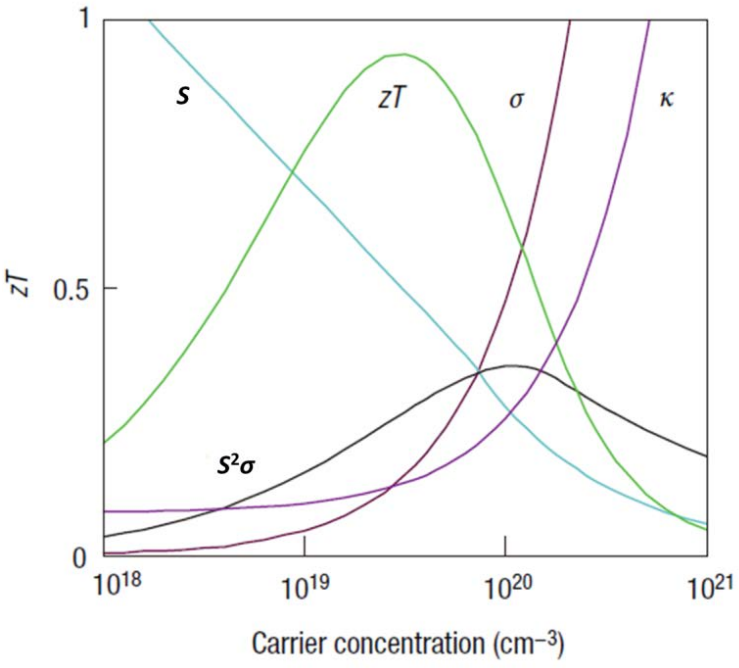

Figure 1.3.1 Optimizing ZT by tuning carrier concentration [23].

1.3.2 Effective Mass

As shown in equation (1.3.3), a large effective mass m^* of charge carriers gives rise to a high Seebeck coefficient. However, materials with large effective mass always have low carrier mobility which in turn results in low electrical conductivity. Large effective mass m^* is related to heavy carriers, which will move with slower velocities, resulting in smaller mobility. Although the exact relationship between effective mass and carrier mobility is complicated, a trade-off between high effective mass and high mobility must be made to get an optimized ZT. There are no certain criteria of the two parameters, because good thermoelectric materials can be found in a wide range of effective masses and mobility, such as low-mobility, high-effective-mass polaron conductors (oxides [24], chalcogenides [25]), and high-mobility, low-effective-mass semiconductors (SiGe [26], GaAs [27]). In some cases, the relationship of effective mass and mobility could be decoupled by introducing new carrier-scattering mechanisms or by producing anisotropic crystal structures in certain types of thermoelectric materials [7].

1.3.3 Lattice Thermal Conductivity

A low lattice thermal conductivity is favorable for a high ZT. However, most of the strategies to reduce lattice thermal conductivity such as introducing more defects and increasing grain boundaries, will deteriorate the electrical conductivity at the same time, because these methods not only increase the phonon scattering but also the scattering of electrons resulting in a reduced carrier mobility. Glasses exhibit the lowest lattice thermal conductivities, but they are not suitable for thermoelectric applications, because of the bad electrical transport properties.

Good thermoelectric materials therefore require the structure of “phonon-glass electron-crystal” (PGEC), since crystalline semiconductors can best meet the compromises required from the electrical properties and glasses possess low lattice thermal conductivities [10]. In such PGEC materials, high-mobility electrons are free to transport charge but the phonons are disrupted at the atomic scale from transporting heat. In fact, PGEC is the general concept for designing good thermoelectric materials.

1.4 Thermoelectric Materials

Thermoelectric materials consist of different material systems. There are some general rules of selecting good thermoelectric materials. First of all, as explained above, good thermoelectric materials are usually heavily doped semiconductors with carrier concentrations between 10^{19} and 10^{20} per cm^3. Besides, a decent band gap is important, because narrow band gap can lead to high carrier mobility, but on the other hand the band gap should be large enough to suppress the excitation of minority charge carriers. Low electronegativity difference between elements is favorable for high carrier mobility. Also, more symmetrical crystal structures tend to have better electrical properties as multi-valley band structures could contribute to high Seebeck coefficient. To get a low thermal conductivity, elements with large atomic weight and complex structures with large number of atoms in the unit cell are necessary. Based on these criteria, several materials stand out for their good thermoelectric performance in different temperature ranges.

For near-room-temperature applications, bismuth telluride (Bi_2Te_3) based alloys with a lamellar structure perpendicular to the c-axis have been proven to be superior to other materials. For the most commonly studied p-type compositions $Bi_xSb_{2-x}Te_3$, the peak ZT

values can reach up to 1.4-1.5, and maximum ZT of the n-type $Bi_2Te_{3-x}Se_x$ is around 1 [28, 29]. By adjusting the carrier concentration, ZT can be optimized to peak at different temperatures. Both the n-type and the p-type Bi_2Te_3 based alloys can be used in applications such as refrigeration and waste-heat recovery up to 200 °C.

PbTe and its alloys are widely studied for their high thermoelectric performance in the mid-temperature ranges (500 K to 900 K). Since the first study of this material for thermoelectric applications in 1957, a lot of efforts have been put into optimizing the performance, since PbTe has a high mean atomic weight and a multi-valley band structure, which can provide a large Seebeck coefficient in excess of 300 $\mu V\ K^{-1}$. Nowadays both n-type and p-type PbTe alloys can get ZT greater than 1 [30, 31].

In the mid-temperature region, skutterudites are also prospective candidates for achieving figure of merit above 1. Skutterudites, with a general formula MX_3 (M=Co, Rh, Ir; X=P, As, Sb), attract wide attention from thermoelectric researchers due to the large voids in their structure which can be filled with filler atoms to reduce thermal conductivity [32]. Skutterudites are the very first good demonstration of the PGEC structure.

Silicon germanium is proven to be good thermoelectric material for temperature ranges above 900 K [33]. Although ZT values for SiGe materials are not that high because of the relatively high lattice thermal conductivity of the diamond structure, SiGe based thermoelectric modules have been extensively used in the radioisotope thermoelectric power generators for space missions.

More examples of emerging thermoelectric compound include clatherates, Zintl phases, Mg_2Si, layered oxyselenide BiCuSeO, Cu_xSe or Zn_4Sb_3, Cu_xMX_y (M: Sn, Sb; X: Se, S),

and so on, all have decent ZT values and are promising for thermoelectric applications. There are also researches on oxides and organic polymers/metal-organic complexes as thermoelectrics. Figure 1.4.1 summarizes the ZT values for some of the state-of-the-art thermoelectric materials.

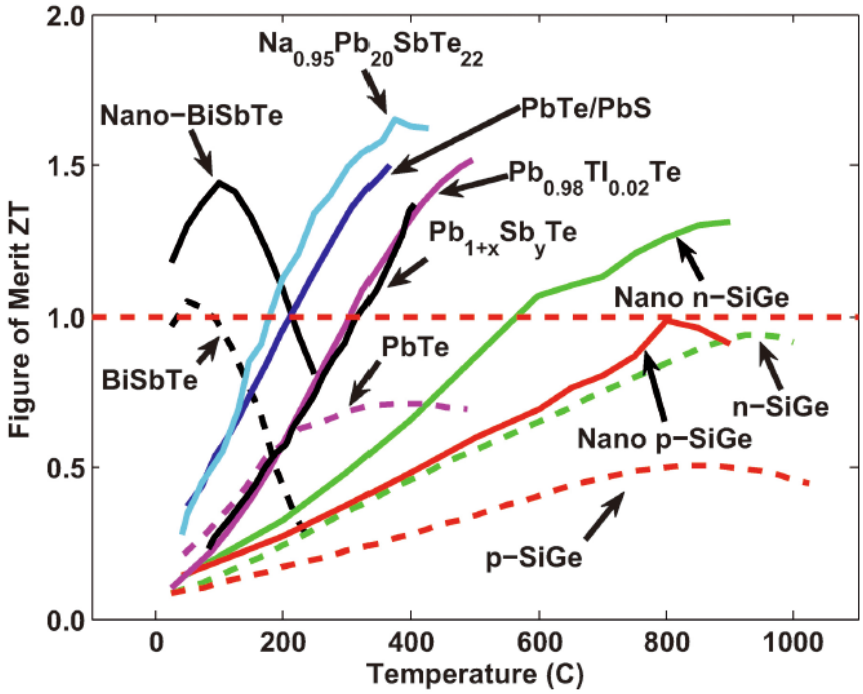

Figure 1.4.1 Figure of merit ZT of state of the art thermoelectric materials versus temperature [34].

1.5 Half-Heusler Compounds

Half-Heusler (HH) compounds have attracted intensive research interest due to their great potential applications in power generation in the middle to high temperature range from 500 °C to 800 °C, which is close to the temperature of most industrial waste heat sources. Compared to other thermoelectric materials in this temperature range, half-Heusler alloys

are competitive because of their high thermal stability, mechanical sturdiness, non-toxicity and relatively cheap price [35, 36].

Half-Heusler compounds represent a fascinating large class of intermetallic phases with general composition ABX, where A is a transition metal, a noble metal, or a rare-earth element, B is a transition metal or a noble metal, and X is a main group element. They crystallize in the MgAgAs type structure of $F\bar{4}3m$ space group. The structure of the HH is shown in Figure 1.5.1. The structure can be viewed as consisting of four interpenetrating *fcc* (face-centered cubic) sublattices of A, B, and X atoms occupying (0, 0, 0), (1/4, 1/4, 1/4), and (1/2, 1/2, 1/2) positions, respectively, leaving the (3/4, 3/4, 3/4) position empty. Upon filling the empty site (3/4, 3/4, 3/4) with an additional B atom, one directly generates the related ternary full-Heusler (FH) phase (space group Fm3m) with general composition AB_2X, which are metals.

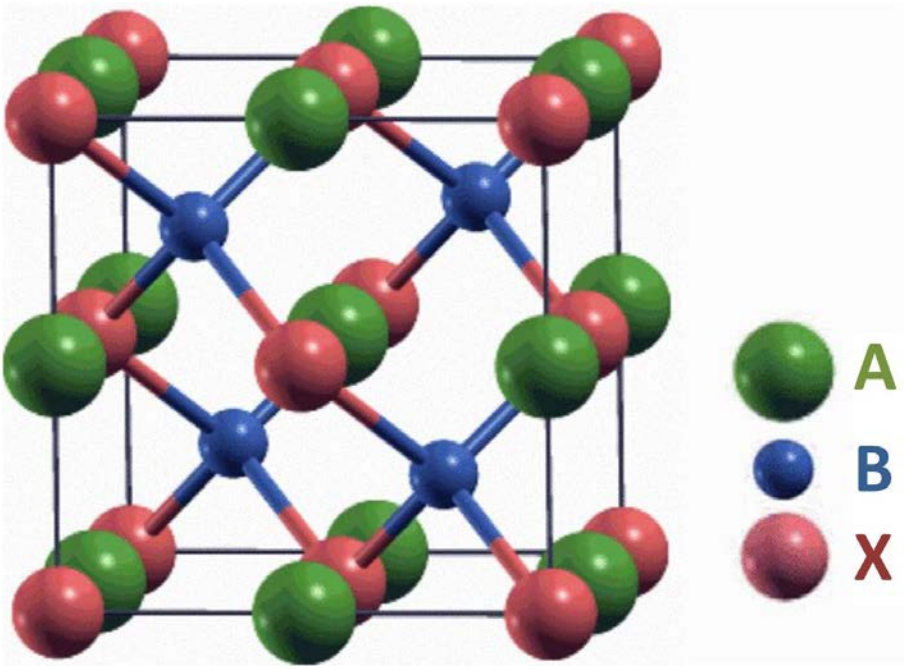

Figure 1.5.1 Crystal structure of half-Heusler compound ABX.

Half-Heusler compounds with 18 valence electron count (VEC) per unit cell are narrow-bandgap semiconductors. Theoretical studies have predicted that for half-Heusler compounds, as a consequence of the larger distance between the B atoms compared to the Heusler phase, the overlap of the d wave functions is weaker, resulting in formation of energy gaps in the density of states spectra [37, 38]. When VEC = 18, half-Heusler compounds with filled valence band and empty conduction band are semiconductors, which may be promising thermoelectric materials.

Although there are more than 100 HHs that can be found in Pearson's handbook and the Inorganic Crystal Structural Database (ICSD), and using the criterion of VEC=18 for semiconductors, there are still more than 30 HHs left [39], for the past decades, most researches have been focused on the system MCoSb (M=Ti, Zr, and Hf) for p-type and MNiSn (M=Ti, Zr, and Hf) for n-type. To enhance the thermoelectric properties, binary or ternary alloying at the A site by Hf, Zr, and Ti was widely employed to reduce the lattice thermal conductivity by introducing point defects scattering [40-42]. The carrier concentrations can be optimized by doping with the adjacent elements such as doping Sn at the Sb site for MCoSb and slightly doping Sb at the Sn site for MNiSn [43, 44]. However, due to the high lattice thermal conductivity, the ZT values of half-Heuslers remain quite low for a long time, only 0.5 at 1000 K in p-type $Hf_{0.5}Zr_{0.5}CoSb_{0.8}Sn_{0.2}$ [45] and 0.8 at 1025 K for n-type $Hf_{0.75}Zr_{0.25}NiSn_{0.975}Sb_{0.025}$ [46]. Recently, our groups managed to further improve the ZT value to 0.8 in p-type $Hf_{0.5}Zr_{0.5}CoSb_{1-x}Sn_x$ and 1.0 in n-type $Hf_{0.75}Zr_{0.25}NiSn_{1-x}Sb_x$, by the nanostructuring approach of high energy ball-milling combined with hot-pressing [47, 48]. The formation of half-Heusler nanocomposite can effectively reduce the lattice thermal conductivity by the increased grain boundary

scattering for phonons without deteriorating the electrical properties too much. Thus the thermoelectric properties can be effectively enhanced in the nanostructured half-Heulsers.

In this dissertation, the thermoelectric properties of n-type half-Heusler compounds are studied. Based on the nanostructural form, different approaches to further improve the thermoelectric performance of the conventional composition MNiSn are discussed. To optimize the electrical properties, Nb, V, and Ta doping at the Hf/Zr site in $Hf_{0.25}Zr_{0.75}NiSn$ is carried out and the results are discussed in Chapter 3. In chapter 4, further alloying Ti at the Zr site in $Hf_{0.25}Zr_{0.75}NiSn$ to reduce the thermal conductivity, and incorporating nanoinclusions into half-Heuslers have been researched respectively. Besides, the thermal stability of the $Hf_{0.25}Zr_{0.75}NiSn_{0.99}Sb_{0.01}$ sample is studied as well. On the other hand, exploring the thermoelectric properties of other half-Heulser compositions to search for new candidates for the thermoelectric applications is important too. Thus in chapter 5 and chapter 6, VCoSb, VFeSb, and YNiSb based half-Heulsers have been synthesized and their thermoelectric properties are studied.

References

[1] T. Seebeck. Magnetic polarization of metals and minerals, Abhandlungen der Deutschen Akademie der Wissenschaften zu Berlin 265 (1822) 1823.

[2] J. Peltier. Nouvelles experiences sur la caloriecete des courans electriques, Ann. Chem 56 (1834) 371-387.

[3] W. Thomson. On a Mechanical Theory of Thermo-Electric Currents, Proceedings of the Royal society of Edinburgh 3 (1857) 91-98.

[4] E. Altenkirch. Über den nutzeffekt der thermosäule, Physikalische Zeitschrift 10 (1909) 560.

[5] E. Altenkirch. Elektrothermische Kälteerzeugung und reversible elektrische Heizung, Physikalische Zeitschrift 12 (1911) 920-924.

[6] A.F. Ioffe. Semiconductor thermoelements and Thermoelectric cooling, Infosearch, ltd., 1957.

[7] D.M. Rowe. CRC handbook of thermoelectrics, CRC press, 1995.

[8] G. Nolas, D. Morelli, T.M. Tritt. Annual Review of Materials Science 29 (1999) 89-116.

[9] D. Morelli, T. Caillat, J. P. Fleurial, A. Borshchevsky, J. Vandersande, B. Chen, C. Uher. Physical Review B 51 (1995) 9622.

[10] G.A. Slack, M.A. Hussain. Journal of Applied Physics 70 (1991) 2694-2718.

[11] L. Hicks, M. Dresselhaus. Physical Review B 47 (1993) 12727.

[12] L. Hicks, M. Dresselhaus. Physical review B 47 (1993) 16631.

[13] G. Chen. Physical Review B 57 (1998) 14958.

[14] R. Venkatasubramanian, E. Siivola, T. Colpitts, B. O'quinn. Nature 413 (2001) 597-602.

[15] T. Harman, P. Taylor, M. Walsh, B. LaForge. science 297 (2002) 2229-2232.

[16] G. Chen. Semiconductors and Semimetals 71 (2001) 203-259.

[17] K.F. Hsu, S. Loo, F. Guo, W. Chen, J.S. Dyck, C. Uher, T. Hogan, E. Polychroniadis, M.G. Kanatzidis. Science 303 (2004) 818-821.

[18] J.P. Heremans, C.M. Thrush, D.T. Morelli. Physical Review B 70 (2004) 115334.

[19] T. Handbook. Macro to Nano, edited by DM Rowe, CRC Taylor & Francis, Boca Ratcon (2006).

[20] T. Tritt. Recent Trends in Thermoelectric Materials Research, Part Two, Academic Press, 2000.

[21] P. Pichanusakorn, P. Bandaru. Nanostructured thermoelectrics, Materials Science and Engineering: R: Reports 67 (2010) 19-63.

[22] M. Cutler, J. Leavy, R. Fitzpatrick. Physical Review 133 (1964) A1143.

[23] G.J. Snyder, E.S. Toberer. Complex thermoelectric materials, Nat Mater 7 (2008) 105-114.

[24] K. Koumoto, I. Terasaki, R. Funahashi. MRS Bulletin 31 (2006) 206-210.

[25] G.J. Snyder, T. Caillat, J. P. Fleurial. Physical Review B 62 (2000) 10185.

[26] X. Wang, H. Lee, Y. Lan, G. Zhu, G. Joshi, D. Wang, J. Yang, A. Muto, M. Tang, J. Klatsky. Applied Physics Letters 93 (2008) 193121.

[27] H. Ehrenreich. Physical Review 120 (1960) 1951.

[28] W. Xie, J. He, H.J. Kang, X. Tang, S. Zhu, M. Laver, S. Wang, J.R. Copley, C.M. Brown, Q. Zhang. Nano letters 10 (2010) 3283-3289.

[29] B. Poudel, Q. Hao, Y. Ma, Y. Lan, A. Minnich, B. Yu, X. Yan, D. Wang, A. Muto, D. Vashaee, X. Chen, J. Liu, M.S. Dresselhaus, G. Chen, Z. Ren. Science 320 (2008) 634-638.

[30] Y. Pei, X. Shi, A. LaLonde, H. Wang, L. Chen, G.J. Snyder. Nature 473 (2011) 66-69.

[31] Q. Zhang, F. Cao, K. Lukas, W. Liu, K. Esfarjani, C. Opeil, D. Broido, D. Parker, D.J. Singh, G. Chen, Z. Ren. Journal of the American Chemical Society 134 (2012) 17731-17738.

[32] X. Shi, J. Yang, J.R. Salvador, M. Chi, J.Y. Cho, H. Wang, S. Bai, J. Yang, W. Zhang, L. Chen. Journal of the American Chemical Society 133 (2011) 7837-7846.

[33] B. Yu, M. Zebarjadi, H. Wang, K. Lukas, H. Wang, D. Wang, C. Opeil, M. Dresselhaus, G. Chen, Z. Ren. Nano Letters 12 (2012) 2077-2082.

[34] A. Minnich, M. Dresselhaus, Z. Ren, G. Chen. Energy & Environmental Science 2 (2009) 466-479.

[35] S. Chen, Z. Ren. Materials Today 16 (2013) 387-395.

[36] T. Zhu, C. Fu, H. Xie, Y. Liu, X. Zhao. Advanced Energy Materials 5 (2015).

[37] J. Tobola, J. Pierre, S. Kaprzyk, R.V. Skolozdra, M.A. Kouacou. Journal of Physics: Condensed Matter 10 (1998) 1013.

[38] J. Toboła, J. Pierre. Journal of Alloys and Compounds 296 (2000) 243-252.

[39] J. Yang, H. Li, T. Wu, W. Zhang, L. Chen, J. Yang. Advanced Functional Materials 18 (2008) 2880-2888.

[40] C. Yu, T.J. Zhu, R.Z. Shi, Y. Zhang, X.B. Zhao, J. He. Acta Materialia 57 (2009) 2757-2764.

[41] G. Joshi, T. Dahal, S. Chen, H. Wang, J. Shiomi, G. Chen, Z. Ren. Nano Energy 2 (2013) 82-87.

[42] S. Chen, K.C. Lukas, W. Liu, C.P. Opeil, G. Chen, Z. Ren. Advanced Energy Materials 3 (2013) 1210-1214.

[43] H. Heinrich, P.R. Art, G. Claudia, E. Gabriele, W. Bernd, B. Ernst. Journal of Physics: Condensed Matter 11 (1999) 1697.

[44] C. Uher, J. Yang, S. Hu, D.T. Morelli, G.P. Meisner. Physical Review B 59 (1999) 8615-8621.

[45] S.R. Culp, J. Simonson, S.J. Poon, V. Ponnambalam, J. Edwards, T.M. Tritt. Applied Physics Letters 93 (2008).

[46] S.R. Culp, S.J. Poon, N. Hickman, T.M. Tritt, J. Blumm. Applied Physics Letters 88 (2006) 042106.

[47] X. Yan, G. Joshi, W. Liu, Y. Lan, H. Wang, S. Lee, J. Simonson, S. Poon, T. Tritt, G. Chen. Nano letters 11 (2010) 556-560.

[48] G. Joshi, X. Yan, H. Wang, W. Liu, G. Chen, Z. Ren. Advanced Energy Materials 1 (2011) 643-647.

Chapter 2

Measurement and Characterization Techniques for Thermoelectric Materials

2.1 Introduction

Since the key criterion for determining a good thermoelectric material is the figure of merit, $ZT = \frac{S^2 \sigma T}{\kappa}$, where S is the Seebeck coefficient, σ is the electrical conductivity, and κ is the thermal conductivity, it is important to accurately measure these electrical and thermal properties of thermoelectric materials to get the correct ZT values. These quantities are further related to more fundamental parameters such as carrier concentration (n), mobility (μ), and specific heat capacity (C_p) of the material. The study of these individual transport properties gives broad insight to evaluate the characteristics of thermoelectric materials.

To obtain reliable and accurate measurements, it is important to identify and quantify the systematic errors in the measurements [1]. We can check the accuracy of our experimental setup by using standard samples (materials with well-known and well-established properties), and the standard samples matching the thermoelectric properties of our own samples are of the most interest. What's more, in order to get trustable results, individual thermoelectric properties used to calculate ZT should be measured from the same sample to avoid possible inhomogeneity problems among different samples. In addition, electrical and thermal transport properties can have a very strong dependence on

crystallographic direction. Thus, samples with anisotropic properties must be measured from the same orientation to get the individual electrical and thermal properties to calculate their ZT. When available, several samples of the same composition or several sections of a given sample should also be measured to give information about repeatability and material uniformity.

Another important aspect of accurate measurements is the contact issue [2]. Establishing excellent electrical contacts to the thermoelectric materials is essential. For the measurement of the Seebeck coefficient, in addition to good electrical contact, nice thermal contact is also required to obtain accurate voltage and temperature data. The materials of the thermocouple and the buffer layer between the sample and thermocouple need to be carefully chosen to prevent any Seebeck voltage padding from the wires of thermal couple or the buffer materials. In regard to the measurements of thermal conductivity, there are several measurement techniques, such as the laser flash method, the radial flow method, and the pulse-power method. For each method, careful experimental procedures are needed. For instance, the laser flash technique requires a thin coating of graphite to the sample surface in order to obtain uniform absorption of the laser light on the sample surface. If good adhesion is not achieved, this coating procedure can potentially be a source of significant error.

In our measurements, we employed commercially available equipment (ZEM-3, ULVAC Inc.) for simultaneous electrical conductivity and Seebeck coefficient measurement up to 1000 °C. Commercial Laserflash equipment was used for thermal diffusivity measurement up to 900 °C (Laserflash LFA457, NETZSCH Instruments, Inc.). The specific heat capacity measurements were carried out on a Differential Scanning

Calorimeter (DSC 404 C, NETZSCH Instruments, Inc.). Hall measurements were performed on a Physical Property Measurement System (PPMS) from Quantum Design to get the carrier concentrations.

For our nanostructured samples, microstructure plays an important role on thermoelectric properties. Therefore, Scanning Electron Microscopy (SEM, LEO 1525) and Transmission Electron Microscopy (TEM, JEOL 2100F) equipment are used to characterize the microstructure of the materials. In addition, a build-in energy dispersive spectroscopy (EDS) system is applied to detect the composition of alloyed thermoelectric materials. The phase of the materials is also characterized by XRD (X'pert PRO PANalytical diffractometer with a Cu Ka radiation source).

In this chapter, various measurement techniques used in characterization of the thermoelectric properties will be summarized. The underlying measurement principles and challenges will be briefly described as well.

2.2 Electrical-Conductivity Measurement

2.2.1 Measurement Principles

The four-probe method has been widely used in the measurement of resistance. As shown in Figure 2.2.1, the current is injected through one set of current leads and voltage is measured using another set of voltage leads.

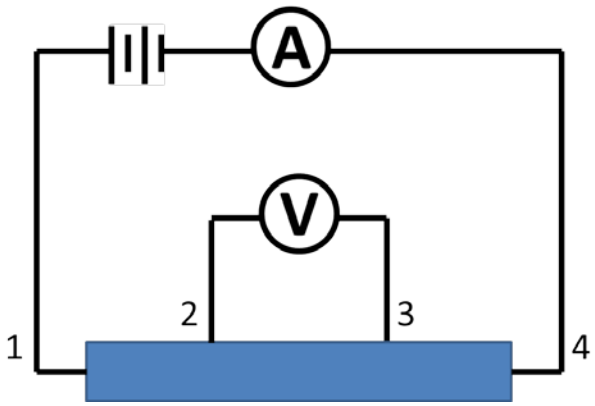

Figure 2.2.1 Four-probe method for measurement of resistance.

The electrical conductivity can be found from the following relation:

$$\sigma = \frac{1}{\rho} = R\frac{A}{l} \tag{2.2.1}$$

Where ρ is resistivity, R is the resistance, L is the length of the sample and A is cross-sectional area of the sample. The resistance is usually deduced from the slope of *V-I* plot during measurement for better accuracy. To eliminate the effect of contact resistance, samples should also be polished to get rid of the oxidized layer before measurement.

For thermoelectric materials, the electrical conductivity measurement is more complicated. When the current goes through the material, a temperature gradient will be generated according to the Peltier effect. Such temperature gradient will in turn introduce a Seebeck voltage due to the Seebeck effect [3]. Thus the total voltage measured is the sum of the ohmic voltage and Seebeck voltage. In order to minimize the effects of the Seebeck induced voltage, either an AC current source or a fast switching DC current source is usually used to measure the electrical conductivity, because the temperature gradient, arising from the Peltier effect, takes some time to develop [4, 5].

2.2.2 Measuring Electrical Conductivity on Commercial ZEM-3 System

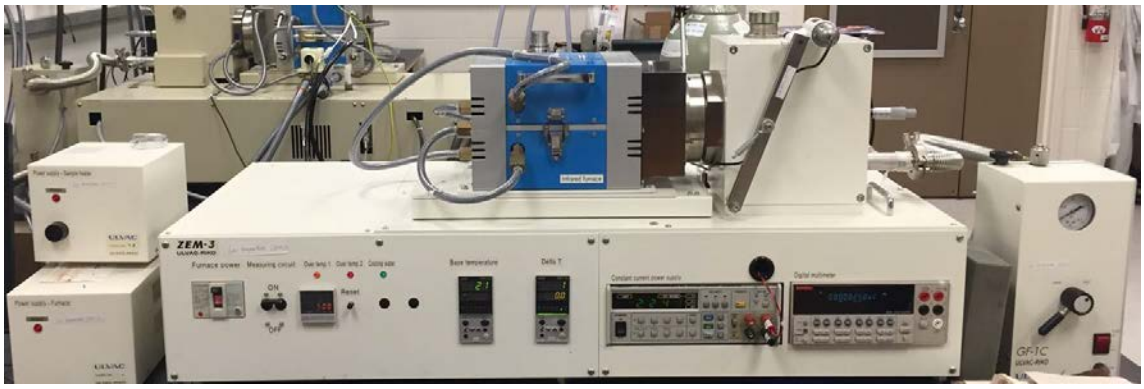

Figure 2.2.2 ULVAC ZEM-3 system.

For our measurements, we use the commercial equipment (ZEM-3, ULVAC Inc.) shown in Figure 2.2.2 which can measure electrical conductivity and Seebeck coefficient simultaneously.

Figure 2.2.3 is a picture showing a real sample mounted on the ZEM-3 system.

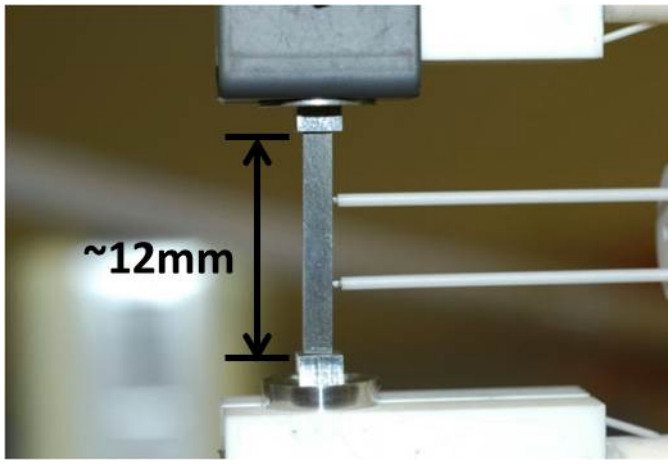

Figure 2.2.3 A picture of a sample mounted on the ZEM-3 system.

This setup is surrounded by an isothermal nickel radiation can to ensure a uniform temperature environment and together enclosed in an infra-red light furnace chamber. The furnace is used to heat up and control the atmosphere to measure the electrical conductivity at different temperatures. In order to minimize the temperature fluctuation by convection, measurement is usually done in partial vacuum at approximately 0.01 MPa because a small amount of inert gas is needed to transport heat and provide the temperature gradient across the sample for which Helium gas is always used.

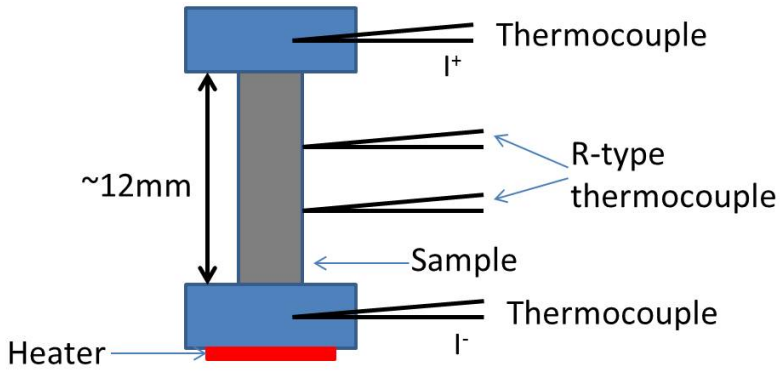

Figure 2.2.4 Schematic diagram for four-probe setup in ZEM-3 system.

A diagram illustrating the four-probe setup in the ZEM-3 system is given in Figure 2.2.4. The sample is held between the top and bottom stages by pressure from the clamp springs which can ensure good contact. There is a heater at the lower stage to create a temperature gradient along the sample for the measurement of Seebeck coefficient. In the middle, the two-probe thermocouples which can measure both temperature and voltage are placed against the sample surface by a small spring force. The pressure is to maintain a stable contact resistance. To ensure that the potential and temperature are uniform in the cross section corresponding to the measuring contact points, the distance between the probes and the end stages should be 1.5 times larger than the lateral dimension. All of our

samples are rectangular bars with an approximate geometry dimension of 2 mm × 2 mm × 12 mm. The sample dimensions are measured using a micrometer with an accuracy of ±0.001 mm. The space between the two probes is fixed at 6 mm with small fluctuations. To get precise and real spacing between those two pairs of thermocouples, an optical camera is installed to measure the two-probe distance.

A *V-I* plot is always performed to check the contact before the start of the actual measurement. A linear plot with no intercept and low contact resistance is required to guarantee a good contact. During the measurement, resistance is determined from the plotted *V-I* curve at different base temperatures. Then the electrical conductivity of the sample is calculated according to equation (2.2.1) from its measured resistance and specimen geometry.

During measurements, voltage is measured very quickly to minimize errors caused by the Peltier effect. However, a steady temperature gradient may exist along the sample during measurements. In reality, currents of opposite directions are run through the sample to cancel out the contributions from Seebeck voltage. The resistance of the sample can be calculated as:

$$R = \frac{V_1 - V_2}{2I} \tag{2.2.2}$$

where V_1 and V_2 are the two voltages measured at different directions of the current.

2.3 Seebeck Coefficient Measurement

2.3.1 Measurement Principles

By definition, the Seebeck coefficient equals the ratio of the potential difference ΔV versus the temperature difference ΔT between the two measuring points. Unlike electrical conductivity, the Seebeck coefficient is not geometry dependent. As illustrated in Figure 2.3.1, the temperature difference is measured by thermocouples, while the voltage difference is measured between one of the legs of the thermocouples. To measure the Seebeck coefficient at different base temperatures, the sample temperature T, is fixed and a small temperature gradient is introduced across the sample. The Seebeck voltage is recorded as a function of temperature difference and the slope yields the Seebeck coefficient.

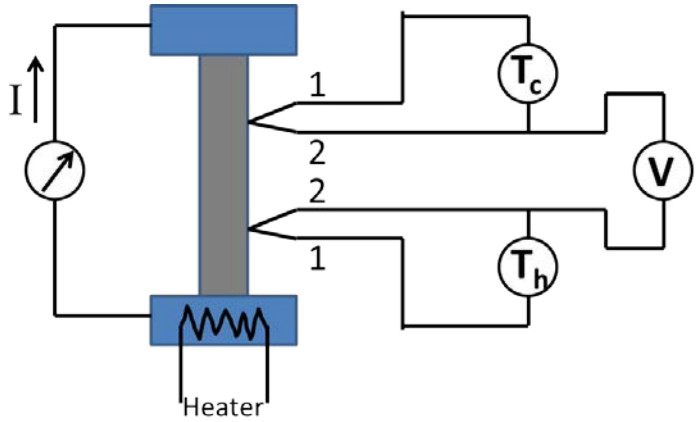

Figure 2.3.1 Illustration of Seebeck coefficient measurement.

Even though this measurement is not sensitive to heat loss, unsteady heat loss is still not desirable for accurate results. Thermocouples with a small diameter of 0.003 inches are

used to minimize conductive heat loss through the thermocouple wire. Theoretically, the curve of the induced voltage vs. temperature difference should pass through zero where there is no temperature gradient. However, in reality there is always some non-zero intercept which is called dark *emf*, because there is always some heat flowing through the thermocouple wires to the port which is coupled with the data acquisition system. If there is a thermal gradient over the thermocouple, it creates a dark *emf*. In general, if the dark *emf* does not exceed 10% of the total Seebeck voltage signal, the Seebeck coefficient measurement is considered to be reliable.

2.3.2 Measuring Seebeck Coefficient on Commercial ZEM-3 System

As mentioned above, the ZEM-3 system can measure the electrical conductivity and Seebeck coefficient simultaneously. For the measurement of Seebeck coefficient, no current is applied through the sample and the only source of voltage comes from the Seebeck effect of the sample and the probe leads. To obtain the Seebeck coefficient at different temperatures, the furnace chamber is heated up. In a typical measurement, a small temperature gradient ΔT will be created by the heater in the bottom stage and the Seebeck voltage ΔV is measured by the probes. Usually several temperature gradients are established and the Seebeck voltage is recorded as a function of ΔT. The Seeebck coefficient could be derived from the slope of ΔV vs. ΔT plot. It is noted that the readout from the slope usually contains the dark *emf* which is the Seebeck coefficient of the thermocouple, so the thermocouple Seebeck value should be compensated when determine the Seebeck coefficient of the sample. The data will only be acceptable if the dark *emf* is less than 10% of the total value.

2.4 Thermal Diffusivity Measurement by Laser Flash Method

The thermal conductivity in terms of the diffusivity and specific heat is given as:

$$\kappa = \rho C_p \alpha \tag{2.4.1}$$

where κ is the thermal conductivity, ρ is the mass density, C_p is the specific heat capacity, and α is the thermal diffusivity. In our measurements, we use Archimedes' principle to measure ρ, the differential scanning calorimeter (DSC 404 C, NETZSCH) to acquire the C_p value and the laser flash system (LFA 457, NETZSCH) to measure α.

Comparing to the measurement of electrical conductivity and Seebeck coefficient, the accuracy for the measurement of thermal conductivity is more challenging because thermal insulation can never be as good as electrical insulation. Heat loss through radiation, convection, and contacts always occurs, and can contribute to a significant portion of the total heat transferred. The laser-flash method has been developed to determine thermal diffusivity, in which a laser-flash source serves to heat the sample to avoid the thermal contact while the temperature is read in a very short time which can also minimize the heat loss during the process.

The laser-flash method was first described by Parker et al. in 1961 [6] and it has been reviewed on a number of occasions [7, 8]. A simple sketch of the method is shown in Figure 2.4.1, and the picture of the laser flash system LFA 457 is shown in Figure. 2.4.2.

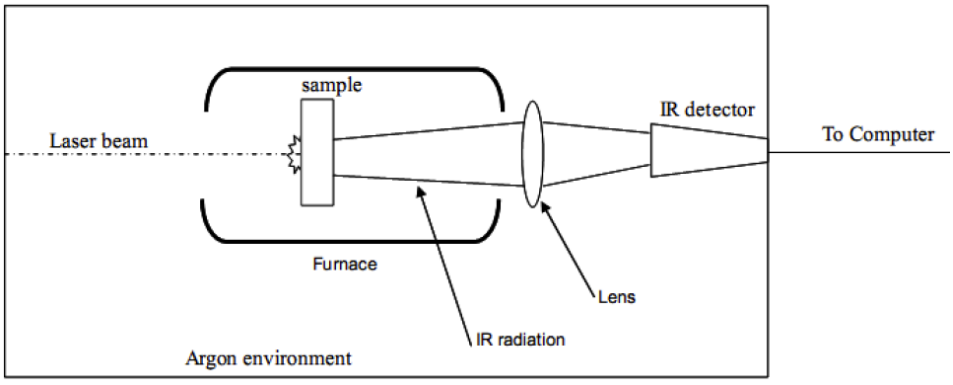

Figure 2.4.1 A simple sketch of the Laser flash method.

In this method, the sample's diameter is much greater than the thickness to ensure one dimensional thermal transport, so samples of around 12.7 mm in diameter and 2 mm in thickness are used. All the samples are also coated with graphite using a dry graphite spray to facilitate the black-body type of absorption. To make approximately one dimensional heat flow, the laser spot is also made uniform and has a greater area than the spot size of the temperature measurement.

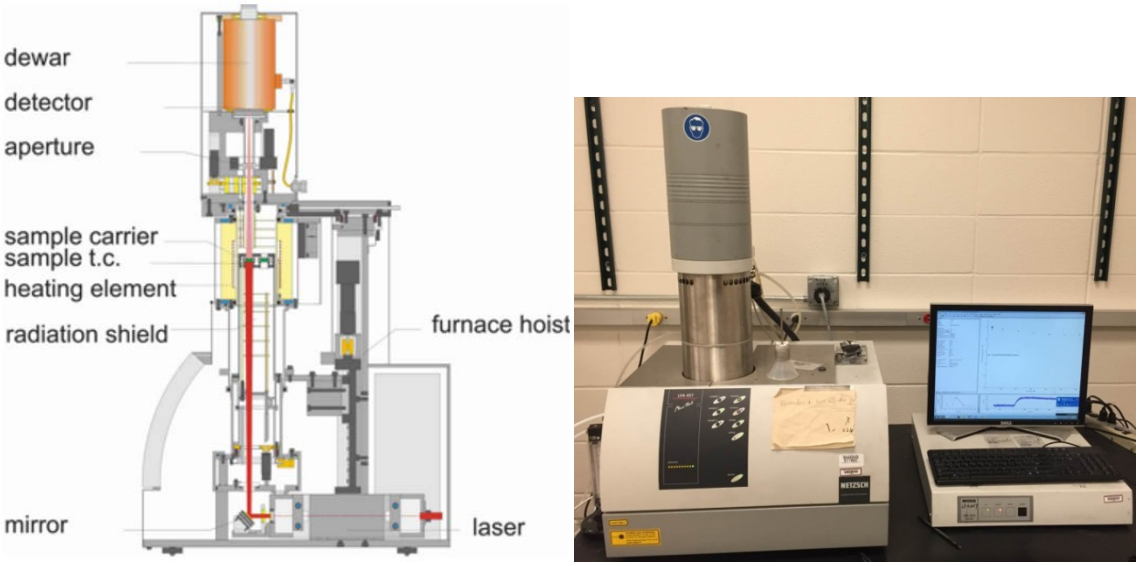

Figure 2.4.2 Laser flash LFA457, NETZSCH.

During the measurement, the laser beam is irradiated on one face of the sample with pulses not more than a millisecond long to minimize the heat loss. The temperature at the opposite face is measured with IR detector as in Figure 2.4.1. Then, the thermal diffusivity is calculated by the equation:

$$\alpha = 0.138 d^2 / t_{1/2} \qquad (2.4.2)$$

where $t_{1/2}$ is the time taken for the rear face to attain half of its maximum temperature and d is the thickness of the sample [1]. In the software, by using various models, the problems of finite-pulse and heat loss have been analyzed to account for and correct the error in the diffusivity measurement [9, 10]. Thus a fairly accurate value for the diffusivity can be obtained with the error range of ~ 2 %, most of which comes from the error in thickness measurement.

2.5 Specific-Heat Measurement by Differential Scanning Calorimeter

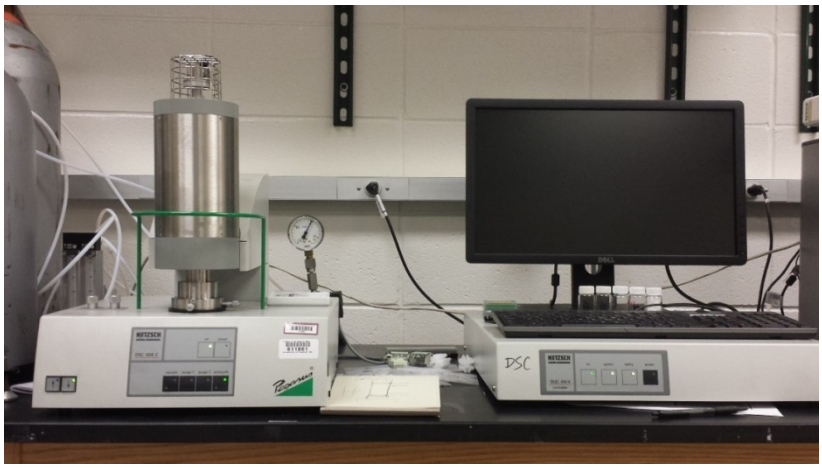

Figure 2.5.1 DSC (DSC 404 C, NETZSCH) for heat capacity measurement.

The Differential-Scanning Calorimetry (DSC) is widely used in the field of thermal characterization of solids and liquids, such as melting temperature, specific heat, phase transition temperature, the degree of crystallinity, and so on. The principle of DSC is to measure the difference in energy input into a testing sample and a reference material as a function of temperature.

During the measurement, the temperature will increase linearly with time (normally 20K/min) and the maximum temperature we can reach is 1000 ^{o}C for the DSC (DSC 404 C, NETZSCH). The reference sample should have a well-defined heat capacity over the temperature range of interest. In our system, sapphire discs with different thicknesses are used as reference material. To minimize the errors, optimum sample dimensions need to match that of the standard sapphire disc, so the testing sample is usually polished to a diameter of 5.5-6.0 mm and thickness of 0.5-1.0 mm. It is also important to match the (m $\times$Cp) value of the reference material to the (m$\times$Cp) value of the sample to enhance the accuracy.

Three measurement circles need to be done over the same temperature range for baseline, standard sample and testing sample, respectively. All three measurements have to be performed with the same crucibles and the same conditions. With the data of all three runs, the specific heat capacity of a material can be calculated as,

$$C_p = \frac{signal\ difference\ (sample - baseline)}{sample\ mass \times heating\ rate \times seneitivity} \qquad (2.5.1)$$

where the sensitivity is obtained from the sapphire measurement by the relation,

$$sensitivity = \frac{signal\ difference\ (sapphire - baseline)}{mass\ (sapphire) \times heating\ rate \times theoret.C_p(sapphire)} \quad (2.5.2)$$

Cp values are only valid when no weight loss occurs. With all these conditions provided, the specific heat capacity of a sample can be measured within 2% accuracy using DSC method.

2.6 Hall Measurement for Carrier Concentration and Mobility

Although the carrier concentration and mobility is not included in calculating ZT, these two parameters are important references for characterizing the transport properties of thermoelectric materials. The carrier concentration and mobility can be measured based on the Hall effect. As illustrated in Figure 2.6.1, when a conductor carrying electric current is subjected to an external magnetic field, the moving charge carriers will be deflected and accumulated by the Lorentz force to one side of the sample. A stable electric field perpendicular to both the electric current *I* and the magnetic field *B* will build up due to the accumulation to counter the Lorentz force. The steady electrical potential is called Hall voltage.

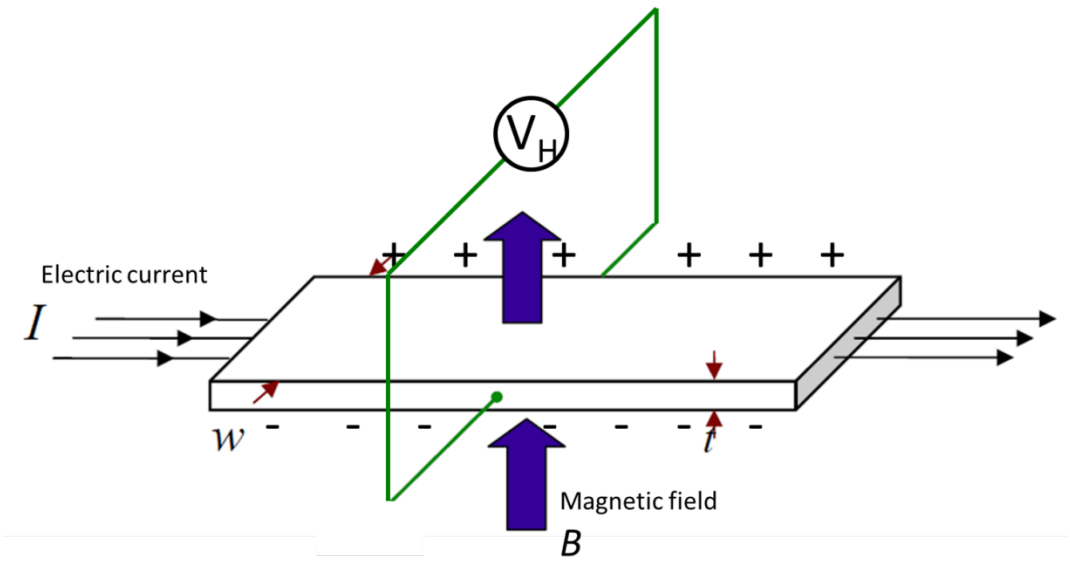

Figure 2.6.1 Schematic of the Hall Effect in a thin flat conductor.

For a simple conductor where there is only one type of charge carrier the Hall voltage V_H is given by,

$$V_H = -\frac{IB}{tne} \tag{2.6.1}$$

where t is the thickness of the flat conductor, e is the charge of moving carriers while n represents carrier concentration. The Hall coefficient R_H is define as,

$$R_H = \frac{V_H t}{IB} = -\frac{1}{ne} \tag{2.6.2}$$

The Hall coefficient is negative for free electrons as charge carriers since e is positive by definition. Therefore, carrier concentration can be derived from equation (2.6.2) and the type of charge carriers will also be found. The Hall mobility can be calculated by,

$$\mu = \frac{\sigma}{ne} \tag{2.6.3}$$

In our measurement, a Physical Property Measurement System (PPMS) from Quantum Design is used to get carrier concentrations from the Hall measurement. A sample with thickness of less than 0.5 mm and cross sectional area of ~ 6×6 mm is prepared by cutting and mechanical polishing. Four gold wires are connected to the edges of the sample by silver epoxy. During the measurement, a magnetic field of 3 T is applied. Two of the wires are used to pass the current while the other two measure the Hall voltage. To ensure accuracy, every sample is measured at least four times by changing the applied current and reversing the direction of the magnetic field, and the final result is the average of several measurements.

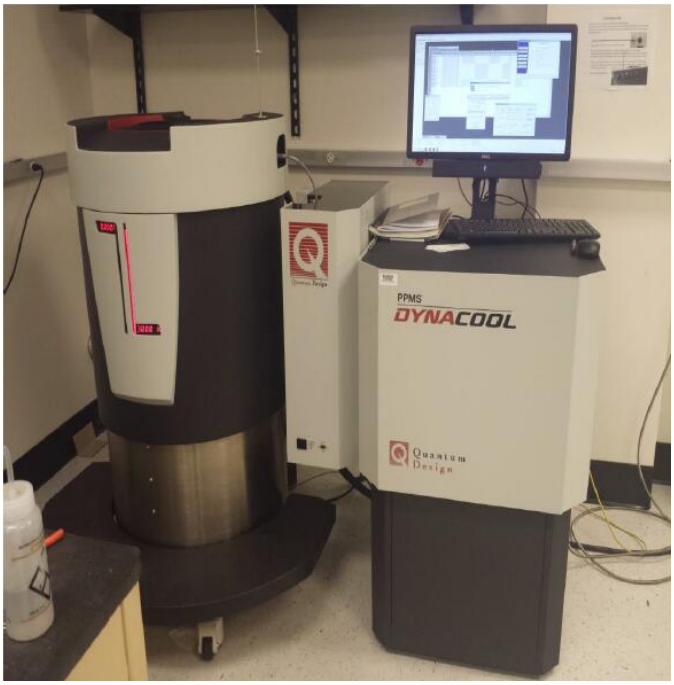

Figure 2.6.2 PPMS (Quantum Design) for carrier concentration and mobility measurement.

References

[1] S. Poon, T. Tritt. Recent trends in thermoelectric materials research II, Semiconductors and Semimetals 70 (2001) 37.

[2] S. Sze. Physics of Semiconductor Devices 2nd edition Awiley Inter-science John wiley and Sons, New York (1981).

[3] D. Rowe, R. Bunce. Journal of Physics E: Scientific Instruments 4 (1971) 902.

[4] H. Goldsmid. Proceedings of the Physical Society 71 (1958) 633.

[5] T. Dauphinee, S. Woods. Review of Scientific Instruments 26 (1955) 693-695.

[6] W. Parker, R. Jenkins, C. Butler, G. Abbott. Journal of Applied Physics 32 (1961) 1679-1684.

[7] F. Righini, A. Cezairliyan. High Temperature High Pressures 5 (1973) 481-501.

[8] R. Taylor, K. Maglic, K. Maglic. Compendium of Thermophysical Property Measurement Methods Vol: 2: Recommended Measurement Techniques and Practices. Plenum Press, New York, 1992.

[9] R. Taylor, L. Clark. High Temperature High Pressures 6 (1974) 65-72.

[10] R.D. Cowan. Journal of Applied Physics 34 (1963) 926-927.

Chapter 3

Thermoelectric Properties of Nb-Doped N-type Half-Heusler Compounds $(Hf_{0.25}Zr_{0.75})_{1-x}Nb_xNiSn$

A part of this chapter contains our previously published work: "Thermoelectric properties of n-type half-Heusler compounds $(Hf_{0.25}Zr_{0.75})_{1-x}Nb_xNiSn$", *Acta Materialia* (2016) 113, 41-47.

3.1 Introduction

The most widely studied n-type half-Heusler compositions are MNiSn (M = Ti, Zr, and Hf). Theoretical calculations show that MNiSn compounds are narrow-bandgap semiconductors and have an indirect bandgap with the conduction band extrema at *X* point and valance band extrema at *Γ* point [1, 2]. The bandgap of MNiSn is around 0.1 – 0.3 eV, obtained from both theoretical and experimental studies [3, 4]. MNiSn compounds are good thermoelectric materials for their high Seebeck coefficients of above -200 μV K^{-1} at room temperature [5]. Such high Seebeck coefficients can be ascribed to the sharp slope of density of states near the Fermi level and its large density of states effective mass $m^* = 2.8 \pm 0.2\ m_e$ [6, 7]. To improve the thermoelectric properties, doping with adjacent elements is a common approach to optimize the electrical properties. However, increasing the carrier concentration by dopants to enhance the electrical conductivity will at the same time decrease the Seebeck coefficient. As a

result, the carrier concentration should be carefully tuned to achieve high electrical conductivity without degrading the Seebeck coefficient too much. The optimized carrier concentration at room temperature for MNiSn compounds is found to be on the order of 10^{20} cm^{-3} via different doping methods [8-10].

In this chapter, we study the effects of Nb doping on the thermoelectric properties of $Hf_{0.25}Zr_{0.75}NiSn$ based compounds. Nb has one more valence electron than Hf/Zr so it can increase the carrier concentration for this n-type half-Heusler compound. In fact, Hiroaki Muta *et al.* did Nb doping in ZrNiSn and TiNiSn before and the maximum ZT value of 0.6 was obtained for $Zr_{0.98}Nb_{0.02}NiSn$ at 800 K [11]. Most recently, Julia Krez *et al.* reported Nb doping in the phase separated n-type $Ti_{0.3}Zr_{0.35}Hf_{0.35}NiSn$ compound and peak ZT value around 0.7 at 900 K was achieved [8]. Here we investigate the effects of Nb doping in the nanostructured $Hf_{0.25}Zr_{0.75}NiSn$ compounds. The carrier concentration is optimized by different concentrations of Nb doping and the thermal and electrical properties of these samples are discussed accordingly. It is interesting to note that some full-Heusler nanoinclusions are found within the half-Heusler matrix by SEM and TEM analysis, which could also play a positive role in the improvement of the thermoelectric properties. Power factor of ~47 μW cm^{-1} K^{-2} and peak ZT of ~0.9 are achieved with Nb doping from 1.8 at% to 2.2 at% at 700 ^{o}C. The output power density and leg efficiency of all the samples are also calculated based on the engineering power factor $(PF)_{eng}$ and engineering figure of merit $(ZT)_{eng}$.

3.2 Experimental Procedures

Various synthesis methods for half-Heusler alloys have been reported, such as solid-state reaction [12], induction melting [13], levitation melting [6], optical-floating-zone melting [14], and microwave heating [15]. Different fabrication methods can result in microstructural difference in samples, leading to variations of thermoelectric properties. Here, for our nanostructured half-Heusler $(Hf_{0.25}Zr_{0.75})_{1-x}Nb_xNiSn$ samples, we employed the nanostructuring approach, which consists of three steps: arc-melting, ball-milling, and hot-pressing.

3.2.1 Arc-melting

The arc-melting method involves the melting of conducting materials using an electric arc. It can reach temperatures over 3000 ^{o}C, so it is suitable for the synthesis of half-Heusler alloys which consists of high melting point elements such as hafnium with a melting point of 2231 ^{o}C. The arc-melting furnace we use is shown in Figure 3.2.1. The electrode stingers (cathode) are made up of tungsten. The hearth plate (anode) is a cylindrical crucible made up of copper which is surrounded by a water jacket to cool down the melted ingot. When the electrode stingers are brought close to the materials on the hearth plate, they conduct a current that forms an arc between them and the materials in the furnace, causing the materials to melt. The melting chamber is pumped down at first and then filled with argon gas to avoid the oxidation of materials.

Figure 3.2.1 Picture of arc melter (Gold Star 452) device form Miller.

$(Hf_{0.25}Zr_{0.75})_{1-x}Nb_xNiSn$ (x = 0, 0.005, 0.01, 0.012, 0.014, 0.016, 0.018, 0.02, 0.022, 0.025, and 0.03) ingots were synthesized by arc-melting the Hf chips (99.7%, Alfa Aesar), Zr slug (99.5%, Alfa Aesar), Nb foil (99.97%, Alfa Aesar), Ni slug (99.98%, Alfa Aesar), and Sn shot (99.99+%, Alfa Aesar) according to the stoichiometry. The ingots were arc-melted at least three times, each time flipped over to ensure homogeneity. The weight loss during arc-melting is less than 0.5%.

3.2.2 Ball-milling

The ball mill is used for grinding materials. The high-energy ball-milling machine we use is shown in Figure 3.2.2, and it can reduce the grain size effectively. For n-type half-Heusler alloys, nanopowders with the particle size around 50 nm can be obtained after 5 – 9 hours ball-milling [16].

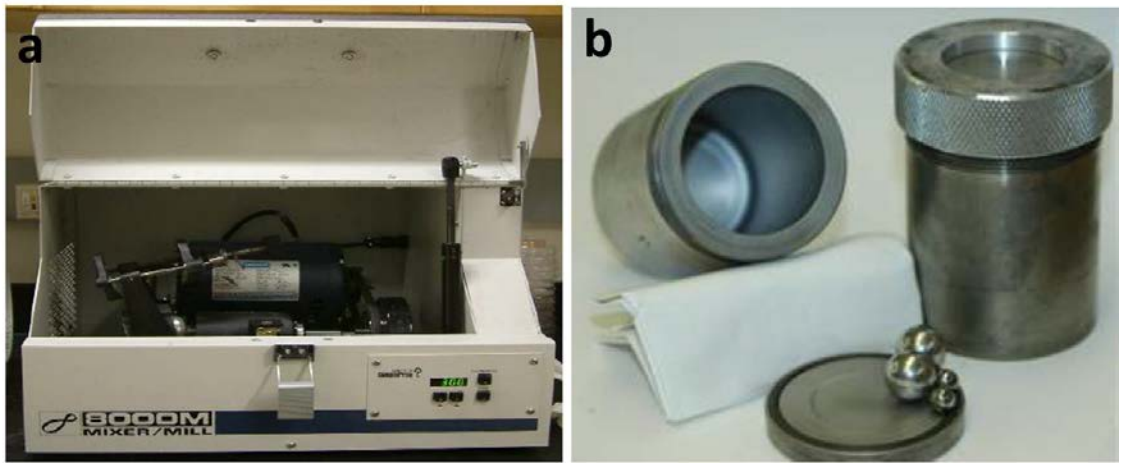

Figure 3.2.2 (a) High-energy ball mill machine (SPEX SamplePrep 8000M Mixer/Mills), (b) Stainless steel ball-milling jars and balls.

The ball-milling process is also widely used in the mechanical alloying. The alloying occurs basically through a repeated collision process of fracturing and cold welding of powder particles trapped between grinding balls. Although the average temperature inside ball milling jar is normally less than 100 °C, the local temperature could actually be raised to the alloying temperature through heat generated by the collisions, which is the driving force for the inter-diffusion of the components along atomically clean fracture surfaces [17]. Therefore, through ball-milling process, not only the grain size can be greatly reduced, but also the composition will be more homogeneous by further mechanical alloying. In our experiments, the alloyed ingots were put into the stainless-steel jar with half-inch stainless-steel grinding balls and ball-milled for 5-9 hours to make nanopowders. To protect the powder from oxidation, the ball-milling jar is filed with argon gas.

3.2.3 Hot-pressing

The $(Hf_{0.25}Zr_{0.75})_{1-x}Nb_xNiSn$ nanopowder needs to be consolidated into dense bulk form for the measurement of the thermoelectric properties. Usually, samples with relative density of more than 95% are required to provide good carrier mobility. On the other hand, the nanostructures need to be preserved during the densification process to achieve better performance. In our experiments, we use the alternating current (AC) hot press in which the sample is heated by Joule heating, as shown in Figure 3.2.3. The advantages of this hot press are that it has fast heating rate, so samples can be heated up to above 1000 °C within minutes, and an active cooling circuit is linked to the system as well, so the cooling rate will also be quick which is within minutes as well. Both the features can contribute to maintaining the nanostructures in the sample and preventing too much grain growth as the temperature increases.

Figure 3.2.3 Home-made hot press.

In a typical press, about 2.6 g $(Hf_{0.25}Zr_{0.75})_{1-x}Nb_xNiSn$ nanopowder was loaded into a graphite die in the glovebox filled with argon gas to minimize the oxidation of the nanopowder. During hot-press, the sample was heated to more than 1000 ^oC in 4 – 6 minutes by a large AC current passing through it. It was also held at that high temperature for about 2 minutes to make sure that the pressed sample is uniformly dense. A pressure of 80 MPa was applied on the sample during the whole process to ensure full density of the sample. After that, the graphite die with the sample in it was taken out immediately to let it slowly cool down to room temperature. A disc sample of half inch in diameter and around 2 mm in thickness is obtained after hot press, which can be used for laserflash measurement.

The volumetric densities of the samples were measured by Archimede's method. The densities for $(Hf_{0.25}Zr_{0.75})_{1-x}Nb_xNiSn$ samples (x = 0, 0.005, 0.01, 0.012, 0.014, 0.016, 0.018, 0.02, 0.022, 0.025, and 0.03) are 8.479 g/cm^3, 8.415 g/cm^3, 8.427 g/cm^3, 8.431 g/cm^3, 8.431 g/cm^3, 8.430 g/cm^3, 8.451 g/cm^3, 8.431 g/cm^3, 8.426 g/cm^3, 8.461 g/cm^3, and 8.420 g/cm^3, respectively. All of samples have a relative density of more than 99% (experimental density vs. the theoretical density of 8.482 g/cm^3).

3.2.4 Characterization

The thermal diffusivities of the disks were measured on a laser-flash equipment (LFA457, Netzsch). The specific heat capacity measurements were carried out on a differential scanning calorimeter (DSC 404 C, Netzsch). Samples were also cut into 2 × 2 × 12 mm bars for electrical conductivity and Seebeck coefficient measurements from room temperature to 700 °C on a commercial equipment (ZEM-3, Ulvac). Hall measurements

were performed on a Physical Property Measurement System (Quantum design) to get the carrier concentrations of these samples at room temperature. The samples were also characterized by XRD (X'pert PRO PANalytical diffractometer with a Cu Ka radiation source), SEM (LEO 1525), and TEM (JEOL 2100F). The uncertainties were estimated to be 3% for thermal diffusivity, specific heat capacity, and electrical conductivity, and 5% for Seebeck coefficient, which results in an uncertainty of 11% for ZT. To increase the readability of all the curves, all the figures are plotted without the error bars.

3.3 Results and Discussions

3.3.1 Phase and Microstructures

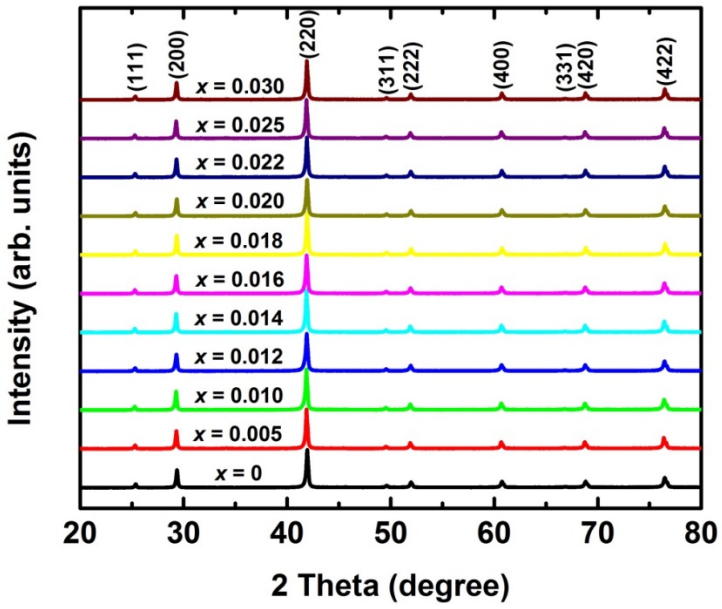

Figure 3.3.1 XRD patterns of $(Hf_{0.25}Zr_{0.75})_{1-x}Nb_xNiSn$ samples(x = 0, 0.005, 0.01, 0.012, 0.014, 0.016, 0.018, 0.02, 0.022, 0.025, and 0.03).

All the Nb doped $(Hf_{0.25}Zr_{0.75})_{1-x}Nb_xNiSn$ samples (x = 0-0.03) obtained by arc-melting, ball-milling, and hot-pressing have single half-Heusler phase in the detection limit of the

XRD machine, shown in Figure 3.3.1. All the peaks are indexed as the cubic half-Heusler phase.

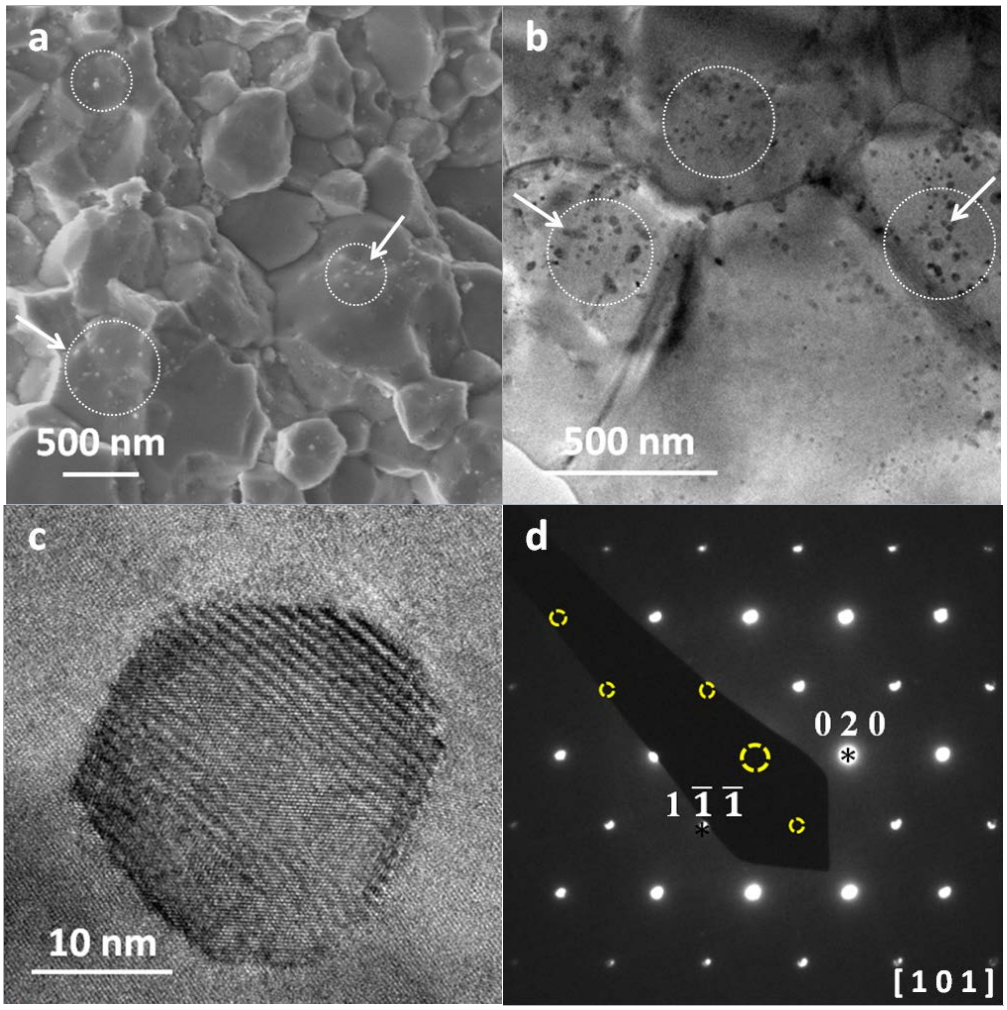

Figure 3.3.2 SEM image (a) and the low magnification TEM image (b) of sample $(Hf_{0.25}Zr_{0.75})_{0.978}Nb_{0.022}NiSn$, high resolution TEM image (c) and the electron diffraction pattern (d) of the full Heusler nanoinclusion. In image (d), the spots covered by the stopper are marked as yellow dashed circles.

Figure 3.3.2 shows the microstructures of the $(Hf_{0.25}Zr_{0.75})_{0.978}Nb_{0.022}NiSn$ samples. The SEM image of the freshly fractured surface in Figure 3.3.2 (a) indicates that the sample is densely packed polycrystalline. The relative density of the sample is calculated to be 99.3% (experimental density of 8.426 g/cm^3 vs. the theoretical density of 8.482 g/cm^3), which also demonstrates the high compaction. The grain size of the sample ranges from 200 nm

to micrometers. The wide distribution of the grain size may be ascribed to the non-uniform grinding during ball-milling and high hot-pressing temperature for which the nanoparticles grow rapidly.

Figure 3.3.2 (b) is the low-magnification TEM image that confirms the grain size distribution from hundred nanometers to micrometers and the grain boundaries. Furthermore, some small particles on the scale of several nanometers can be seen on the surface of the grains as shown in the SEM image in Figure 3.3.2 (a), and this can also be noticed in the low-magnification TEM image with some black spots on the individual grain (Figure 3.3.2 (b)). High-magnification TEM image is taken on one of those nanoinclusions and is shown in Figure 3.3.2 (c). This nanoinclusion is about 20 nm in diameter. The electron diffraction pattern is taken on the nanoinclusion and presented in Figure 3.3.2 (d). This electron-diffraction pattern can be indexed as full-Heusler structure (space group Fm3m) oriented along the [101] zone axis. On the other hand, split spots can be noticed in the electron diffraction pattern that originates from the half-Heusler matrix with similar diffraction pattern along [101] zone axis. As full-Heusler has slightly larger lattice constant than half-Heusler, for the split spots, the part closer to the transmission spot belongs to the full-Heusler and the farther part belongs to the matrix. By measuring the split diffraction spots, we get about 2% differences of the lattice parameters between full-Heusler and half-Heusler. Therefore, full-Heusler nanoinclusions are distributed in this half-Heulser sample.

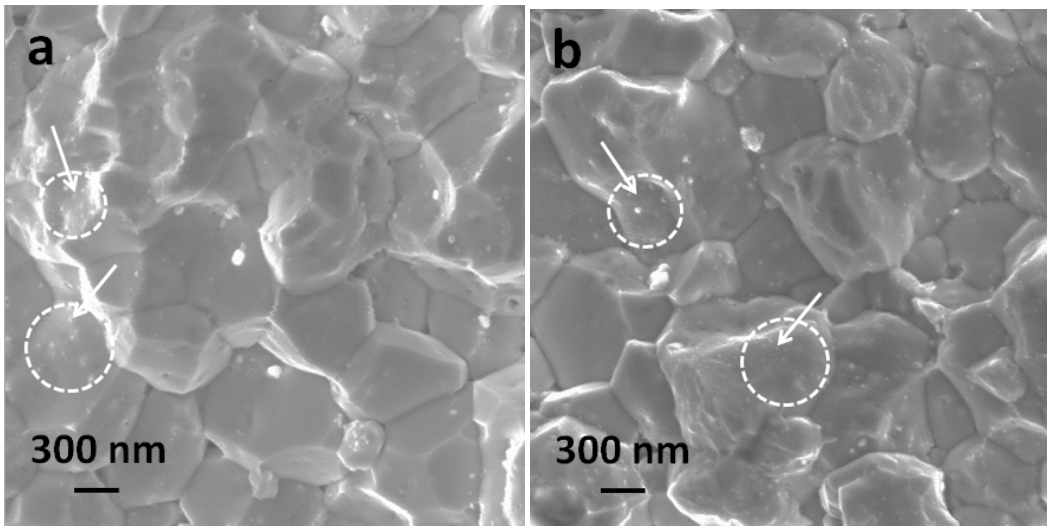

Figure 3.3.3 SEM images of $(Hf_{0.25}Zr_{0.75})_{1-x}Nb_xNiSn$ samples with x=0 (a), x=0.01 (b).

In addition, samples with other doping concentrations (x = 0, 0.01) were also found to have such nanoparticles on the grains in their SEM images shown in Figure 3.3.3, so we believe that the full-Heusler nanoinclusions exist in all of our half-Heusler samples. Although we start our experiments by arc-melting the elements in stoichiometry, higher nickel concentration around 38 at% compared to the stoichiometric value of 33 at% is found in the final hot-pressed samples by EDS. Such Ni/interstitial site intrinsic disorder is also reported by others in ZrNiSn and about 5% excess of Ni was found [7, 18]. Reports of calculations, synchrotron x-ray and neutron scattering studies pointed out that rather than a statistical distribution, the excess Ni atoms tend to come close to each other and form full-Heusler nano-clusters within the half-Heusler matrix [19, 20], which is consistent with our observations of the full-Heusler nanoinclusions. It is reported that excess Ni on interstitial sites can produce in-gap electronic states near the Fermi energy and the nanoinclusions can also act as phonon scattering centers to reduce lattice thermal

conductivity [12, 21-23], both of which are beneficial for the improvement of thermoelectric properties.

3.3.2 Electrical Properties

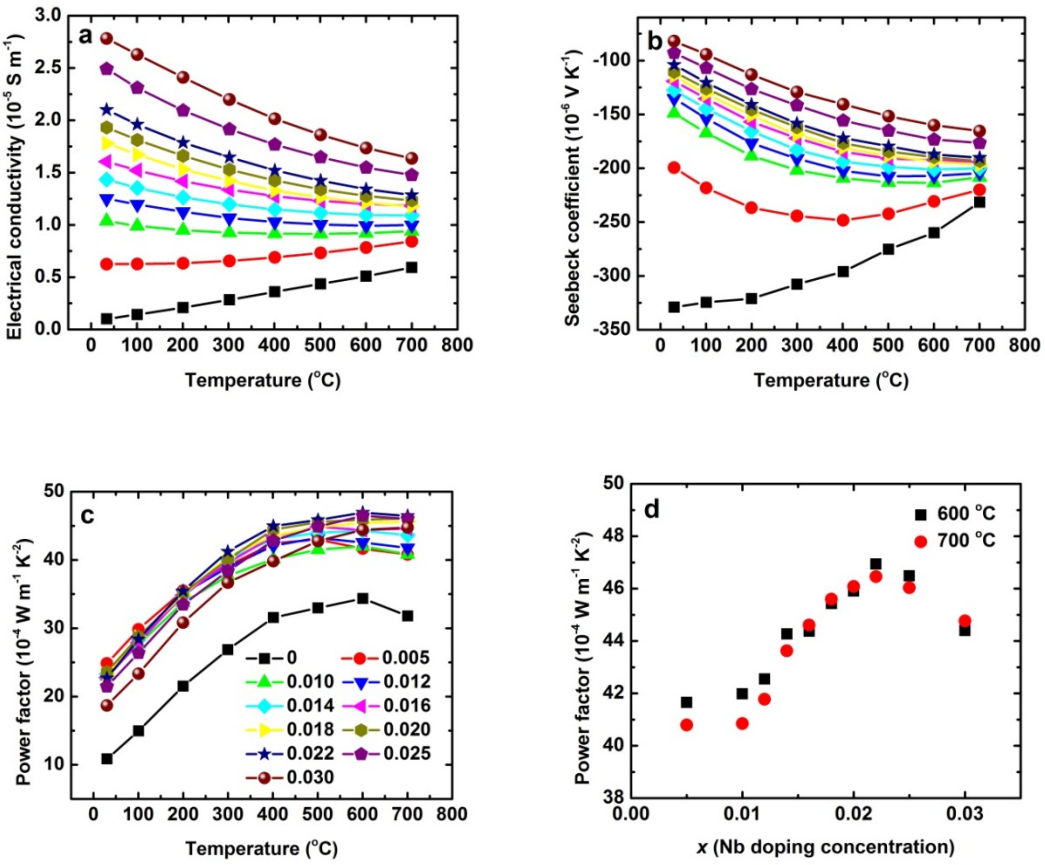

Figure 3.3.4 Temperature-dependent electrical conductivity (a), Seebeck coefficient (b), power factor (c), and power factor at 600 °C and 700 °C (d) of $(Hf_{0.25}Zr_{0.75})_{1-x}Nb_xNiSn$ samples (x = 0, 0.005, 0.01, 0.012, 0.014, 0.016, 0.018, 0.02, 0.022, 0.025, and 0.03).

The temperature-dependent electrical conductivity of the undoped $Hf_{0.25}Zr_{0.75}NiSn$ and the Nb doped $(Hf_{0.25}Zr_{0.75})_{1-x}Nb_xNiSn$ samples are presented in Figure 3.3.4 (a). For the undoped and 0.5 at% Nb doped samples, the electrical conductivity increases when the temperature increases showing the typical behavior of semiconductors. When the samples

are doped with more than 1.2 at% Nb, the electrical conductivity decreases with temperature which exhibits characteristics of degenerate semiconductors. Comparing all the doped samples, the higher the doping level, the larger the electrical conductivity is. The Hall carrier concentrations and Hall mobility at room temperature of all the samples are measured and listed in Table 3.3.1. Since Nb has one more valence electron than Hf/Zr, it acts as an electron donor. Therefore, when the amount of Nb doping increases, the Hall carrier concentration increases leading to the enhancement of electrical conductivity.

Table 3.3.1. Hall carrier concentration and Hall mobility at room temperature of $(Hf_{0.25}Zr_{0.75})_{1-x}Nb_xNiSn$ samples (x = 0, 0.005, 0.01, 0.012, 0.014, 0.016, 0.018, 0.02, 0.022, 0.025, and 0.03).

Nb doping level (at%)	0	0.5	1	1.2	1.4	1.6	1.8	2	2.2	2.5	3
Carrier concentration (10^{20} cm^{-3})	0.17	0.96	1.76	2.16	2.7	3.05	3.28	3.31	3.92	4.72	5.85
Mobility (cm^2 V^{-1} S^{-1})	37.5	39.7	36.7	36.2	33.2	32.9	33.9	36.5	33.5	33.0	29.7

Figure 3.3.4 (b) shows the temperature-dependent Seebeck coefficient. Without any doping, the absolute value of Seebeck coefficient decreases with increasing temperature because of the thermal excitation of both electrons and holes. After Nb doping, the absolute value of Seebeck coefficient increases as temperature increases at first, and then it begins to decrease or stops increasing at higher temperatures which is due to the excitation of intrinsic charge carriers, known as bipolar effects. When the doping concentration is higher than 2 at%, the Seebeck coefficient shows continuous increase in the whole temperature range from room temperature to 700 °C, which means that the

bipolar effects can be suppressed by higher concentrations of extrinsic charge carriers. At any fixed temperature, the Seebeck coefficient decreases with Nb doping concentration increasing, which is due to the increase of carrier concentration. With the optimized carrier concentration, the power factors of the Nb doped samples have significant improvement in comparison with the undoped one in the whole temperature range, as shown in Figure 3.3.4 (c). Figure 3.3.4 (d) presents the values of power factors at 600 ^{o}C and 700 ^{o}C with different Nb doping levels. As the doping concentration increases, the power factor increases at first and then decreases when the carrier concentration becomes too large. The highest power factor of ~47 μW cm^{-1} K^{-2} is achieved at 600 °C with Nb doping concentration of 2.2 at% and this is about 37% enhancement over the undoped sample.

3.3.3 Thermal Properties

Figure 3.3.5 gives the temperature-dependent thermal diffusivity (a), specific heat capacity (b), total thermal conductivity (c), and lattice thermal conductivity (d) of the undoped and Nb doped samples. With increasing temperature, the thermal diffusivity decreases at first and then increases at high temperatures due to the bipolar effects especially for the undoped samples and the ones doped with low concentration. The suppression of bipolar effects can also be clearly noticed as the upturn of thermal diffusivity happens at higher temperatures when the Nb doping concentration increases. The specific heat capacity (Cp) of the samples doped with 1.2 at% and 2.2 at% Nb is measured and are shown in Figure 3.3.5 (b). The Cp values of the two samples are almost the same and the minor difference is within the measurement error of DSC, so we use the

Cp of 1.2 at% doped sample for all the doped samples. The thermal conductivity in Figure 3.3.5 (c) is calculated by multiplying the density, the specific heat capacity, and the thermal diffusivity. It turns out that thermal conductivities of all the doped samples are much larger than the undoped one and increase with doping concentration.

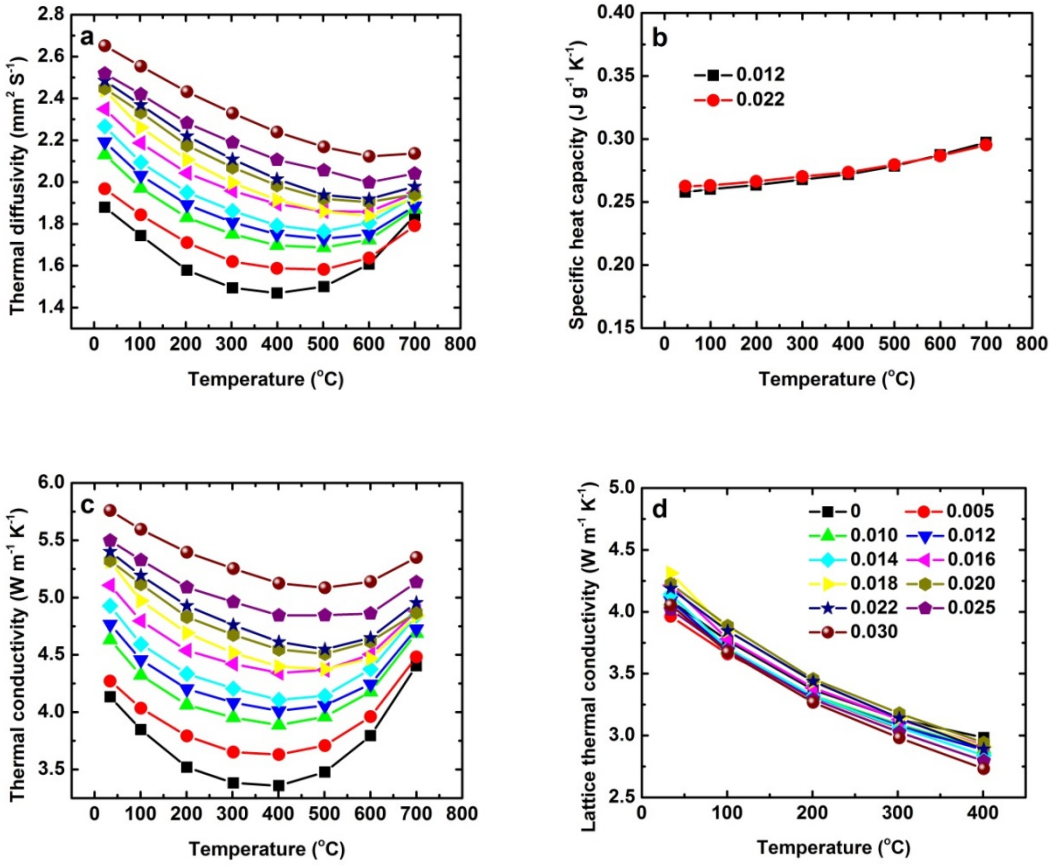

Figure 3.3.5 Temperature-dependent thermal diffusivity (a), specific heat capacity (b), thermal conductivity (c), and lattice thermal conductivity (d) of $(Hf_{0.25}Zr_{0.75})_{1-x}Nb_xNiSn$ samples (x = 0, 0.005, 0.1, 0.012, 0.014, 0.016, 0.018, 0.02, 0.022, 0.025, and 0.03).

The total thermal conductivity is the sum of the lattice thermal conductivity and the electronic thermal conductivity from the charge carriers and bipolar effects. The electronic thermal conductivity can be obtained using the Wiedemann-Franz relation, κ_e =

$L\sigma T$, where L is the Lorenz number, σ is electrical conductivity, and T is absolute temperature. The Lorenz number can be calculated according to the following equation,

$$L = \left(\frac{k_B}{e}\right)^2 \left(\frac{(r+7/2)F_{r+5/2}(\xi)}{(r+3/2)F_{r+1/2}(\xi)} - \left[\frac{(r+5/2)F_{r+3/2}(\xi)}{(r+3/2)F_{r+1/2}(\xi)} \right]^2 \right) \tag{3.3.1}$$

where r is the scattering parameter, and F_n is the Fermi integral given by,

$$F_n(\xi) = \int_0^\infty \frac{\chi^n}{1+e^{\chi-\xi}} d\chi \tag{3.3.2}$$

Based on a single parabolic band model, the reduced Fermi energy ξ can be deduced from the Seebeck coefficient as,

$$S = \pm \frac{k_B}{e} \left(\frac{(r+5/2)F_{r+3/2}(\xi)}{(r+3/2)F_{r+1/2}(\xi)} - \xi \right) \tag{3.3.3}$$

In this calculation, we assumed that the acoustic phonon scattering dominates in the carrier scattering mechanism. The calculation results of the Lorenz number are shown in Figure 3.3.6. Accordingly, the lattice thermal conductivity of all the samples is calculated from room temperature to 400 °C right before the bipolar effects occur by subtracting the electronic thermal conductivity from the total thermal conductivity. As shown in Figure 4 (d), the lattice thermal conductivity decreases with increasing temperature. There is not too much difference of the lattice thermal conductivity among all the samples. This is probably because the doping concentrations for our samples are pretty low (only up to 3%), so the point defect scattering caused by the dopants is small and is not the dominant phonon scattering mechanism here.

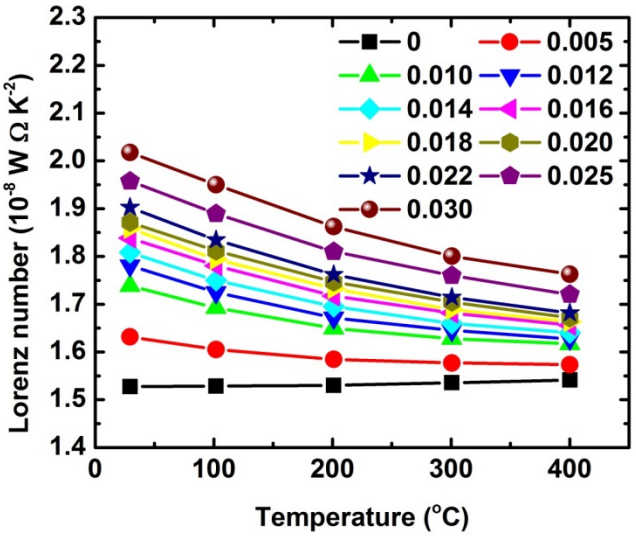

Figure3.3.6 Calculated temperature-dependent Lorenz number of $(Hf_{0.25}Zr_{0.75})_{1-x}Nb_xNiSn$ samples (x = 0, 0.005, 0.1, 0.012, 0.014, 0.016, 0.018, 0.02, 0.022, 0.025, and 0.03).

3.3.4 Figure of Merit ZT

Figure 3.3.7 presents the temperature-dependent figure of merit ZT values of all the samples. Compared to the undoped sample, the samples doped with x from 0.5 at% to 2.2 at% Nb show enhanced ZT values in the whole temperature range from room temperature to 700 °C. When the doping concentration is higher than 2.2 at%, the ZT values begin to decrease because the carrier concentration is too large. As a result, the highest ZT of ~0.9 is achieved at 700 °C in samples doped with Nb from 1.8 at% to 2.2 at%.

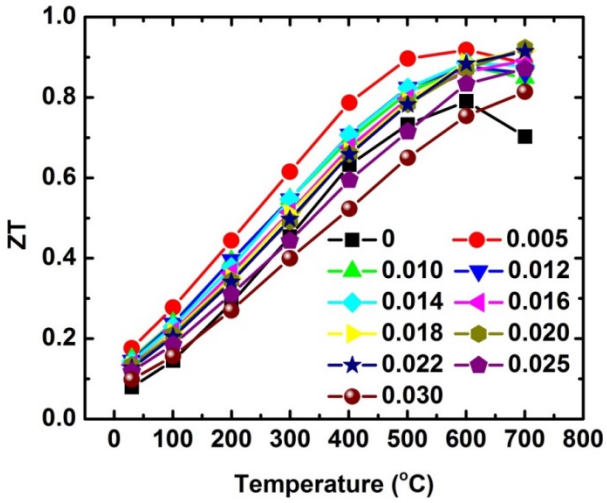

Figure 3.3.7 Temperature-dependent ZT of $(Hf_{0.25}Zr_{0.75})_{1-x}Nb_xNiSn$ samples (x = 0, 0.005, 0.01, 0.012, 0.014, 0.016, 0.018, 0.02, 0.022, 0.025, and 0.03).

3.3.5 Calculated Output Power and Efficiency

Since the conventional ZT and power factor only indicate the performance of a material at a specific temperature, Kim *et al*. defined an engineering figure of merit $(ZT)_{eng}$ and an engineering power factor $(PF)_{eng}$ which are associated with the temperature boundaries and gradient and will provide a more accurate prediction of the maximum efficiency of a material by accounting for cumulative temperature-dependent properties [24]. The engineering power factor $(PF)_{eng}$ and engineering figure of merit $(ZT)_{eng}$ of the undoped sample and all the Nb doped samples are calculated assuming a leg length of 2 mm, a cold-side temperature of 50 °C and a hot-side temperature ranging from 75 °C to 700 °C. The engineering power factor $(PF)_{eng}$ and engineering figure of merit $(ZT)_{eng}$ are calculated by,

$$(PF)_{eng} = \frac{\left(\int_{T_C}^{T_H} S(T)dT\right)^2}{\int_{T_C}^{T_H} \rho(T)dT} \tag{3.3.4}$$

$$(ZT)_{eng} = \frac{(PF)_{eng}}{\int_{T_C}^{T_H} \kappa(T)dT}(T_H - T_C) \tag{3.3.5}$$

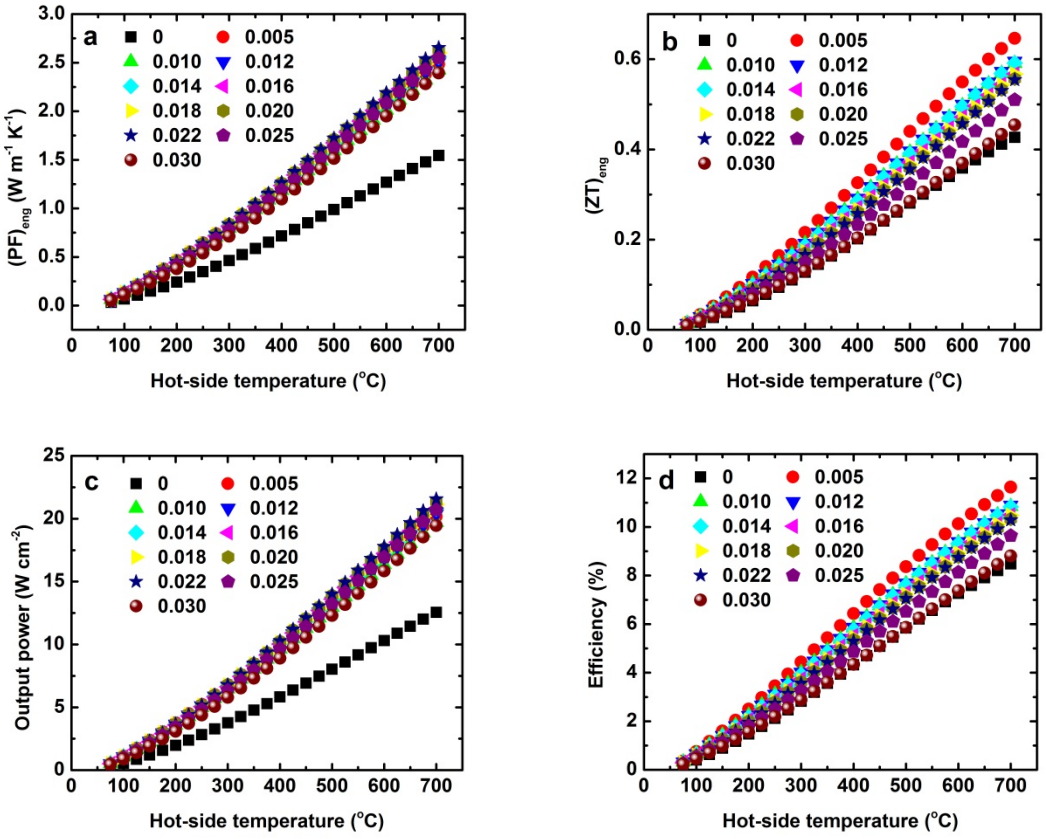

Figure 3.3.8 Calculated $(PF)_{eng}$ (a), $(ZT)_{eng}$ (b), output power density (c), and efficiency (d) as a function of hot-side temperature for $(Hf_{0.25}Zr_{0.75})_{1-x}Nb_xNiSn$ samples (x = 0, 0.005, 0.01, 0.012, 0.014, 0.016, 0.018, 0.02, 0.022, 0.025, and 0.03) with cold side at 50 °C and leg length of 2 mm.

The results of $(PF)_{eng}$ and $(ZT)_{eng}$ as a function of hot side temperature are presented in Figure 3.3.8 (a) and Figure 3.3.8 (b), respectively. All the Nb-doped samples show an obvious enhancement of $(PF)_{eng}$ compared to the undoped sample. For $(ZT)_{eng}$, the

highest values are obtained in samples doped with 0.5% Nb. The output power density and leg efficiency are calculated using $(PF)_{eng}$ and $(ZT)_{eng}$, respectively, by also taking into account the Thomson effect. The output power ω_{max} and efficiency η_{max} are calculated from the following equations,

$$\omega_{\max} = \frac{1}{4}\frac{\left(T_H - T_C\right)^2}{L_{leg}}\left(PF\right)_{eng} \tag{3.3.6}$$

$$\eta_{\max} = \eta_C \frac{\sqrt{1+\left(ZT\right)_{eng}\left(\alpha_1/\eta_C\right)}-1}{\alpha_0\sqrt{1+\left(ZT\right)_{eng}\left(\alpha_1/\eta_C\right)}+\alpha_2} \tag{3.3.7}$$

Where

$$\eta_C = \frac{T_H - T_C}{T_H} \tag{3.3.8}$$

$$\alpha_i = \frac{S_{T_H}\left(T_H - T_C\right)}{\int_{T_C}^{T_H} S(T)dT} - \frac{\int_{T_C}^{T_H}\tau(T)dT}{\int_{T_C}^{T_H} S(T)dT} W_T\eta_C - iW_J\eta_C \quad (i = 0,\ 1,\ 2) \tag{3.3.9}$$

$$\tau = T\frac{dS(T)}{dT} \tag{3.3.10}$$

$$W_T = \frac{\int_{T_C}^{T_H}\int_{T}^{T_H}\tau(T)dTdT}{\Delta T\int_{T_C}^{T_H}\tau(T)dT} \tag{3.3.11}$$

$$W_J = \frac{\int_{T_C}^{T_H}\int_{T}^{T_H}\rho(T)dTdT}{\Delta T\int_{T_C}^{T_H}\rho(T)dT} \tag{3.3.12}$$

in which τ, S_{TH}, η_c, W_T, and W_J are the Thomson coefficient, Seebeck coefficient at hot side, Carnot efficiency, weight factor of Thomson heat, and weight factor of Joule heat, respectively.

As shown in Figure 3.3.8 (c), the output power density increases with the increase of Nb doping concentration till 2.2 at%. At the hot-side temperature of 700 °C, the maximum output power density of ~22 W cm^{-2} is achieved in the sample doped with 2.2 at% Nb which is about 70% higher over the undoped sample. For the leg efficiency shown in Figure 3.3.8 (d), it decreases slowly as the Nb doping concentration increases beyond 0.005 but the leg efficiency of all the doped samples are higher than the undoped sample. The maximum efficiency is about 12% at hot-side temperature of 700 °C in 0.5 at% Nb doped sample and this is about 37% higher than the undoped sample.

3.4 Conclusions

Nb doped $(Hf_{0.25}Zr_{0.75})_{1-x}Nb_xNiSn$ samples (x = 0, 0.005, 0.01, 0.012, 0.014, 0.016, 0.018, 0.02, 0.022, 0.025, and 0.03) are successfully synthesized by ball-milling the arc-melted ingot to form nanopowder and then hot-pressing the nanopowder to get nanostructured bulk samples. With Nb doping, the carrier concentration increases as well as the electrical conductivity indicating that Nb is an effective electron donor in this n-type half-Heusler. The thermoelectric performance of the nanostructured n-type half-Heusler $Hf_{0.25}Zr_{0.75}NiSn$ can be enhanced by Nb doping. With optimized carrier concentration, a peak ZT ~0.9 at 700 °C is achieved in samples with Nb doping from 1.8 at% to 2.2 at%. Both the power factor of ~47 μW cm^{-1} K^{-2} and peak ZT of ~0.9 are comparable to the reported best n-type MNiSn half-Heuslers with ZT around 1 that are doped with Sb [25, 26]. The advantage of Nb over Sb doping is that the experiments are more controllable, since Sb has high vapor pressure and evaporates a lot during arc-melting and Nb doesn't have such problems. Besides, the Nb doped samples can be more thermally stable than Sb

doped ones especially at high temperatures due to the high vapor pressure of Sb. Finally, the calculations of the output power density and leg efficiency demonstrate that the maximum output power density around 22 W cm^{-2} and highest leg efficiency around 12% can be obtained in Nb doped samples. The high output power density of 22 W cm^{-2} with a leg length of 2 mm, a cold-side temperature of 50 °C and a hot-side temperature of 700 °C indicates that our samples are promising thermoelectric materials for high power generation applications.

3.5 Future Perspective

Since vanadium and tantalum are in the same column as niobium on the periodic table and all of them have one more valence electron than Hf/Zr, vanadium and tantalum may also be good dopants for the half-Heusler MNiSn. In the following sections, the results of 1 at% and 2 at% vanadium doping, and 0.5 at%, 1 at%, and 2 at% tantalum doping in $Hf_{0.25}Zr_{0.75}NiSn$ are presented and discussed, respectively. All the samples were synthesized by arc-melting the elements in stoichiometry together to form the ingot first, then ball-milling the ingot into nanopowder, and finally hot-pressing to get the dense bulk sample.

3.5.1 Vanadium Doping in $Hf_{0.25}Zr_{0.75}NiSn$

Figure 3.5.1 shows the thermoelectric properties of $(Hf_{0.25}Zr_{0.75})_{1-x}V_xNiSn$ (x = 0.01 and 0.02) samples and the results are compared to the undoped sample and 1 at% and 2 at% Nb doped ones. With vanadium doping, the electrical conductivity is increased in the whole temperature range from room temperature to 700 ^oC compared to the undoped

sample, which means that vanadium can also act as an electron donor to enhance the carrier concentration in $Hf_{0.25}Zr_{0.75}NiSn$ compound. The electrical conductivity increases when the temperature rises, showing the typical behavior of semiconductors. Comparing to the 1 at% and 2 at% Nb doped samples, the electrical conductivity of vanadium doped ones are much lower. The electrical conductivity of 2 at% vanadium doped sample is even smaller than that of 1 at% Nb doped one. Thus as an electron donor, vanadium is not as strong as Nb. This may be because that vanadium has higher electronegativity than Nb, so vanadium is less likely to donate electrons as Nb.

The Seebeck coefficients (Figure 3.5.1 (b)) of vanadium doped samples are decreased as to the undoped sample due to the increase of carrier concentration. The thermal conductivity (Figure 3.5.1 (d)) is increased by vanadium doping due to the higher electronic thermal conductivity. Both the Seebeck coefficient and the thermal conductivity show strong bipolar effects at around 400 ^{o}C, which are due to the thermal excitation of intrinsic charge carriers. In comparison to the undoped sample, the power factor of vanadium doped ones shows moderate enhancement, as well as the ZT value. However, either the power factor or the ZT value of 1 at% and 2 at% vanadium doping is as high as the 1 at% and 2 at% Nb doping. This is because the electrical conductivity of 1 at% and 2 at% vanadium doped samples is still not high enough, which means that the carrier concentration is still low compared to the optimal value. Therefore, future studies of increasing the vanadium doping concentrations are needed to optimize the electrical properties, so that the ZT can be further enhanced.

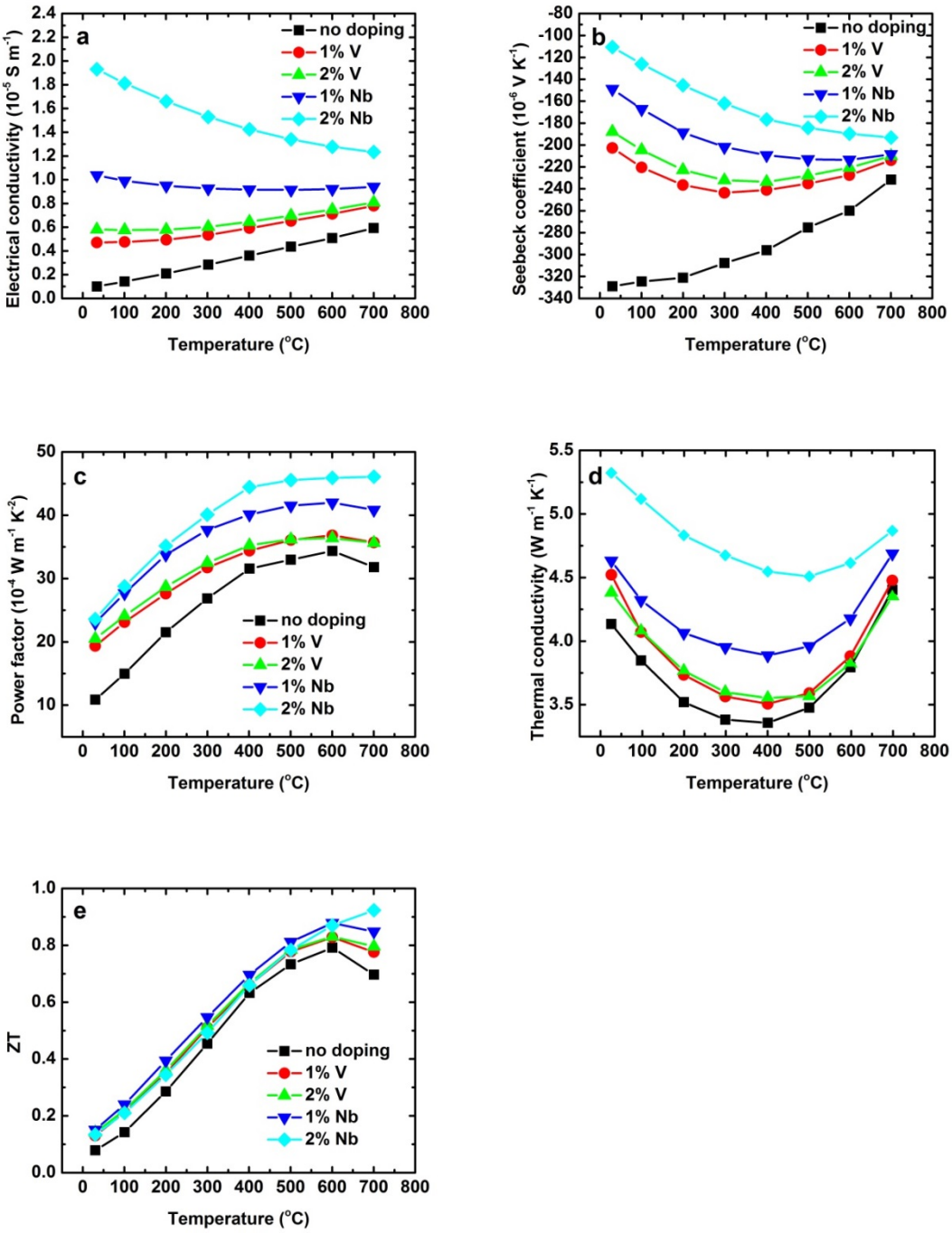

Figure 3.5.1 Temperature-dependent electrical conductivity (a), Seebeck coefficient (b), power factor (c), thermal conductivity (d), and ZT (e) of $(Hf_{0.25}Zr_{0.75})_{1-x}V_xNiSn$ (x= 0, 0.01, and 0.02) samples, compared to $(Hf_{0.25}Zr_{0.75})_{1-x}Nb_xNiSn$ (x = 0.01 and 0.02).

3.5.2 Tantalum Doping in $Hf_{0.25}Zr_{0.75}NiSn$

$(Hf_{0.25}Zr_{0.75})_{1-x}Ta_xNiSn$ (x = 0.005, 0.01, 0.02) samples are also successfully synthesized and their thermoelectric properties are studied. In Figure 3.5.2, the thermoelectric properties of the Ta doped samples are presented and compared to the undoped one and the 2 at% Nb doped sample as well. Figure 3.5.2 (a) shows the temperature-dependent electrical conductivities. Compared to the undoped sample, the electrical conductivity is greatly enhanced by Ta doping. With only 0.5 at% Ta, the electrical conductivity is increased from 0.1 x 10^{-5} S m^{-1} to 1.5 x 10^{-5} S m^{-1} at room temperature. The electrical conductivities of the Ta doped samples decrease with temperature, showing the typical behavior of degenerate semiconductors. At a certain temperature, the higher the Ta doping level, the larger the electrical conductivity is. In comparison to the Nb doped sample, the electrical conductivity of the sample with 1 at% Ta is even higher than the sample doped with 2 at% Nb. Thus Ta is a stronger electron donor than Nb and can increase the carrier concentration more effectively than Nb. This may also be ascribed to the lower electronegativity of Ta than Nb, so Ta can donate electron more easily.

The Seebeck coefficients of all the samples are presented in Figure 3.5.2 (b). The Seebeck coefficient is decreased after Ta doping because of the increase of carrier concentration. When the Ta concentration increases, the Seebeck coefficient keeps decreasing at a certain temperature. For all the Ta doped samples, as temperature rises, the Seebeck coefficient continues increasing. No bipolar effect is noticed here probably because the bipolar effect is suppressed by the high extrinsic carrier concentration. As shown in Figure 3.5.2 (c), the power factors of all the Ta doped samples exhibit large

enhancement compared to the undoped sample over the whole temperature range. The highest power factor of 50 x 10^{-4} W m^{-1} K^{-2} is achieved at 500 ^{o}C and 600 ^{o}C in all the samples with Ta doping despite different doping concentrations. The power factor of Ta doped samples is even higher than the Nb doped one, so Ta is even a better dopant in this $Hf_{0.25}Zr_{0.75}NiSn$ half-Heusler compound.

Figure 3.5.2 (d) shows the temperature-dependent thermal conductivities for all the samples. Compared to the undoped sample, the thermal conductivity is increased with Ta doping due to the increased electronic thermal conductivity. Among the sample with different Ta doping concentration, the higher the doping concentration, the larger the thermal conductivity is. As temperature increases, the thermal conductivity decreases at first and then increases at high temperatures due to the bipolar effect. With higher Ta doping level, the bipolar effects happen at higher temperature because the large extrinsic carrier concentration can suppress the bipolar effect.

The ZT values are calculated and shown in Figure 3.5.2 (e). For the sample doped with 2 at% Ta, due to its high thermal conductivity, the ZT values do not show any improvement except at 700 ^{o}C, compared to the undoped sample. Thus the doping concentration of 2 at% is too large for Ta doping. When the sample is doped with 1 at% Ta, the ZT is increased over the whole temperature range. A peak ZT of 1 is obtained at 700 ^{o}C, this is even higher than the Nb doped samples, so Ta is even more effective in enhancing the thermoelectric properties of $Hf_{0.25}Zr_{0.75}NiSn$ than Nb.

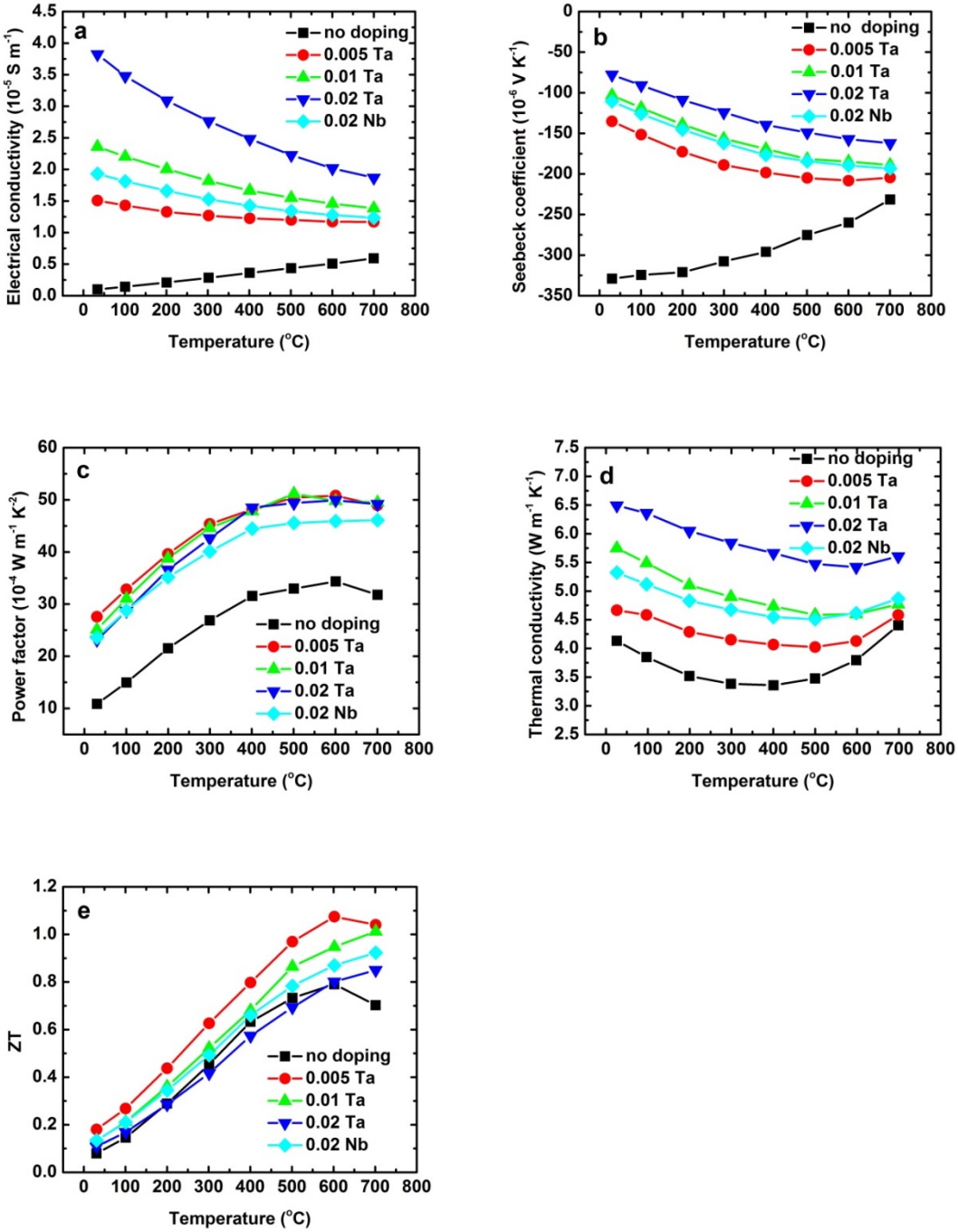

Figure 3.5.2 Temperature-dependent electrical conductivity (a), Seebeck coefficient (b), power factor (c), thermal conductivity (d), and ZT (e) of $(Hf_{0.25}Zr_{0.75})_{1-x}Ta_xNiSn$ (x= 0, 0.005, 0.01, and 0.02) samples, compared to $(Hf_{0.25}Zr_{0.75})_{0.08}Nb_{0.02}NiSn$.

The highest ZT value is achieved in the sample doped with 0.5 at% Ta owing to its lower thermal conductivity. The maximum ZT value of 1.1 is attained at 600 ^{o}C in $(Hf_{0.25}Zr_{0.75})_{0.995}Ta_{0.005}NiSn$, which is even higher than the best reported ZT of 1 in Sb doped MNiSn half-Heuslers. Future studies of finely tuning the Ta doping concentrations can be carried out to further optimize the thermoelectric properties of $Hf_{0.25}Zr_{0.75}NiSn$.

References

[1] S. Öğüt, K.M. Rabe. Physical Review B 51 (1995) 10443.

[2] P. Larson, S. Mahanti, S. Sportouch, M. Kanatzidis. Physical Review B 59 (1999) 15660.

[3] F. Aliev, N. Brandt, V. Moshchalkov, V. Kozyrkov, R. Skolozdra, A. Belogorokhov. Zeitschrift für Physik B Condensed Matter 75 (1989) 167-171.

[4] J. Schmitt, Z.M. Gibbs, G.J. Snyder, C. Felser. Materials Horizons 2 (2015) 68-75.

[5] C. Uher, J. Yang, S. Hu, D.T. Morelli, G.P. Meisner. Physical Review B 59 (1999) 8615-8621.

[6] C. Yu, T. J. Zhu, R. Z. Shi, Y. Zhang, X. B. Zhao, J. He. Acta Materialia 57 (2009) 2757-2764.

[7] H. Xie, H. Wang, C. Fu, Y. Liu, G.J. Snyder, X. Zhao, T. Zhu. Scientific Reports 4 (2014).

[8] J. Krez, J. Schmitt, G.J. Snyder, C. Felser, W. Hermes, M. Schwind. Journal of Materials Chemistry A 2 (2014) 13513-13518.

[9] K. Gałązka, S. Populoh, W. Xie, S. Yoon, G. Saucke, J. Hulliger, A. Weidenkaff. Journal of Applied Physics 115 (2014) 183704.

[10] O. Appel, Y. Gelbstein. Journal of Electronic Materials 43 (2014) 1976-1982.

[11] H. Muta, T. Kanemitsu, K. Kurosaki, S. Yamanaka. Journal of Alloys and Compounds 469 (2009) 50-55.

[12] J.P. Makongo, D.K. Misra, X. Zhou, A. Pant, M.R. Shabetai, X. Su, C. Uher, K.L. Stokes, P.F. Poudeu. Journal of the American Chemical Society 133 (2011) 18843-18852.

[13] S.R. Culp, J. Simonson, S.J. Poon, V. Ponnambalam, J. Edwards, T.M. Tritt. Applied Physics Letters 93 (2008).

[14] S. Ouardi, G.H. Fecher, C. Felser, C.G. Blum, D. Bombor, C. Hess, S. Wurmehl, B. Büchner, E. Ikenaga. Applied Physics Letters 99 (2011) 152112.

[15] C.S. Birkel, W.G. Zeier, J.E. Douglas, B.R. Lettiere, C.E. Mills, G. Seward, A. Birkel, M.L. Snedaker, Y. Zhang, G.J. Snyder. Chemistry of Materials 24 (2012) 2558-2565.

[16] G. Joshi, X. Yan, H. Wang, W. Liu, G. Chen, Z. Ren. Advanced Energy Materials 1 (2011) 643-647.

[17] T. Handbook. Macro to Nano, edited by DM Rowe, CRC Taylor & Francis, Boca Ratcon (2006).

[18] H. H. Xie, J. L. Mi, L. P. Hu, N. Lock, M. Chirstensen, C. G. Fu, B.B. Iversen, X. B. Zhao, T. J. Zhu. CrystEngComm 14 (2012) 4467-4471.

[19] D.T. Do, S.D. Mahanti, J.J. Pulikkoti. Journal of Physics: Condensed Matter 26 (2014) 275501.

[20] J.E. Douglas, P.A. Chater, C.M. Brown, T.M. Pollock, R. Seshadri. Journal of Applied Physics 116 (2014) 163514.

[21] K. Miyamoto, A. Kimura, K. Sakamoto, M. Ye, Y. Cui, K. Shimada, H. Namatame, M. Taniguchi, S. I. Fujimori, Y. Saitoh. Applied Physics Express 1 (2008) 081901.

[22] H. Miyazaki, T. Nakano, M. Inukai, K. Soda, Y. Izumi, T. Muro, J. Kim, M. Takata, M. Matsunami, S. I. Kimura. Materials Transactions 55 (2014) 1209-1214.

[23] Y. Liu, A. Page, P. Sahoo, H. Chi, C. Uher, P.F. Poudeu. Dalton Transactions 43 (2014) 8094-8101.

[24] H.S. Kim, W. Liu, G. Chen, C.-W. Chu, Z. Ren. Proceedings of the National Academy of Sciences 112 (2015) 8205-8210.

[25] G. Joshi, T. Dahal, S. Chen, H. Wang, J. Shiomi, G. Chen, Z. Ren. Nano Energy 2 (2013) 82-87.

[26] S. Chen, K.C. Lukas, W. Liu, C.P. Opeil, G. Chen, Z. Ren. Advanced Energy Materials 3 (2013) 1210-1214.

Chapter 4

Experimental Studies on the Thermoelectric Properties of $Hf_{0.25}Zr_{0.75}NiSn$ Compound

4.1 Effects of Ti Substitution at the Zr Site in $Hf_{0.25}Zr_{0.75}NiSn_{0.99}Sb_{0.01}$

4.1.1 Introduction

In chapter 3, the optimization of the carrier concentration in $Hf_{0.25}Zr_{0.75}NiSn$ by Nb, V, and Ta doping were discussed. In addition to improving the electrical properties by doping, reducing the thermal conductivity is also important for the enhancement of ZT. The n-type half-Heusler compounds MNiSn usually have high thermal conductivity due to their high lattice thermal conductivity (above 4 W m^{-1} K^{-1} at room temperature) [1]. Such high lattice thermal conductivity of half-Heusler compared to other compounds such as Bi_2Te_3 and PbTe will limit the improvement of ZT. Therefore, suppressing the lattice thermal conductivity of half-Heuslers is important, because it can lead to the decrease of total thermal conductivity without deteriorating the electrical properties too much.

Alloying effects which can produce more point defects scattering for phonons have been proven to be effective in reducing the lattice thermal conductivity. Binary or ternary combination of different ratios of Ti, Zr and Hf at the M site of MNiSn can reduce

approximately 50% of the lattice thermal conductivity at room temperature compared to the unalloyed MNiSn [2-5]. Isoelectronic alloy of Pt and Pd at the Ni site can also decrease the lattice thermal conductivity [6, 7]. However, since Pt and Pd are expensive elements, alloying Pt and Pd is not practical in large scale applications.

Another approach to suppress the lattice thermal conductivity is to increase the boundary scattering for phonons by reducing the grain sizes to nanoscale. Bhattacharya et al. reported that by ball-milling and shock compaction the grain size of $TiNiSn_{1-x}Sb_x$ decreased from more than 10 mm to less than 1 mm, which leads to the dramatic reduction of lattice thermal conductivity to 3.7 W m^{-1} K^{-1} [8]. Our group managed to make $Hf_{0.75}Zr_{0.25}NiSn_{0.99}Sb_{0.01}$ nanopowders with a grain size of around 50 nm by high energy ball-milling [9]. With rapid hot pressing, the nanostructure can be preserved in the bulk sample with particle size in the range of 200-300 nm. The lattice thermal conductivity of the nanostructured sample is around 3.5 W m^{-1} K^{-1} which is about 15% reduction compared to the ingot.

In this section, based on the nanostructured $Hf_{0.25}Zr_{0.75}NiSn_{0.99}Sb_{0.01}$ compound, further alloying Ti at the Zr site is discussed. The $Hf_{0.25}Zr_{0.75-x}Ti_xNiSn_{0.99}Sb_{0.01}$ (x = 0, 0.1, 0.2, 0.3) samples were synthesized and their thermoelectric properties were measured. The results show that with 30% Ti the thermal diffusivity at room temperature is decreased from 2.25 mm^2 S^{-1} to 1.77 mm^2 S^{-1}, which is about 21% reduction compared to the one without Ti. The electrical conductivity is also decreased with Ti substitution, leading to the decrease of power factor. As a result, although the thermal conductivity is suppressed by alloying Ti, the ZT value does not have obvious improvement. To have a better understanding of the effects of Ti substitution, three unalloyed samples $TiNiSn_{0.99}Sb_{0.01}$,

$ZrNiSn_{0.99}Sb_{0.01}$, and $HfNiSn_{0.99}Sb_{0.01}$ were synthesized as well. It's found out that $TiNiSn_{0.99}Sb_{0.01}$ sample has much lower electrical conductivity and power factor than the other two samples, which may explain the reason for the worse electrical properties after Ti substitution in $Hf_{0.25}Zr_{0.75}NiSn_{0.99}Sb_{0.01}$ compound.

4.1.2 Experimental Procedures

All the half-Heusler ingots: $Hf_{0.25}Zr_{0.75-x}Ti_xNiSn_{0.99}Sb_{0.01}$ (x = 0, 0.1, 0.2, 0.3), $TiNiSn_{0.99}Sb_{0.01}$, $ZrNiSn_{0.99}Sb_{0.01}$, and $HfNiSn_{0.99}Sb_{0.01}$ were synthesized by arc-melting the Hf chip (99.7%, Alfa Aesar), Zr slug (99.5%, Alfa Aesar), Ti sponge (99.95%, Alfa Aesar), Nb foil (99.97%, Alfa Aesar), Ni slug (99.98%, Alfa Aesar), Sn shot (99.99+%, Alfa Aesar) and Sb rod (99.8%, Alfa Aesar) in stoichiometry. To ensure the homogeneity, the ingots were arc-melted under Ar protection at least three times and flipped over every time. Then the alloyed ingots were directly put into a stainless steel jar with grinding balls and ball-milled for 5 hours. The bulk samples were prepared by hot pressing the nanopowders in a graphite die. After hot-press, the graphite die was taken out immediately to let it cool down slowly. The disks of 12.7 mm in diameter and around 2 mm in thickness were prepared for measurements.

The uncertainties of measurements were estimated to be 3% for thermal diffusivity, specific heat capacity, and electrical conductivity, and 5% for Seebeck coefficient, which results in an uncertainty of 11% for ZT. To increase the readability of all the curves, all the figures are plotted without the error bars.

4.1.3 Results and Discussions

The thermal diffusivities of $Hf_{0.25}Zr_{0.75-x}Ti_xNiSn_{0.99}Sb_{0.01}$ (x = 0, 0.1, 0.2, 0.3) samples are shown in Figure 4.1.1 (a). By Ti substitution, the thermal diffusivity is reduced in the whole temperature range due to the alloying scattering. The higher the Ti concentration, the lower the thermal diffusivity is. With 30% Ti the thermal diffusivity at room temperature is decreased from 2.25 $mm^2\ S^{-1}$ to 1.77 $mm^2\ S^{-1}$, which is about 21% reduction compared to the one without Ti. However at higher temperatures, the decrease of thermal diffusivity is less, because stronger bipolar effects are noticed when Ti concentration increases. The thermal conductivity in Figure 4.1.1 (b) is calculated by multiplying the thermal diffusivity, the density, and the specific heat capacity of each sample. The densities are measured by Archimede's method and listed in Table 4.1.1. The specific heat capacity of the sample $Hf_{0.25}Zr_{0.75}NiSn_{0.99}Sb_{0.01}$ is measured and used to calculate the thermal conductivities for all the samples. With Ti substitution, the specific heat capacity may increase a little bit, so about 5% error should be taken into consideration. From Figure 4.1.1 (b), owning to the alloying effects, the thermal conductivity can be effectively suppressed by Ti substitution for Zr.

Table 4.1.1 Densities of $Hf_{0.25}Zr_{0.75-x}Ti_xNiSn_{0.99}Sb_{0.01}$ (x = 0, 0.1, 0.2, 0.3) samples measured by Archimede's method.

Sample	x = 0	x = 0.1	x = 0.2	x = 0.3
Density (g cm^{-3})	8.438	8.361	8.329	8.273

The electrical conductivity is presented in Figure 4.1.1 (c). The electrical conductivities of the samples with Ti are decreased in the whole temperature range compared to the

original sample without Ti. One reason for this may be there is more alloying scattering for charge carriers so the carrier mobility is decreased. Among the three samples with Ti, although the Ti concentrations are different, the electrical conductivities are almost the same except some small changes at high temperatures. Figure 4.1.1 (d) shows the Seebeck coefficients for the four samples. When temperature increases, the absolute values of Seebeck coefficients first increase and begin to decrease at high temperatures due to the thermal excitation of intrinsic charge carriers, which is called the bipolar effect. The higher the Ti concentration, the earlier the bipolar effects occur. The bandgap of a semiconductor can be estimated from the temperature-dependent Seebeck coefficient measurement by the Goldsmid-Sharp bandgap formula $E_g = 2eS_{max}T_{max}$, where S_{max} is the highest Seebeck coefficient and T_{max} is the temperature when S reaches the maximum value [10]. Accordingly, the bandgaps of the four samples $Hf_{0.25}Zr_{0.75-x}Ti_xNiSn_{0.99}Sb_{0.01}$ are calculated to be 0.37 eV, 0.34 eV, 0.33 eV, and 0.28 eV, when x = 0, 0.1, 0.2, and 0.3, respectively. It demonstrates that the bandgap becomes smaller when more Ti substitutes Zr, which is consistent with theoretical calculations that TiNiSn has smaller bandgap than ZrNiSn [11]. Due to the narrower bandgap, the intrinsic charge carriers are easier to be excited, so the bipolar effects happen at lower temperature when there is more Ti.

The power factors of the four samples are calculated and shown in Figure 4.1.1 (e). Because of the decrease of electrical conductivity, the power factors of all the samples with Ti are decreased. When the Ti concentration increases, the power factor keeps decreasing in the whole temperature range because the Seebeck coefficients also decrease with Ti. The peak of the power factor shifts to lower temperatures due to the bipolar effects.

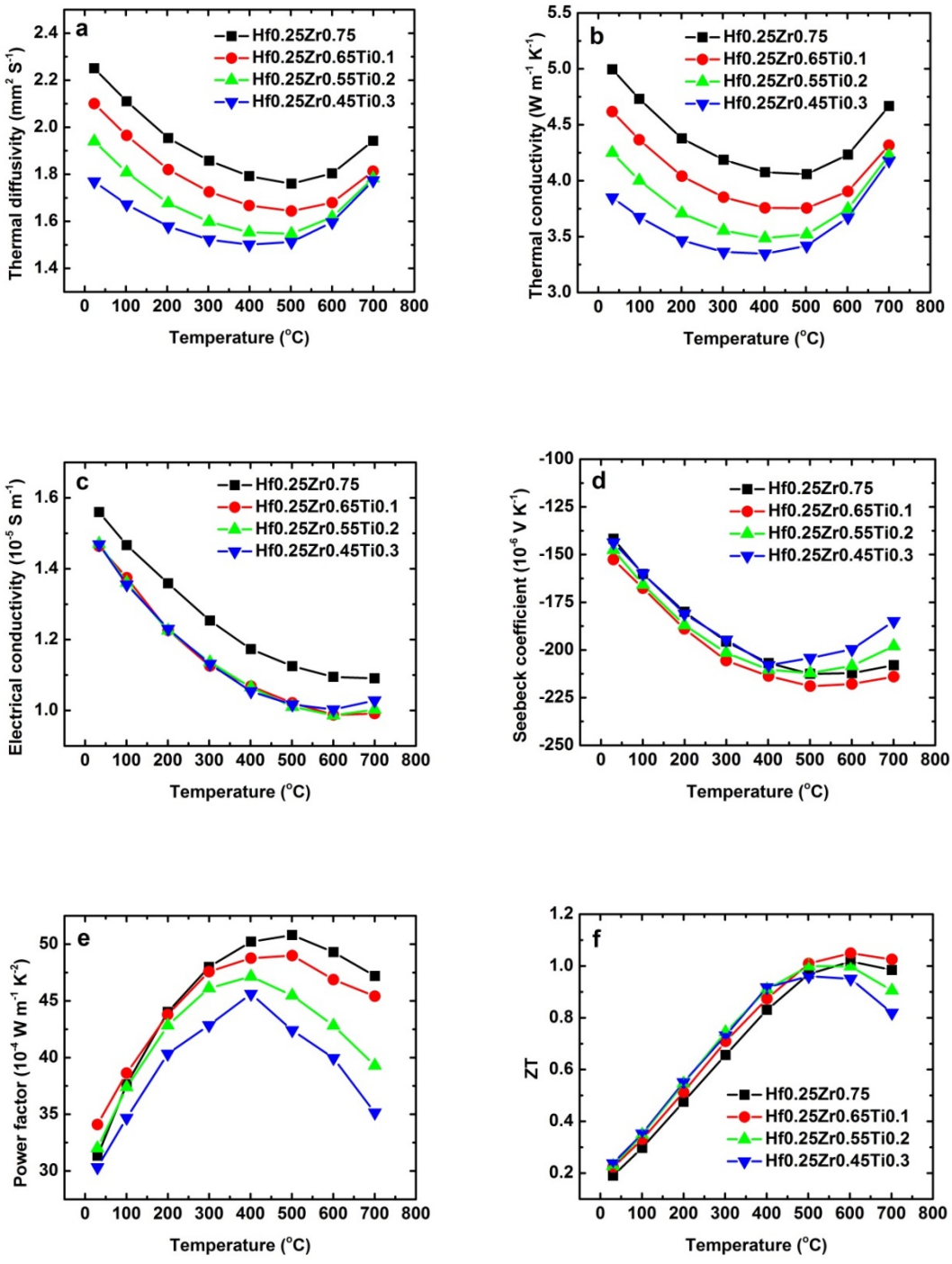

Figure 4.1.1 Temperature-dependent thermal diffusivity (a), thermal conductivity (b), electrical conductivity (c), Seebeck coefficient (d), power factor (e), and ZT (f) of $Hf_{0.25}Zr_{0.75-x}Ti_xNiSn_{0.99}Sb_{0.01}$ (x = 0, 0.1, 0.2, 0.3) samples.

As a result, although the thermal conductivities are suppressed by Ti substitution, the ZT values do not have obvious improvement compared to the one without Ti. As shown in Figure 4.1.1 (f), for the sample alloyed with 10% Ti, the ZT values have a little bit enhancements over the whole temperature range. For the other two samples with 20% and 30% Ti, the ZT values only show some improvement below 500 ^{o}C, and the ZT drops at higher temperatures due to the strong bipolar effects.

$TiNiSn_{0.99}Sb_{0.01}$, $ZrNiSn_{0.99}Sb_{0.01}$, and $HfNiSn_{0.99}Sb_{0.01}$ samples are also synthesized to study the thermoelectric properties of the three half-Heusler compounds without any alloying. Their electrical properties are shown in Figure 4.1.2. For the electrical conductivity (Figure 4.1.2 (a)), $ZrNiSn_{0.99}Sb_{0.01}$ has the highest electrical conductivity over the whole temperature range, and $TiNiSn_{0.99}Sb_{0.01}$ has much lower electrical conductivity than the other two. This may also explain that when Ti substitutes Zr in this n-type Half-Heusler compound, the electrical conductivity decreases. As demonstrated in Figure 4.1.2 (b), $ZrNiSn_{0.99}Sb_{0.01}$ shows smaller Seebeck coefficient at room temperature, followed by $HfNiSn_{0.99}Sb_{0.01.}$ However, at higher temperature, the Seebeck coefficient of $TiNiSn_{0.99}Sb_{0.01}$ is much lower than the other two because of its strong bipolar effects after 400 ^{o}C. The bandgap for the three compounds are also calculated by the Goldsmid-Sharp bandgap formula. The calculated bandgap is 0.30 eV, 0.37 eV, 0.35 eV for $TiNiSn_{0.99}Sb_{0.01}$, $ZrNiSn_{0.99}Sb_{0.01}$, and $HfNiSn_{0.99}Sb_{0.01}$, respectively. As the bandgap of $TiNiSn_{0.99}Sb_{0.01}$ is much smaller than the other two, the bipolar effects occur at lower temperatures, so it shows lower Seebeck coefficient at high temperatures. This result is also consistent with the previous studies that with Ti substitution for Zr in $Hf_{0.25}Zr_{0.75}NiSn_{0.99}Sb_{0.01}$, the bandgap shrinks and the bipolar effects become stronger.

Figure 4.1.2 (c) shows the power factors of the three samples. Both $ZrNiSn_{0.99}Sb_{0.01}$ and $HfNiSn_{0.99}Sb_{0.01}$ have similar values of power factor and the highest value can reach 50 x 10^{-4} W m^{-1} K^{-2} at 500 ^{o}C. However, for $TiNiSn_{0.99}Sb_{0.01}$, the highest power factor is only 40 x 10^{-4} W m^{-1} K^{-2} at 300 ^{o}C, and above 300 ^{o}C, the power factor drops dramatically.

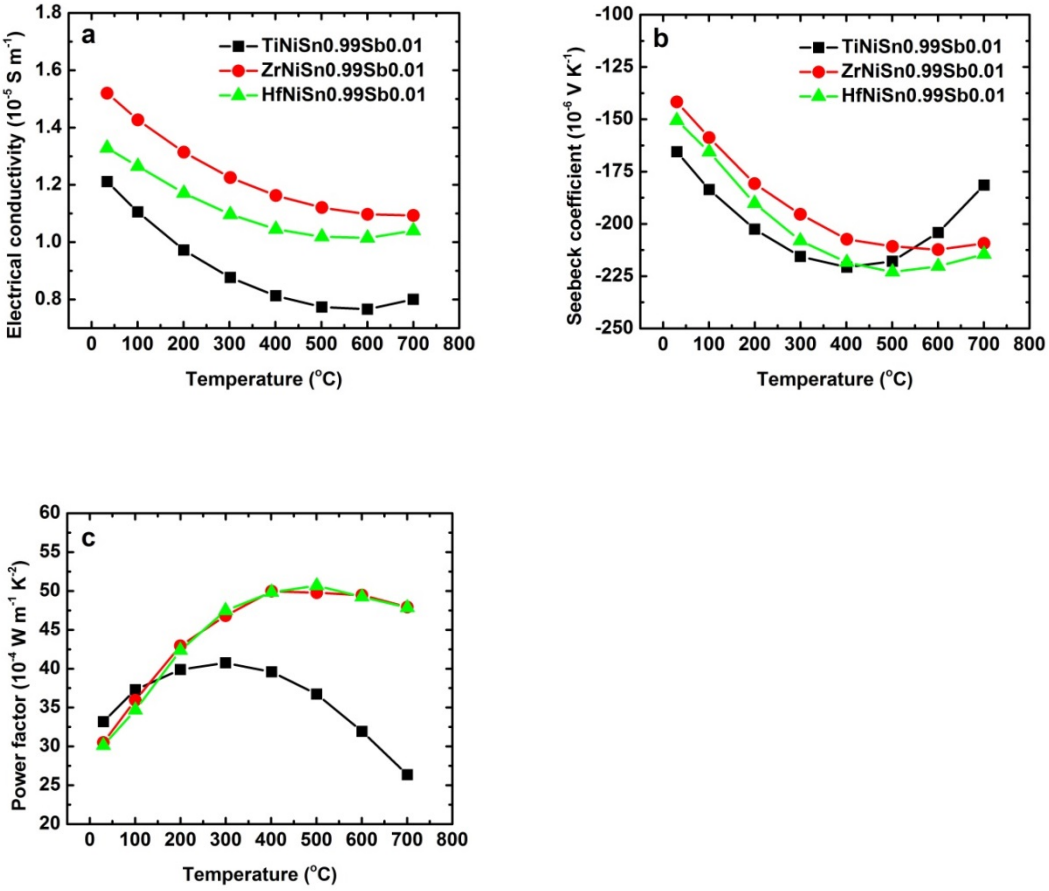

Figure 4.1.2 Temperature-dependent electrical conductivity (a), Seebeck coefficient (b), and power factor (c) of $TiNiSn_{0.99}Sb_{0.01}$, $ZrNiSn_{0.99}Sb_{0.01}$, and $HfNiSn_{0.99}Sb_{0.01}$.

The thermal diffusivities of the three samples are presented in Figure 4.1.3 (a). $TiNiSn_{0.99}Sb_{0.01}$ shows lower thermal diffusivity than the other two, probably because of its lower electronic thermal conductivity. Strong bipolar effect in thermal diffusivity is

also noticed for $TiNiSn_{0.99}Sb_{0.01}$. The thermal diffusivities for $ZrNiSn_{0.99}Sb_{0.01}$ and $HfNiSn_{0.99}Sb_{0.01}$ are similar to each other. Compared to the $Hf_{0.25}Zr_{0.75-x}Ti_xNiSn_{0.99}Sb_{0.01}$ (x = 0, 0.1, 0.2, 0.3) samples, these three samples without alloying have much higher thermal diffusivities. For instance, the thermal diffusivity of $Hf_{0.25}Zr_{0.75}NiSn_{0.99}Sb_{0.01}$ is 2.25 $mm^2\ S^{-1}$ at room temperature, which shows about 40% reduction compared to $ZrNiSn_{0.99}Sb_{0.01}$ or $HfNiSn_{0.99}Sb_{0.01}$ of which the thermal diffusivity is 3.70 $mm^2\ S^{-1}$ at room temperature. It demonstrates again that alloying effects can suppress the thermal diffusivity effectively. Figure 4.1.3 (b) shows the measured specific heat capacity for the three samples. The lighter the element, the larger the specific heat capacity is. The densities of the three samples are listed in Tables 4.1.2. The thermal conductivity is calculated and presented in Figure 4.1.3 (c). $HfNiSn_{0.99}Sb_{0.01}$ has lower thermal conductivity than $ZrNiSn_{0.99}Sb_{0.01}$ because of its lower C_p. $TiNiSn_{0.99}Sb_{0.01}$ shows smaller thermal conductivities at low temperatures, but this advantage diminishes at high temperatures due to the bipolar effects. Finally, the ZT values of the three samples are shown in Figure 4.1.3 (d). Below 400 ^oC, there is not too much difference in ZT among the three samples. However, above 400 ^oC, the ZT values of $ZrNiSn_{0.99}Sb_{0.01}$ and $HfNiSn_{0.99}Sb_{0.01}$ are much higher than $TiNiSn_{0.99}Sb_{0.01}$. The highest ZT value is about 0.8 at 600 ^oC for $HfNiSn_{0.99}Sb_{0.01}$, 0.76 at 700 ^oC for $ZrNiSn_{0.99}Sb_{0.01}$, and 0.56 at 500 ^oC for $TiNiSn_{0.99}Sb_{0.01}$.

Table 4.1.2 Densities of $TiNiSn_{0.99}Sb_{0.01}$, $ZrNiSn_{0.99}Sb_{0.01}$, and $HfNiSn_{0.99}Sb_{0.01}$ samples measured by Archimede's method.

$TiNiSn_{0.99}Sb_{0.01}$	$TiNiSn_{0.99}Sb_{0.01}$	$TiNiSn_{0.99}Sb_{0.01}$	$TiNiSn_{0.99}Sb_{0.01}$
Density (g cm^{-3})	7.173	7.760	10.485

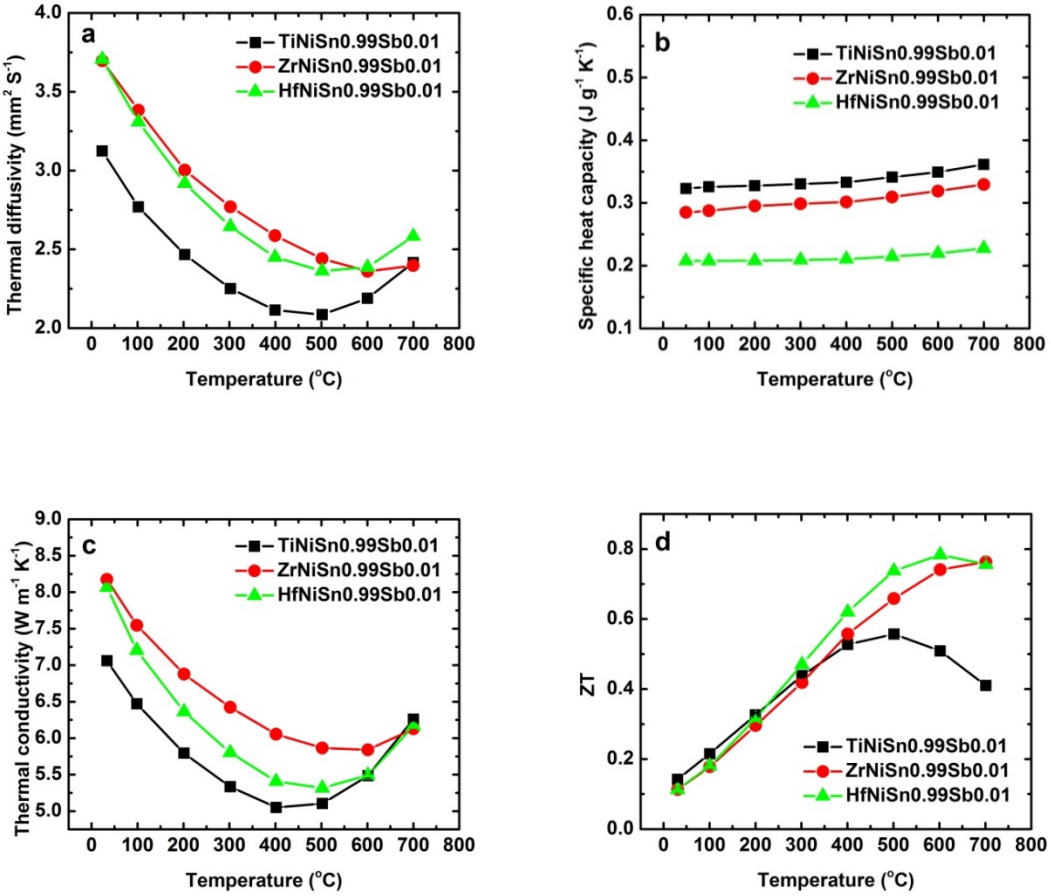

Figure 4.1.3 Temperature-dependent thermal diffusivity (a), specific heat capacity (b), thermal conductivity (c), and ZT (d) of $TiNiSn_{0.99}Sb_{0.01}$, $ZrNiSn_{0.99}Sb_{0.01}$, and $HfNiSn_{0.99}Sb_{0.01}$.

By comparing the thermoelectric properties of the three unalloyed samples, we can see that the thermoelectric properties of $ZrNiSn_{0.99}Sb_{0.01}$ and $HfNiSn_{0.99}Sb_{0.01}$ are closer to each other. Both of them have high power factor of around 50 x 10^{-4} W m^{-1} K^{-2} at 500 ^{o}C and ZT value near 0.8 at 600 ^{o}C or 700 ^{o}C. Thus when binary alloying Hf and Zr, the thermal conductivity can be greatly reduced and at the same time the electrical properties will not change too much, so the ZT can be enhanced [2, 5]. However, the electrical properties of $TiNiSn_{0.99}Sb_{0.01}$ are poorer than the other two. The highest power factor of

$TiNiSn_{0.99}Sb_{0.01}$ is only 40 x 10^{-4} W m^{-1} K^{-2} at 300 ^{o}C, and above 300 ^{o}C, the power factor drops dramatically due to the bipolar effects. Thus when further substitute Zr by Ti in $Hf_{0.25}Zr_{0.75-x}Ti_xNiSn_{0.99}Sb_{0.01}$, although the thermal conductivity can be reduced, the ZT value does not have much improvement due to the decrease of power factor.

4.1.4 Conclusions

In this section, the thermoelectric properties of $Hf_{0.25}Zr_{0.75-x}Ti_xNiSn_{0.99}Sb_{0.01}$ (x = 0, 0.1, 0.2, 0.3) samples are studied. By further alloying Ti at the Zr site, the thermal conductivity can be suppressed and more than 20% reduction in thermal conductivity at room temperature is achieved by alloying 30% Ti. However, the electrical conductivity as well as the power factor is decreased with Ti substitution, so the ZT value does not have obvious improvement. Three unalloyed samples: $TiNiSn_{0.99}Sb_{0.01}$, $ZrNiSn_{0.99}Sb_{0.01}$, and $HfNiSn_{0.99}Sb_{0.01}$ are synthesized and their thermoelectric properties are studied as well. It turns out that $TiNiSn_{0.99}Sb_{0.01}$ has poorer electrical properties than the other two compounds, because the narrower bandgap in $TiNiSn_{0.99}Sb_{0.01}$ leads to strong bipolar effects. This may be the reason for the worse electrical properties when further alloying Ti in $Hf_{0.25}Zr_{0.75-x}Ti_xNiSn_{0.99}Sb_{0.01}$ (x = 0, 0.1, 0.2, 0.3).

4.2 $Hf_{0.25}Zr_{0.75}NiSn$ with InSb Nanoinclusions

4.2.1 Introduction

Besides optimizing the electrical properties by doping with adjacent elements and reducing the thermal conductivity via alloying effects or nanostructuring approaches, another way to enhance the thermoelectric properties of materials is to incorporate some

nanoinclusions into the structure. By introducing secondary phase nanoinclusions, the interface between the nanoinclusions and the matrix can selectively scatter the low energy charge carriers and reduce their contribution to Seebeck coefficient which is called the energy filtering effects [12], so the Seebeck coefficient can be increased. On the other hand, it can create additional boundary scatterings for phonons at the interface between the nanoinclusion and matrix leading to the reduction of lattice thermal conductivity. The simultaneously enhanced Seebeck coefficient and reduced lattice thermal conductivity can effectively improve ZT.

Such method has also been employed in optimizing the thermoelectric properties of half-Heusler compounds. Since full-Heuser phase can be easily formed during the synthesis of half-Heulser compounds by simply increasing the ratio of Ni in MNiSn, incorporating the full-Heusler nanoinclusions into the half-Heusler matrix has been widely studied [13-16]. Makongo et al. reported that by adding 2 at% extra nickel in half-Heusler composition, full-Heusler nanoinclusions were formed which could provide additional scattering for the charge carriers and phonons at the grain boundaries between the half-Heusler matrix and full-Heusler. Therefore the low-energy charge carriers would be filtered out, resulting in 67% increase of Seebeck coefficient, and at the same time about 20% reduction of the lattice thermal conductivity was also noticed compared to the pure half-Heusler matrix [13, 14]. Similarly, incorporating other phase nanoinclusions such as InSb, HfO_2, and ZrO_2 were also reported to be able to enhance the thermoelectric properties of half-Heusler comopunds [17-20].

In this section, the half-Heusler matrixes $Hf_{0.25}Zr_{0.75}NiSn$ with *x* mole InSb nanoinclusions (x = 0, 0.005, 0.01, 0.012, 0.015, 0.018, 0.02) are synthesized and their

thermoelectric properties are studied. Xie et al. reported that by introducing the InSb nanoincluions into the MCoSb based n-type half-Heusler $Ti_{0.5}Hf_{0.25}Zr_{0.25}Co_{0.95}Ni_{0.05}Sb$, the nanoinclusion-induced electron injection and electron filtering mechanisms helped to simultaneously decrease the resistivity and enhance the Seebeck coefficient [17]. A ZT around 0.5 was attained at 820 K for the sample containing 1 at% InSb nanoinclusions, which is a 160% improvement over the sample containing no nanoinclusions. The InSb nanoinclusions have also been reported to be introduced into both the n-type and p-type skutterudites and could effectively enhance the thermoelectric properties [21, 22]. Here we add the InSb into the n-type half-Heusler $Hf_{0.25}Zr_{0.75}NiSn$, both the thermal conductivity and electrical conductivity are increased due to the increase of carrier concentration. High power factor of 55 x 10^{-4} W m^{-1} K^{-2} above 400 ^{o}C is achieved in the sample with 1.8 mol% InSb, which is about 10% higher than that of the reported best n-type half-Heulser doped with Sb. The peak ZT value of 1.15 is attained at 700 ^{o}C in the sample with 1.8 mol% InSb, which is 45% higher than the sample without InSb.

4.2.2 Experimental Procedures

The n-type half-Heusler samples $Hf_{0.25}Zr_{0.75}NiSn$ with *x* mole InSb (x = 0, 0.005, 0.01, 0.012, 0.015, 0.018, 0.02) were firstly synthesized by arc-melting all the elements in $Hf_{0.25}Zr_{0.75}NiSn$ based on the stoichiometry and *x* mol% InSb compound (99.99%, Alfa Aesar) together to form the ingots. To ensure the homogeneity, the ingots were arc-melted under Ar protection at least three times and flipped over every time. Then the alloyed ingots were directly put into a stainless steel jar and ball-milled for 5 hours. The bulk samples were prepared by hot pressing the nanopowders in a graphite die. After hot-

press, the graphite die was taken out immediately to let it cool down slowly. The disks of 12.7 mm in diameter and around 2 mm in thickness were prepared for measurements.

The uncertainties of measurements were estimated to be 3% for thermal diffusivity, specific heat capacity, and electrical conductivity, and 5% for Seebeck coefficient, which results in an uncertainty of 11% for ZT. To increase the readability of all the curves, all the figures are plotted without the error bars.

4.2.3 Results and Discussions

The XRD patterns of all the $Hf_{0.25}Zr_{0.75}NiSn$ samples with *x* mole InSb (*x* = 0, 0.005, 0.01, 0.012, 0.015, 0.018, 0.02) are shown in Figure 4.2.1. All the indexed peaks are corresponding to the cubic half-Heusler phase. No peaks for the InSb phase are found within the detection limit of XRD, perhaps because the ratio of InSb is too low, only up to 2 mol%. Figure 4.2.2 is the low magnification TEM image of the sample with 2 mol% InSb. It shows that the grain sizes are more than 1 μm and there are some small particles on the surface of the grains. The high resolution TEM image (Figure 4.2.2 (b)) is taken on one of the nanoinclusions. The diameter of this nanoinclusion is about 20 nm. The interplanar spacing is labeled in the picture and is about 0.23 nm, which corresponds to the (220) planes of InSb with space group $F\bar{4}3m$. Therefore it demonstrates the existence of InSb nanoinclusions in the samples.

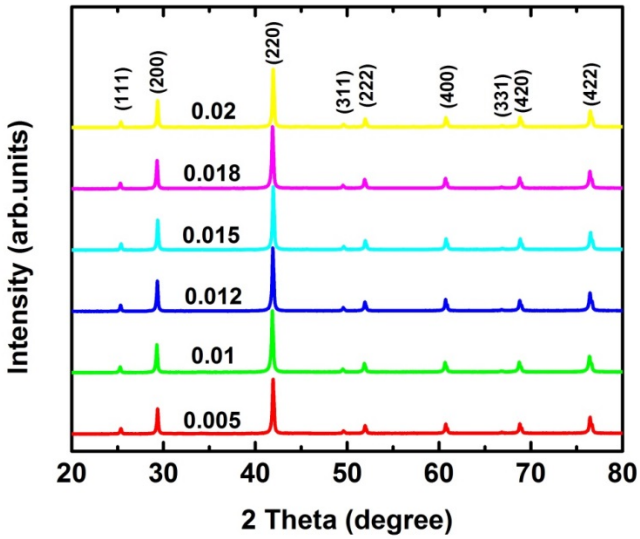

Figure 4.2.1 XRD patterns of $Hf_{0.25}Zr_{0.75}NiSn$ samples with *x* mole InSb (*x* = 0, 0.005, 0.01, 0.012, 0.015, 0.018, 0.02).

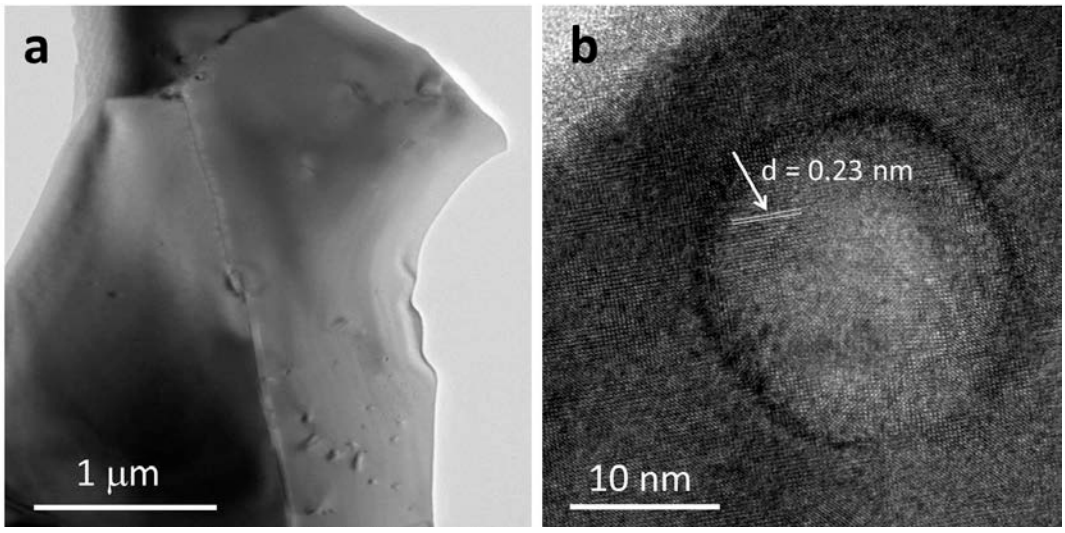

Figure 4.2.2 Low magnification TEM image (a) and high resolution TEM image (b) of $Hf_{0.25}Zr_{0.75}NiSn$ sample with 2 mol% InSb.

The thermal-transport properties are measured and the results are presented in Figure 4.2.3. For the thermal diffusivities (Figure 4.2.3 (a)), as the concentrations of InSb

increase, the thermal diffusivity keeps increasing at a certain temperature. With temperature increasing, the thermal diffusivity decreases at first and then increases at high temperatures due to the bipolar effects. The suppression of bipolar effects can be clearly noticed as the upturn of thermal diffusivity happens at higher temperatures when the InSb concentration increases.

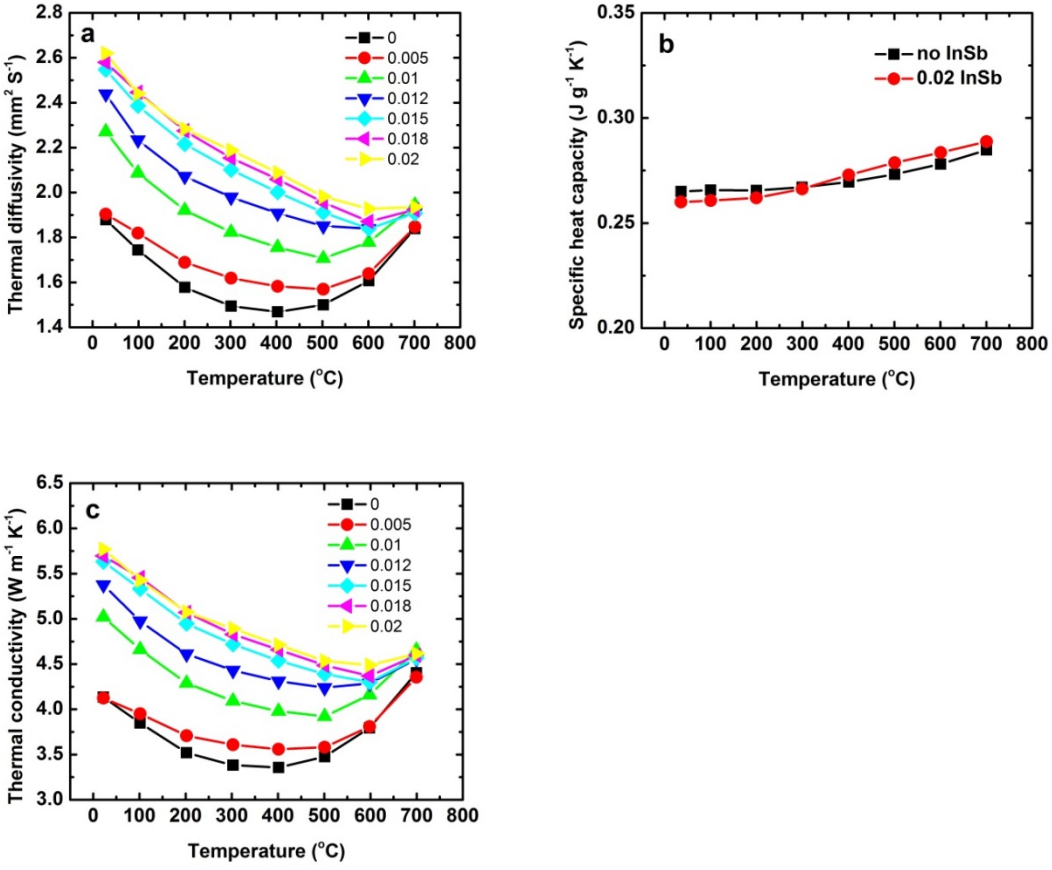

Figure 4.2.3 Temperature-dependent thermal diffusivity (a), specific heat capacity (b), and thermal conductivity (c) of $Hf_{0.25}Zr_{0.75}NiSn$ samples with *x* mole InSb (*x* = 0, 0.005, 0.01, 0.012, 0.015, 0.018, 0.02).

The specific heat capacity (Cp) of the sample with 2 mol% InSb is measured and shown in Figure 4.2.3 (b). Compared to the Cp values of the sample without InSb, the difference between the two is small, so the small amount of InSb doesn't change the Cp too much.

Thus the Cp values of the sample with 2% InSb are used to calculate the thermal conductivity for all the samples with InSb. The densities of the samples are measured by Archimede's method. The densities for $Hf_{0.25}Zr_{0.75}NiSn$ samples with *x* mole InSb (*x* = 0, 0.005, 0.01, 0.012, 0.015, 0.018, 0.02) are 8.479 g/cm^3, 8.347 g/cm^3, 8.407 g/cm^3, 8.382 g/cm^3, 8.41 g/cm^3, 8.395 g/cm^3, 8.373 g/cm^3, respectively. All of samples have a relative density of more than 98%. The thermal conductivity shown in Figure 4.2.3 is calculated by multiplying the thermal diffusivity, the density, and the Cp for each sample. The thermal conductivity increases when InSb concentration increases due to the higher electronic thermal conductivity.

The temperature-dependent electrical conductivities for all the samples are shown in Figure 4.2.4 (a). At a certain temperature, the higher the InSb concentration, the lager the electrical conductivity is. For the samples without InSb and with 0.5% InSb, the electrical conductivity increases when the temperature increases showing the typical behavior of semiconductors. When the samples are with more than 1 mol% InSb, the electrical conductivities decrease with temperature, which exhibits characteristics of degenerate semiconductors. The Hall carrier concentrations and Hall mobility at room temperature of all the samples are measured and listed in Table 4.2.1. As the InSb concentration increases, the Hall carrier concentration becomes larger. In fact, the carrier concentration of InSb is small (~ 10^{18} cm^{-3}). The reason for the increase of carrier concentration may come from the nanoinclusion-induced electron injection, as illustrated in the literature [17]. Another reason may be that some InSb react with $Hf_{0.25}Zr_{0.75}NiSn$ and Sb goes into the compound as the n-type electron donor. The Hall carrier mobility of the samples with InSb is enhanced compared to the sample without InSb, because InSb has high carrier

mobility (~ 10^3 cm^2 V^{-1} S^{-1}). The carrier mobility increases at first and then decreases with higher InSb concentration probably due to more boundary scatterings for carriers from the interface between half-Heusler matrix and InSb nanoinclusions.

Table 4.2.1 Hall carrier concentration and Hall mobility at room temperature of $Hf_{0.25}Zr_{0.75}NiSn$ samples with *x* mole InSb (x = 0, 0.005, 0.01, 0.012, 0.015, 0.018, 0.02).

InSb concentration (mole%)	0	0.01	0.012	0.015	0.018	0.02
Carrier concentration (10^{20} cm^{-3})	0.17	1.81	2.36	3.04	3.44	3.87
Mobility (cm^2 V^{-1} S^{-1})	37.5	42.2	42.5	43.0	42.0	38.3

Figure 4.2.4 (b) is the temperature-dependent Seebeck coefficient. As the ratio of InSb increases, the Seebeck coefficient at a certain temperature decreases owning to the higher carrier concentration. When the InSb concentration is low, the Seebeck coefficient increases with temperature at first and then decreases due to the bipolar effects. As the InSb concentration is higher than 1.2 mol%, the Seebeck coefficient keeps increasing in the whole temperature range because the bipolar effects can be suppressed by large extrinsic carrier concentration. The power factor is shown in Figure 4.2.4 (c). All the samples with InSb exhibit much higher power factor than the sample without InSb. At a fixed temperature, the power factor keeps increasing with InSb ratio until the InSb concentration reaches 1.8 mol%. With 2 mol% InSb, the power factor starts to decrease probably because the carrier concentration is too large. As a result, the highest power factor is achieved in the sample with 1.8 mol% InSb. High power factor of 55 x 10^{-4} W

m^{-1} K^{-2} above 400 ^{o}C is attained, which is around 60% enhancement compared to the sample without InSb.

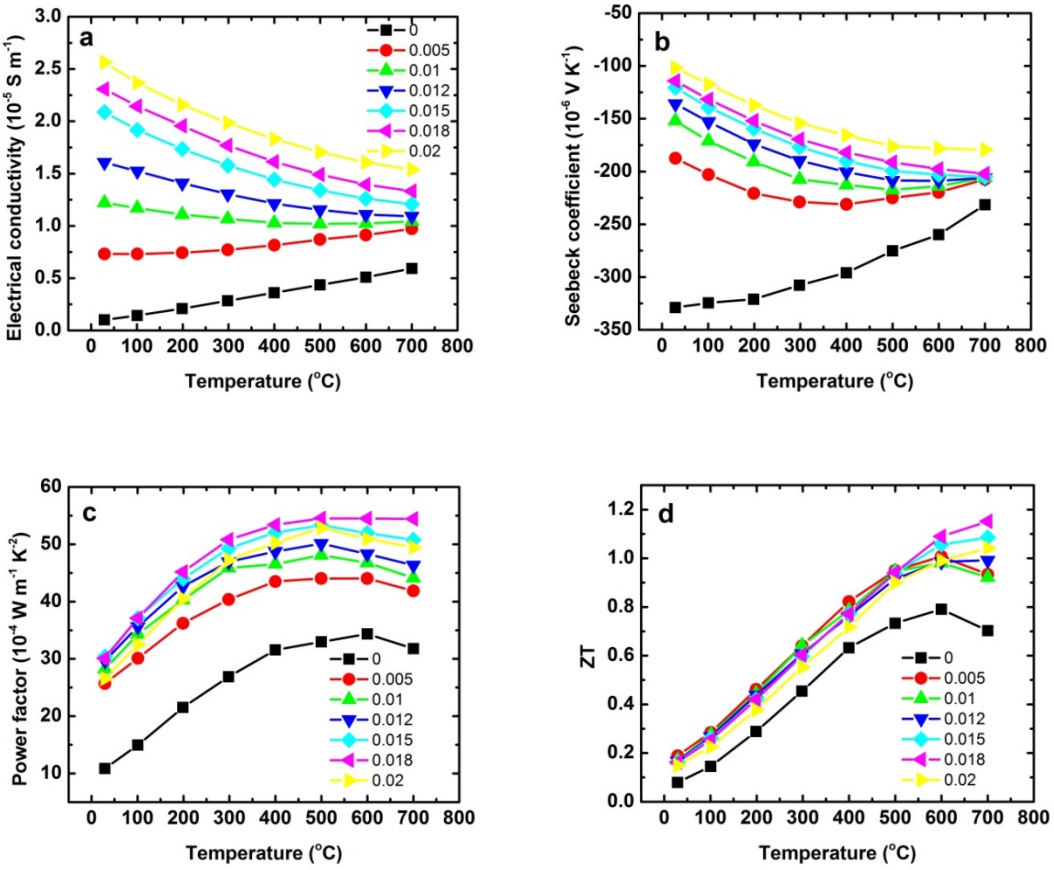

Figure 4.2.4 Temperature-dependent electrical conductivity (a), Seebeck coefficient (b), power factor (c), and ZT (d) of $Hf_{0.25}Zr_{0.75}NiSn$ samples with *x* mole InSb (*x* = 0, 0.005, 0.01, 0.012, 0.015, 0.018, 0.02).

The ZT values are presented in Figure 4.2.4 (d). Although the thermal conductivity is increased with InSb, the power factor is increased much more, so all the samples with InSb show enhanced ZT compared to the sample without InSb. Among the samples with InSb, the ZT values do not have too much difference below 500 ^{o}C. Above 500 ^{o}C, the samples with 1.5 mol% and 1.8 mol% InSb have higher ZT due to the suppressed bipolar effects. When the InSb concentration reaches 2 mol%, the ZT begins to decrease due to

the too large carrier concentration. The highest ZT value of 1.15 is achieved at 700 ^{o}C in the sample with 1.8 mol% InSb. This ZT value is even higher than the reported best n-type half-Heuslers doped with Sb, of which the peak ZT value is around 1.

4.2.4 Conclusions

The samples with nominal composition $Hf_{0.25}Zr_{0.75}NiSn$ with *x* mole InSb (*x* = 0, 0.005, 0.01, 0.012, 0.015, 0.018, 0.02) are prepared by the process of arc-melting, ball-milling, and hot-pressing. The existence of InSb nanoinclusions in the samples is confirmed by the TEM analysis. Both the carrier concentration and carrier mobility are enhanced with InSb, so the electrical conductivity as well as the thermal conductivity is greatly increased. The carrier concentration is optimized with different ratios of InSb. The highest power factor is achieved in the sample with 1.8 mol% InSb, and the peak value is 55 x 10^{-4} W m^{-1} K^{-2} at above 400 ^{o}C, which shows around 60% enhancement compared to the sample without InSb. The ZT values are also improved with InSb nanoinclusions. The peak ZT value of 1.15 is achieved at 700 ^{o}C in the sample with 1.8 mol% InSb, which is 45% higher than the sample without InSb. Therefore, the InSb nanoinclusions can effectively enhance the thermoelectric properties of this n-type half-Heusler $Hf_{0.25}Zr_{0.75}NiSn$.

4.3 Thermal Stability Test of $Hf_{0.25}Zr_{0.75}NiSn_{0.99}Sb_{0.01}$

4.3.1 Introduction

Half-Heusler (HH) compounds are well-known for their high thermoelectric performance in the middle to high temperature range from 500 °C to 700 °C, which is close to the

temperature of most industrial waste heat sources. The high power factors of around 50 x 10^{-4} W m^{-1} K^{-2} at 500 ^{o}C and 600 ^{o}C make half-Heusler compounds great candidates in power generation applications. In real applications, the long-term stability is required for the materials. Although the half-Heusler compounds are known to have good thermal stability, there are only a few reports about the thermal stability tests for half-Heuslers. Krzysztof Galazka et al. first reported the phase formation, stability, and oxidation in $Ti_{0.33}Zr_{0.33}Hf_{0.33}NiSn$ half-Heusler compounds [23]. They found that the as-prepared samples consisted of Ti- and (Zr,Hf)-rich phases within the half-Heusler structure, and the Ti-rich HH phase decomposed after 10 h heat treatment at 600 ^{o}C. Their TG tests in air revealed that the samples started to be oxidized at around 300 ^{o}C, and after heat treatment at 600 ^{o}C for about 5 hours, the sample weight didn't change too much anymore. However, they did not report the changes of the thermoelectric properties before and after heat treatment. Later J. Krez et al. studied the long-term stability of n-type $Ti_{0.3}Zr_{0.35}Hf_{0.35}NiSn$ and p-type $Ti_{0.26}Sc_{0.04}Zr_{0.35}Hf_{0.35}NiSn$ after 500 cycles (1700 h) from 100 ^{o}C to 600 ^{o}C in quartz ampules under vacuum [24]. Their samples are made by arc-melting followed by annealing. The phase separations into Ti-rich and Ti-poor phases were also noticed and such structures were preserved after cycling. They studied the thermoelectric properties as well, and found that the samples were stable even after 500 cycles.

In this section, we discuss the results of heat treatment for $Hf_{0.25}Zr_{0.75}NiSn_{0.99}Sb_{0.01}$ samples in air at 600 ^{o}C for 1 day, 3 days, and 7 days, respectively. The $Hf_{0.25}Zr_{0.75}NiSn_{0.99}Sb_{0.01}$ samples were prepared by arc-melting, ball-milling, and hot-pressing, and their grain sizes are on the nanoscale. It is always doubtful whether the

criteria of thermal stability can be met by nanostructured materials especially under operating at high temperatures. Here the thermal stability of the nanostructured half-Heulser compounds is studied for the first time. The backscattering electron mode (BSE) SEM images of the samples show homogeneous compositions and the thickness of the oxidation layer is about 20 – 30 μm after annealing in air. Although the grain size keeps increasing with annealing time, the thermoelectric properties do not change even after 7 days annealing. Therefore, the high thermal stability of the nanostructured $Hf_{0.25}Zr_{0.75}NiSn_{0.99}Sb_{0.01}$ samples is confirmed.

4.3.2 Experimental Procedures

The $Hf_{0.25}Zr_{0.75}NiSn_{0.99}Sb_{0.01}$ ingot was made by arc-melting the elements according to the stoichiometry. Then the alloyed ingot was put into a stainless steel jar and ball-milled for 5 hours to get nanopowders. To have a reliable comparison, four samples for the annealing test were prepared by hot pressing the nanopowders ball-milled from the same ingot and the hot-pressing conditions were kept the same. Four disks of 12.7 mm in diameter and around 2 mm in thickness were prepared. All the samples were polished before the heat treatment. Three samples were put into the furnace and kept at 600 ^{o}C for 1 day, 3 days, and 7 days, respectively. All of them were exposed in air during the heat treatment. The BSE-SEM images were taken on the cross-section of the samples to study the oxidation. The SEM images of the fracture surface of the four samples were also taken to find out the grain sizes. The samples were polished to get rid of the oxidized surfaces before the measurements of thermoelectric properties. The thermal diffusivity,

electrical conductivity, and Seebeck coefficient of the four samples were measured, respectively.

The uncertainties of measurements were estimated to be 3% for thermal diffusivity and electrical conductivity, and 5% for Seebeck coefficient, which results in an uncertainty of 11% for ZT. To increase the readability of all the curves, all the figures are plotted without the error bars.

4.3.3 Results and Discussions

Figure 4.3.1 shows the BSE-SEM images of the $Hf_{0.25}Zr_{0.75}NiSn_{0.99}Sb_{0.01}$ samples annealed in air at 600 ^{o}C for 1 day (a), 3 days (b), and 7 days (c). The grey layer at the edge of the sample in the images is the oxidized layer. After air annealing for 1 day, there is already a thick layer oxidized, and the thickness of the oxidation layer is around 20 – 30 μm. However, as the annealing time increases, the thickness of the oxidation layer doesn't grow any more. Even after 7 days annealing, the thickness of the oxidized layer is still 20 – 30 μm. The formed oxidation layer can probably prevent the oxygen further diffusing into the sample, and protect the sample to some extent. At the sample side, it is noteworthy that the composition of all the samples is homogeneous, and no phase separation is observed in our samples. This is because there is no Ti in the composition, so the problem of decomposition of the Ti-rich phase after heat treatment as illustrated in the literature [23] will not exist in our case.

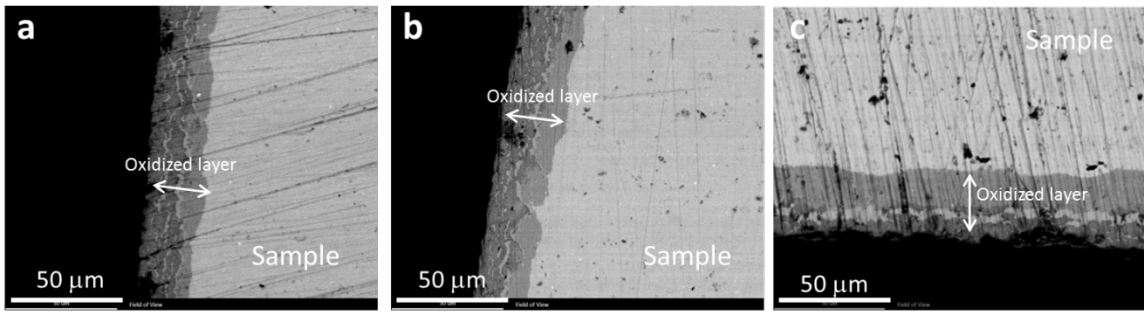

Figure 4.3.1 Backscattering electron mode (BSE) SEM images of $Hf_{0.25}Zr_{0.75}NiSn_{0.99}Sb_{0.01}$ samples annealed in air at 600 ^{o}C for 1 day (a), 3 days (b), and 7 days (c).

The SEM images of the freshly fractured surface of the four samples are taken and presented in Figure 4.3.2. As shown in Figure 4.3.2 (a), the grain size of the $Hf_{0.25}Zr_{0.75}NiSn_{0.99}Sb_{0.01}$ sample without heat treatment ranges from several hundred nanometers to micrometers. As the annealing time increases, the grain size keeps growing. For the sample annealed at 600 ^{o}C for 7 days (Figure 4.3.2 (d)), the average grain size is much large than the sample without heat treatment. Large grains of several micrometers are observed in the last sample (Figure 4.3.2 (d)), and at the same time some small grains of less than 1 micrometer are still preserved after 7 days annealing. Here the samples are annealed at 600 ^{o}C. In thermoelectric modules, the hot site temperature is 600 ^{o}C, but the cold site temperature can be around 50 ^{o}C. There is temperature gradient in the thermoelectric leg, so the grain size will not grow such fast in applications.

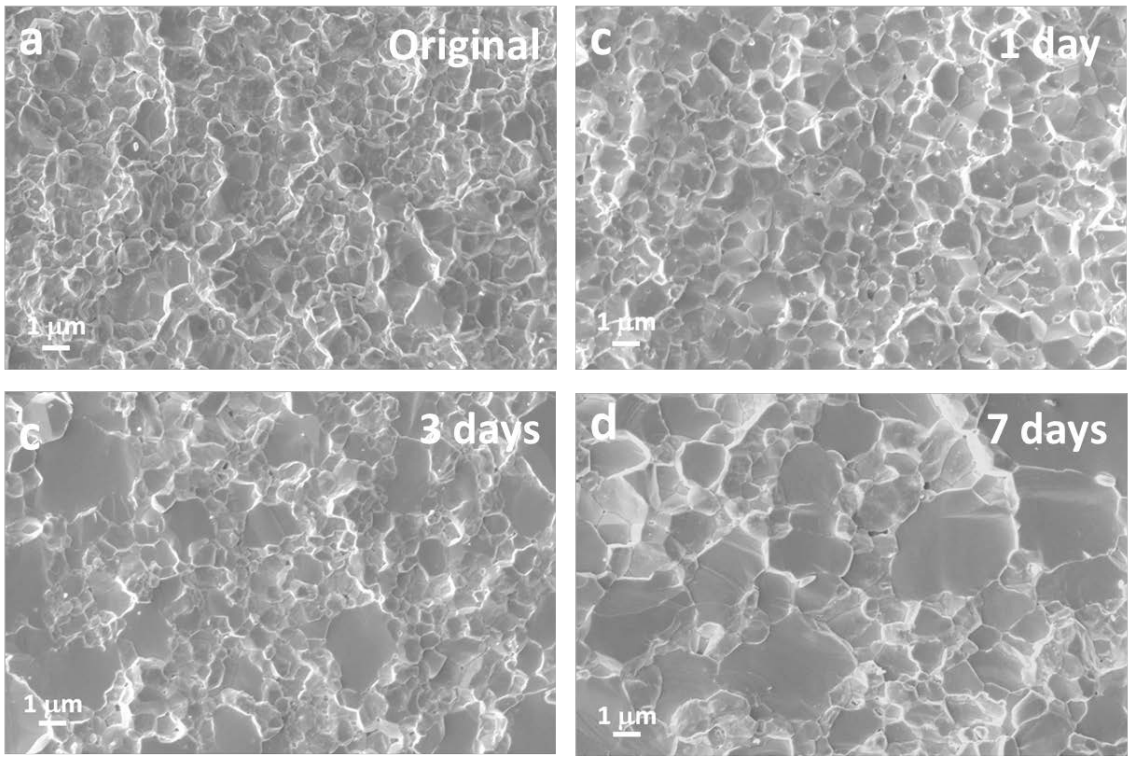

Figure 4.3.2 SEM images of $Hf_{0.25}Zr_{0.75}NiSn_{0.99}Sb_{0.01}$ sample as prepared (a), and annealed in air at 600 ^{o}C for 1 day (b), 3 days (c), and 7 days (d).

The thermoelectric properties are measured for all the samples. Figure 4.3.3 (a) shows the thermal conductivities. Although the grain size is increased after annealing, the thermal conductivities are almost the same over the whole temperature range for all the samples. This may be because there are still some nanosized grains preserved even after 7 days annealing as shown in Figure 4.3.2 (d), they can still provide enough boundary scatterings for phonons. The electrical properties are also measured. Both electrical conductivity and Seebeck coefficient show little changes for all the four samples with different annealing time. It means that the compositions of the samples are very stable during heat treatment, so that the thermoelectric properties can be kept the same. On the other side, the changes in grain size do not have effects on the electrical properties as

well. As a result, both the power factor and ZT values are unchanged after annealing. It demonstrates that the $Hf_{0.25}Zr_{0.75}NiSn_{0.99}Sb_{0.01}$ samples have great thermal stabilities.

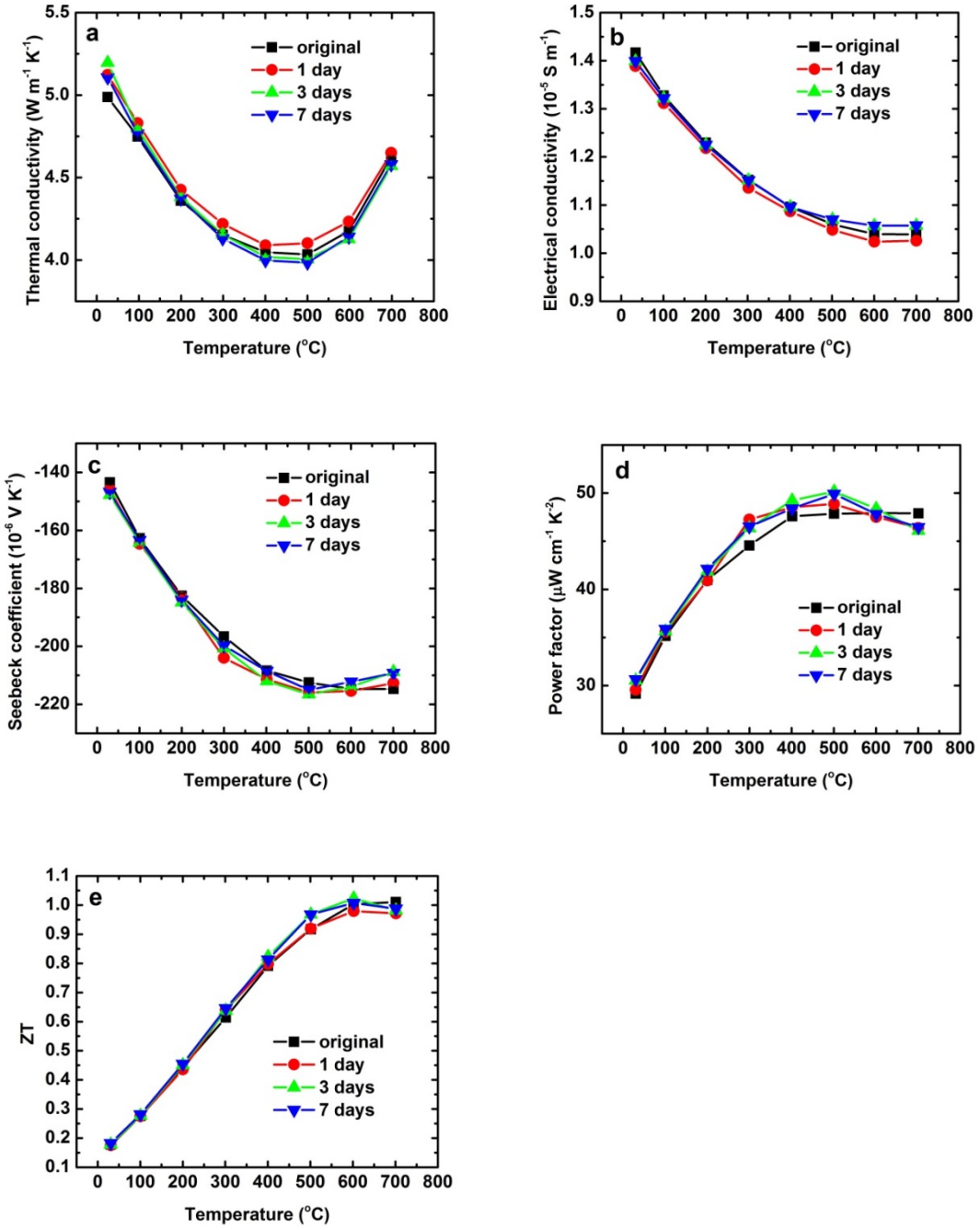

Figure 4.3.3 Temperature-dependent thermal conductivity (a), electrical conductivity (b), Seebeck coefficient (c), power factor (d), and ZT (e) of $Hf_{0.25}Zr_{0.75}NiSn_{0.99}Sb_{0.01}$ sample as prepared, and annealed in air at 600 °C for 1 day, 3 days, and 7 days.

4.3.4 Conclusions

To study the thermal stability, four $Hf_{0.25}Zr_{0.75}NiSn_{0.99}Sb_{0.01}$ samples were prepared under the same conditions. Three of them were annealed in air at 600 ^{o}C for 1 day, 3 days, and 7 days respectively. The BSE-SEM images reveal that the surfaces of the samples are oxidized during the heat treatment. The thickness of the oxidation layer is around 20 – 30 μm, and the thickness doesn't grow as the annealing time is increased from 1 day to 7 days. The SEM image of the sample without annealing shows that the grain size ranges from several hundred nanometers to micrometers. As the annealing time increases, the grain size keeps increasing. Some large grain sizes of several micrometers are observed for the sample heated for 7 days. However, the thermoelectric properties of the four samples are the same, which means that the changes of grain sizes are still not enough to affect the thermoelectric properties yet. It also demonstrates that the $Hf_{0.25}Zr_{0.75}NiSn_{0.99}Sb_{0.01}$ samples have good thermal stabilities. Future work of even longer annealing time is needed to find out how large the grain size will grow and what's the grain size that will have influence on the thermoelectric properties of the samples.

References

[1] C. Uher, J. Yang, S. Hu, D.T. Morelli, G.P. Meisner. Physical Review B 59 (1999) 8615-8621.

[2] C. Yu, T. J. Zhu, R. Z. Shi, Y. Zhang, X. B. Zhao, J. He. Acta Materialia 57 (2009) 2757-2764.

[3] Y. Kimura, H. Ueno, Y. Mishima. Journal of Electronic Materials 38 (2009) 934-939.

[4] G. Joshi, T. Dahal, S. Chen, H. Wang, J. Shiomi, G. Chen, Z. Ren. Nano Energy 2 (2013) 82-87.

[5] S. Chen, K.C. Lukas, W. Liu, C.P. Opeil, G. Chen, Z. Ren. Advanced Energy Materials 3 (2013) 1210-1214.

[6] H. Xie, H. Wang, Y. Pei, C. Fu, X. Liu, G.J. Snyder, X. Zhao, T. Zhu. Advanced Functional Materials 23 (2013) 5123-5130.

[7] Q. Shen, L. Chen, T. Goto, T. Hirai, J. Yang, G. Meisner, C. Uher. Applied Physics Letters 79 (2001) 4165-4167.

[8] S. Bhattacharya, T.M. Tritt, Y. Xia, V. Ponnambalam, S. Poon, N. Thadhani. Applied Physics Letters 81 (2002) 43-45.

[9] G. Joshi, X. Yan, H. Wang, W. Liu, G. Chen, Z. Ren. Advanced Energy Materials 1 (2011) 643-647.

[10] H. Goldsmid, J. Sharp. Journal of Electronic Materials 28 (1999) 869-872.

[11] J. Yang, H. Li, T. Wu, W. Zhang, L. Chen, J. Yang. Advanced Functional Materials 18 (2008) 2880-2888.

[12] A. Minnich, M. Dresselhaus, Z. Ren, G. Chen. Energy & Environmental Science 2 (2009) 466-479.

[13] J.P. Makongo, D.K. Misra, J.R. Salvador, N.J. Takas, G. Wang, M.R. Shabetai, A. Pant, P. Paudel, C. Uher, K.L. Stokes. Journal of Solid State Chemistry 184 (2011) 2948-2960.

[14] J.P. Makongo, D.K. Misra, X. Zhou, A. Pant, M.R. Shabetai, X. Su, C. Uher, K.L. Stokes, P.F. Poudeu. Journal of the American Chemical Society 133 (2011) 18843-18852.

[15] Y. Liu, P. Sahoo, J.P. Makongo, X. Zhou, S. J. Kim, H. Chi, C. Uher, X. Pan, P.F. Poudeu. Journal of the American Chemical Society 135 (2013) 7486-7495.

[16] Y. Liu, A. Page, P. Sahoo, H. Chi, C. Uher, P.F. Dalton Transactions 43 (2014) 8094-8101.

[17] W. Xie, J. He, S. Zhu, X. Su, S. Wang, T. Holgate, J. Graff, V. Ponnambalam, S. Poon, X. Tang. Acta Materialia 58 (2010) 4705-4713.

[18] L. Chen, X. Huang, M. Zhou, X. Shi, W. Zhang. Journal of Applied Physics 99 (2006) 064305.

[19] S.J. Poon, D. Wu, S. Zhu, W. Xie, T.M. Tritt, P. Thomas, R. Venkatasubramanian. Journal of Materials Research 26 (2011) 2795-2802.

[20] C. C. Hsu, Y. N. Liu, H. K. Ma. Journal of Alloys and Compounds 597 (2014) 217-222.

[21] H. Li, X. Tang, Q. Zhang, C. Uher. Applied Physics Letters 94 (2009) 102114.

[22] G. Tan, H. Chi, W. Liu, Y. Zheng, X. Tang, J. He, C. Uher. Journal of Materials Chemistry C 3 (2015) 8372-8380.

[23] K. Gałązka, S. Populoh, L. Sagarna, L. Karvonen, W. Xie, A. Beni, P. Schmutz, J. Hulliger, A. Weidenkaff. Physica Status Solidi (a) 211 (2014) 1259-1266.

[24] J. Krez, B. Balke, S. Ouardi, S. Selle, T. Höche, C. Felser, W. Hermes, M. Schwind. Physical Chemistry Chemical Physics 17 (2015) 29854-29858.

Chapter 5

Synthesis and Thermoelectric Properties of N-type Half-Heusler Compound VCoSb with Valence Electron Count of 19

A part of this chapter contains our previously published work: “Synthesis and thermoelectric properties of n-type half-Heusler compound VCoSb with valence electron count of 19”, *Journal of Alloys and Compounds* (2016) 654, 321-326.

5.1 Introduction

All the well-known half-Hesuler compositions for thermoelectric applications such as MNiSn and MCoSb have 18 valence electron count (VEC) per unit cell. Theoretical studies have predicted that for half-Heusler compounds ABX, as a consequence of the larger distance between the B atoms compared to the Heusler phase, the overlap of the d wave functions is weaker, resulting in formation of energy gaps in the density of states spectra [1, 2]. The electrical transport properties of these compounds are directly related to the number of VEC. When VEC = 18, half-Heusler compounds with filled valence band and empty conduction band are semiconductors. On the other hand, with one more or one less VEC, the Fermi level will enter the valence band (for VEC = 17) or conduction band (for VEC = 19) resulting in metallic properties [1-3]. Because good thermoelectric materials are usually narrow band gap semiconductors, half-Heusler

compounds with VEC = 19 are thought to be metallic and are seldom considered for any possibility as thermoelectric materials till the recent report on the thermoelectric properties of NbCoSb as the first reported n-type half-Heusler with 19 VEC [4].

In this paper, we report our experimental results on another half-Heusler compound VCoSb with VEC = 19. Previous studies on the magnetic and electrical transport properties of VCoSb below room temperatures have been reported by K. Kaczmarska et al. [5]. From their measurement, the electrical conductivity at room temperature is around 2.7 x 10^5 S m^{-1} which is consistent with our room temperature electrical conductivity. Here for the first time we report the thermoelectric properties of VCoSb at high temperatures. Our results demonstrate that VCoSb with half-Heusler phase shows characteristics of semiconductor with electrical conductivity ranging from 2.6 to 1.3 x 10^5 S m^{-1} throughout the temperature range between room temperature and 700 °C. The Seebeck coefficient is negative with a maximum value around -130 μV/K at 600 °C indicating that it acts like an n-type semiconductor. The samples with nanostructures were prepared by arc-melting and ball-milling followed by hot-pressing. Different hot-pressing temperatures result in different porosities, leading to variations of individual properties, but the maximum thermoelectric figure-of-merit (ZT) around 0.5 is achieved in all the nanostructured samples. By 2 at% Sn doping at the Sb site or 2 at% Ti doping at the V site, the ZT value can be further enhanced to 0.56 at 700 ^oC.

5.2 Experimental Procedures

Half-Heusler ingot of VCoSb was synthesized by arc-melting vanadium pieces (99.7%, Alfa Aesar), cobalt pieces (99.9+%, Alfa Aesar), and antimony rod (99.8%, Alfa Aesar)

in stoichiometry. To ensure the homogeneity, the ingot was arc-melted under Ar protection at least three times and flipped over every time. Then the alloyed ingot was directly put into a stainless steel jar with grinding balls and ball-milled for 5 hours to 9 hours (SPEX 8000M Mixer/Mill). The bulk samples were prepared by hot pressing the nanopowders at 750 °C, 800 °C, and 900 °C in a graphite die, respectively. After hot-pressing, the graphite die was taken out immediately to let it cool down slowly. The disks of 12.7 mm in diameter and around 2 mm in thickness were prepared for measurements. On the other hand, another ingot sample was made by annealing the arc-melted ingot at 700 °C for 60 hours for comparison with the ball-milled nanostructured samples.

The volumetric densities of the samples were measured by Archimede's method. The thermal diffusivities were measured on disks by a laser flash equipment (LFA457, Netzsch). Samples were also cut into about 2 x 2 x 12 mm bars for electrical conductivity and Seebeck coefficient measurements on a commercial equipment (ZEM3, Ulvac). The specific heat capacity measurements were performed on a differential scanning calorimeter (DSC 404 C, Netzsch). The carrier concentrations were obtained by Hall measurements on a Physical Property Measurement System (Quantum design). The samples were also characterized by XRD (X'pert PRO PANalytical diffractometer with a Cu Ka radiation source), SEM (LEO 1525), and TEM (JEOL 2100F) to study their crystallinity and grain size. The measurement errors were estimated to be 3% for electrical conductivity, 5% for Seebeck coefficient, 3% for thermal diffusivity, and 3% for specific heat capacity, which results in an uncertainty of 11% for ZT. For better readability, all the figures are plotted without error bars.

5.3 Results and Discussions

5.3.1 Hot-pressing Temperature

5.3.1.1 Phases and Microstructures

The X-ray diffraction (XRD) patterns of the ingot sample and three VCoSb samples hot pressed at 750 °C, 800 °C, and 900 °C are shown in Figure 5.3.1. All the indexed peaks match well with the peaks of cubic half-Heusler phase. The lattice parameter deduced from the XRD pattern is about 5.7955 Å which is consistent with the value of 5.796 Å in the database.

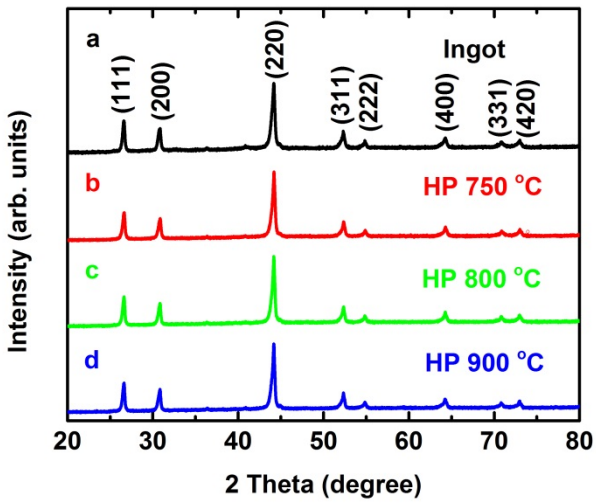

Figure 5.3.1 XRD patterns of the ingot sample (a) and three VCoSb samples hot-pressed at 750 °C (b), 800 °C (c), and 900 °C (d).

Table 5.3.1 lists the actual densities and relative densities of the samples. It clearly shows that the higher the hot-pressing temperature, the denser the sample is. The relative

densities are calculated by dividing each density with the theoretical value of 7.903 g cm^{-3}. When the hot-pressing temperature reaches 800 °C, the relative density is greater than 95%.

Table 5.3.1 Experimentally measured, actual and relative densities of ingot and three VCoSb samples hot pressed at 750 °C, 800 °C, and 900 °C.

Sample	Ingot	HP 750 °C	HP 800 °C	HP 900 °C
Density (g cm^{-3})	7.617	7.477	7.629	7.671
Theoretical density (g cm^{-3})	7.903	7.903	7.903	7.903
Relative density (%)	96.38	94.61	96.53	97.06

The scanning electron microscope (SEM) images in Figure 5.3.2 shows the fractured surface of the samples hot-pressed at 750 °C (a), 800 °C (b), and 900 °C (c), respectively. For all the three samples, the grain size ranges from less than 100 nm to several hundred nanometers. The wide distribution of the grain size may be owing to the non-uniform grinding and high hot-press temperature for which the nanoparticles grow rapidly. Comparing the SEM images of the three samples, the one hot-pressed at 900 °C shows relatively higher compaction, and the other two samples have some porosity. The TEM image of the sample hot-pressed at 800 °C shown in Figure 5.3.2 (d) confirms the grain size observed in the SEM image. Figure 5.3.2 (e) is the high resolution TEM image that demonstrates the clean grain boundaries and good crystallinity of individual grains. Fast Fourier Transformation diffractogram of the selected area is presented in the inset in Figure 5.3.2 (e) which is indexed as the half-Heusler structure oriented along the [213] zone axis.

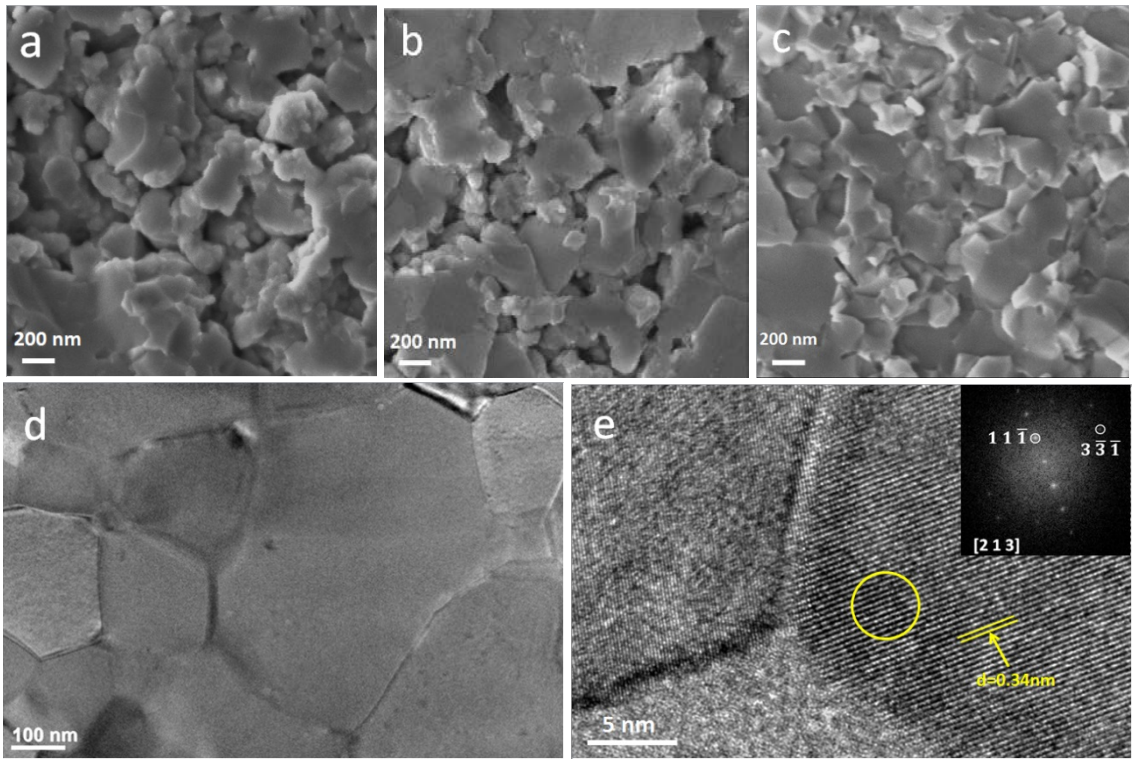

Figure 5.3.2 SEM image of the VCoSb samples hot-pressed at 750 °C (a), 800 °C (b), and 900 °C (c), TEM images at medium (d) and high (e) resolution of the sample hot-pressed at 800 °C. The inset in image (e) is the Fast Fourier Transformation diffractogram of the selected area.

5.3.1.2 Thermal Properties

The specific heat capacity (Cp) of all the samples are measured and shown in Figure 5.3.3 (a). The difference of Cp values among the three samples hot pressed at different temperatures is less than 3% which is within the measurement error of DSC. The Cp increases steadily from 0.32 J g^{-1} K^{-1} at room temperature to 0.35 J g^{-1} K^{-1} at 500 °C, but above 600 °C, Cp increases sharply from 0.36 J g^{-1} K^{-1} at 600 °C to 0.41 J g^{-1} K^{-1} at 700 °C. Figure 5.3.3 (b) is the temperature-dependent thermal diffusivity of the samples. The thermal diffusivity decreases as the temperature increases which is due to the

declining of the relaxation time for phonons. However, after 500 °C, the diffusivity drops even more, which is in consistence of the sharp change of Cp.

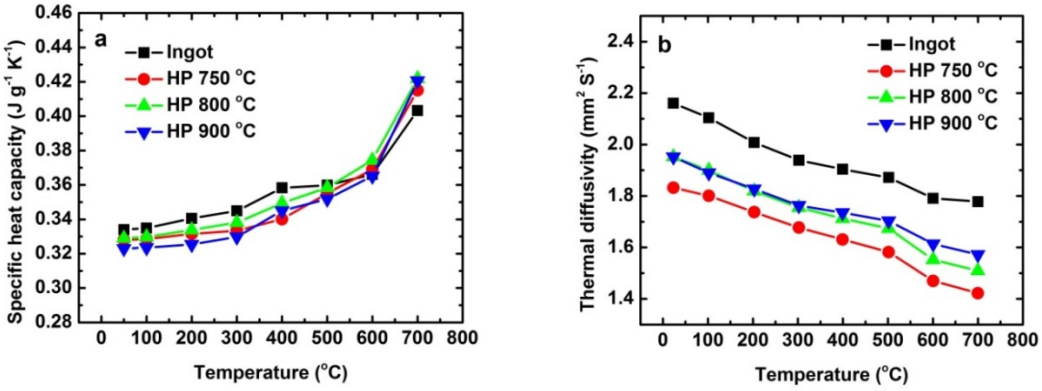

Figure 5.3.3 Temperature-dependent specific heat capacity (a), and thermal diffusivity (b) of ingot and three VCoSb samples hot-pressed at 750 °C, 800 °C, and 900 °C.

To find out whether this change comes from the evaporation of Sb at high temperatures, a thermogravimetric measurement was carried out and the result is shown in Figure 5.3.4. It reveals the mass is constant from room temperature to 700 °C, so the abrupt increase of Cp and thermal conductivity at high temperatures is not caused by the evaporation of Sb.

The change at high temperatures may be due to the atomic disorders. Some literatures pointed out that since V has smaller atomic volumes than other 3d metals which occupies the X position such as Ti, the closer atomic radius between V and Co may cause strong atomic disorder between V and Co [1, 5]. Especially at higher temperatures, the atomic disorder may become much stronger so the thermal diffusivity decreases more after 500 °C.

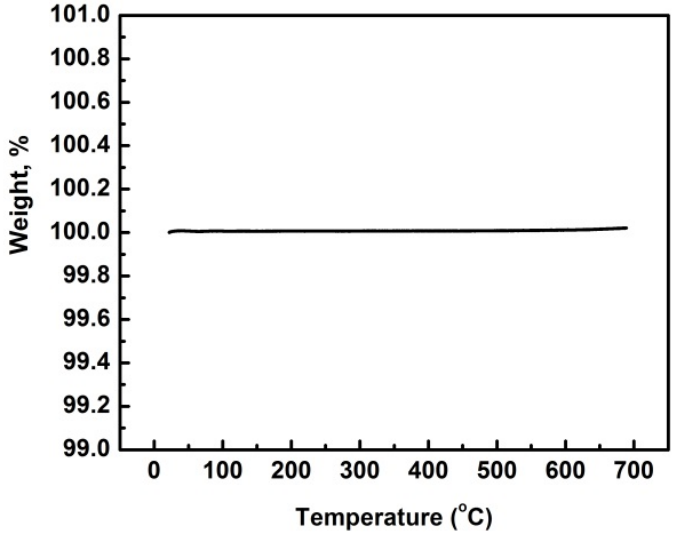

Figure 5.3.4 Thermogravimetric analysis result of the nanostructured VCoSb sample hot-pressed at 800 °C.

Compared to the ingot sample, the thermal diffusivities of the nanostructured samples are much lower, which demonstrates that the additional ball-milling and hot-pressing process can effectively reduce the grain size to increase the boundary scattering of phonons. The samples hot-pressed at lower temperatures have lower thermal diffusivity owing to its relatively higher porosity. The thermal conductivity shown in Figure 5.3.5 is calculated by multiplying the density, the specific heat, and the thermal diffusivity. The thermal conductivity drops after 500 °C and then rises after 600 °C, owning to the decreasing of the diffusivity and the sharp increasing of Cp.

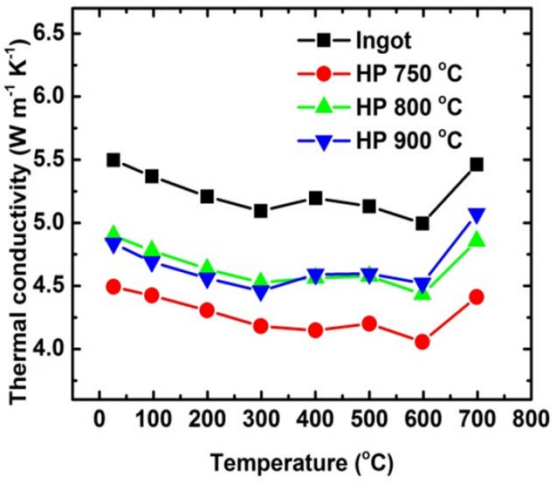

Figure 5.3.5 Temperature-dependent thermal conductivity of ingot and three VCoSb samples hot-pressed at 750 °C, 800 °C, and 900 °C.

5.3.1.3 Electrical Properties and Figure of Merit ZT

The temperature-dependent electrical conductivity (a), Seebeck coefficient (b), power factor (c), and the calculated ZT (d) are shown in Figure 5.3.6. For all the samples, the electrical conductivity first decreases as the temperature rises because of the scattering of the electrons, which exhibit metallic or degenerated semiconductor behaviors. Then the electrical conductivity begins increasing after 600 °C which may be due to the thermal excitation of the intrinsic charge carriers. The electrical conductivities of nanostructured samples are smaller than the ingot because of the additional scattering of the charge carriers by the nanograin boundaries. For all the three samples hot-pressed at different temperatures, at a certain temperature of measurement, the electrical conductivity is higher when the hot-pressing temperature increases because of the higher compaction density.

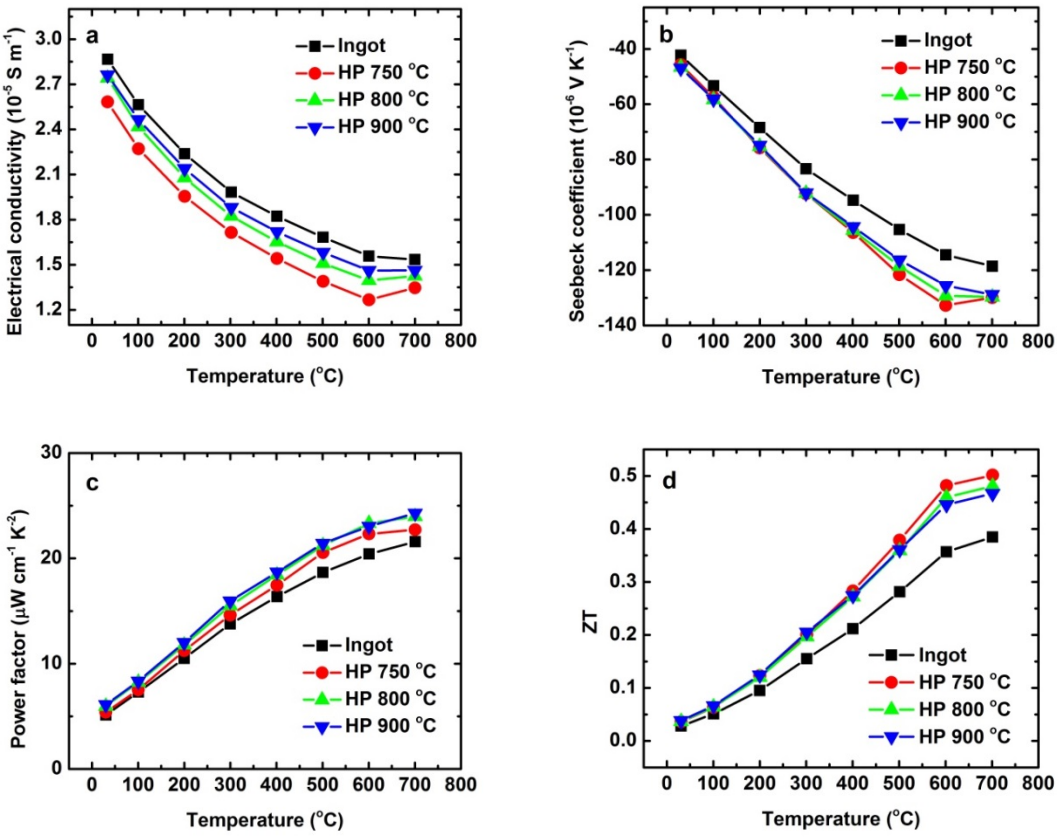

Figure 5.3.6 Temperature-dependent electrical conductivity (a), Seebeck coefficient (b), power factor (c), and ZT (d) of ingot and three VCoSb samples hot-pressed at 750 °C, 800 °C, and 900 °C.

As to the Seebeck coefficient, it increases with temperature before 600 °C and then increases slower or decrease because of the bipolar effect. The values for all the hot-pressed samples are almost the same, and only show some minor deviations at high temperatures. The Seebeck coefficient is also enhanced for the nanostructured samples compared to the ingot. As a result, the power factor ($S^2\sigma$) increases in the whole temperature range and the nanostructured samples have improved values than the ingot. The samples hot-pressed at 800 °C and 900 °C having similar peak values around 25 μW cm^{-1} K^{-2} at 700 °C and slightly higher than the one hot-pressed at 750 °C. The ZT values

are presented in Figure 5.3.6 (d). Nearly 30% enhancement is noticed for the nanostructured samples compared to the ingot, owing to the reduced thermal conductivity and the improved power factor. Below 500 °C, the ZT values are almost the same for all the nanostructured samples. Due to the lower thermal conductivity, the sample hot-pressed at lower temperature show slightly higher ZT values at higher temperatures. After all, the maximum ZT about 0.5 is achieved at above 600 °C for all the nanostructured samples.

Table 5.3.2 Carrier concentration and mobility at room temperature of ingot and three VCoSb samples hot-pressed at 750 °C, 800 °C, and 900 °C.

Sample	Ingot	HP 750 °C	HP 800 °C	HP 900 °C
Carrier concentration (10^{22} cm^{-3})	1.97	1.44	1.6	1.86
Electrical conductivity (10^{5} S m^{-1})	2.87	2.58	2.74	2.76
Mobility (cm^{2} V^{-1} S^{-1})	0.91	1.12	1.07	0.93

The carrier concentrations are obtained from Hall measurements at room temperature and the carrier mobility μ is calculated by the equation $\mu = \sigma/(ne)$, where σ, n, and e are electrical conductivity, carrier concentration, and elementary charge, respectively. The results are presented in Table 5.3.2. The carrier concentrations of all the samples are not much different. However, the nanostructured samples do have a little bit lower carrier concentration than the ingot which indicates that the grain boundaries may be trapping the electrons where low energy electrons could be preferentially scattered, which also explains that the Seebeck coefficient is enhanced for the nanostructured samples. The carrier concentration of VCoSb samples (on the order of 10^{22} cm^{-3}) is much higher than

other half-Heusler compounds such as MNiSn based samples for which the carrier concentration is on the order of 10^{20} cm^{-3} even after doping to increase the carrier concentration. Because theoretical studies demonstrate that half-Heuslers with VEC = 19 would show metallic properties because they have one electron in the conduction band, the theoretical carrier concentration accordingly is estimated to be about 2 x 10^{22} cm^{-3}. Our measured carrier concentration is consistent with the theoretical results. However, the carrier mobility of our samples is extremely low compared to other half-Heusler compounds such as MNiSn, for which the carrier mobility is 30 – 40 cm^2 V^{-1} S^{-1}. As a result, the values of electrical conductivity of VCoSb are comparable to semiconductors.

5.3.2 Ball-milling Time

Different ball-milling time has also been carried out to try to optimize the synthesis process. The synthesis conditions were the same for all the three samples except the ball-milling time. Ball-milling time of 5 hours, 7 hours, and 9 hours was tried respectively. Figure 5.3.7 shows the SEM images of the freshly fractured surface of the three samples. By increasing the ball-milling time, the grain sizes are more uniform and the average grain size is smaller.

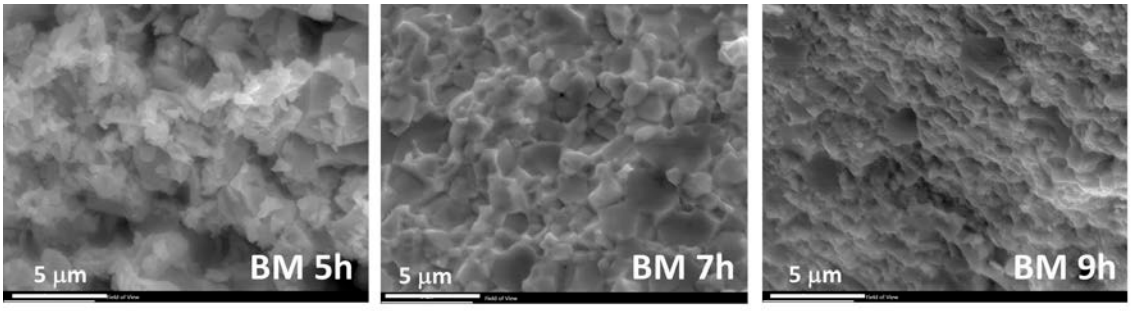

Figure 5.3.7 SEM images of the VCoSb samples ball-milled for 5 hours, 7 hours, and 9 hours.

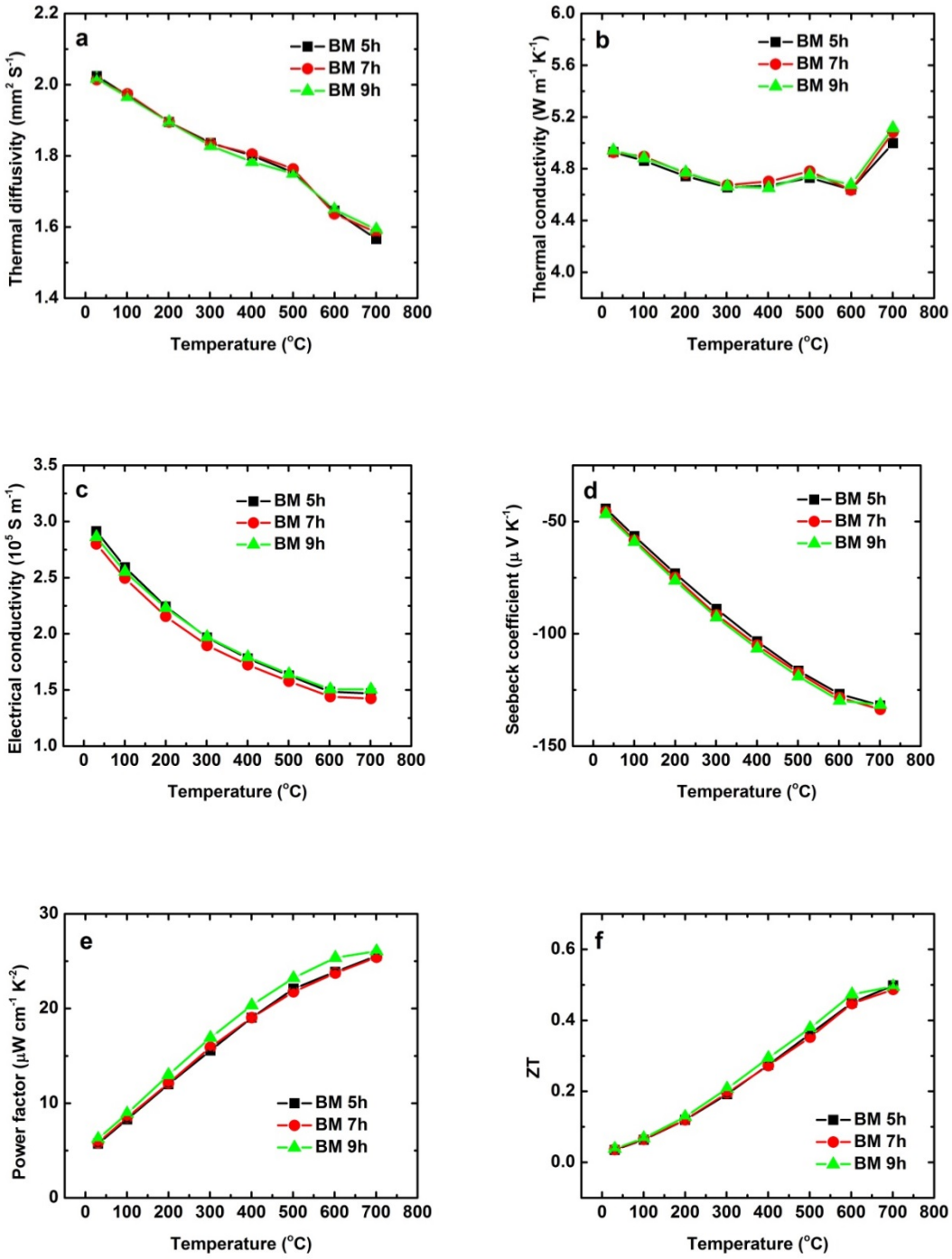

Figure 5.3.8 Temperature-dependent thermal diffusivity (a), thermal conductivity (b), electrical conductivity (c), Seebeck coefficient (d), power factor (e), and ZT (f) of VCoSb samples ball-milled for 5 hours, 7 hours, and 9 hours.

Figure 5.3.8 presents the temperature-dependent thermoelectric properties of the three samples with different ball-milling time. It shows that the thermal conductivity, electrical conductivity, and Seebeck coefficient are almost the same among the three samples, so changing the ball-milling time does not have a big influence on the thermoelectric properties. The densities of the three samples ball-milled for 5 hours, 7 hours, and 9 hours are 7.577 g cm^{-3}, 7.607 g cm^{-3}, and 7.618 g cm^{-3}, respectively. All of them have a relative density of more than 95%. Comparing to the results of different hot-pressing temperatures, we can see that the when the relative density of the nanostructured samples are more than 95%, their thermoelectric properties are close to each other. Therefore the porosity of the samples plays a more important role in determining the thermoelectric properties of the nanostructured VCoSb samples than the small change in the particle size, as long as the particle size is on the scale of hundreds of nanometers.

5.3.3 Effects of Annealing

As we mentioned above, there may exist V and Co atomic disorder in VCoSb. Such atomic disorder may lead to variations in the thermal and electrical properties. Thus we annealed one of the nanostructured samples trying to reduce the defects in the sample. The annealing process was carried out by sealing the sample in a vacuumed quartz tube, putting it into a furnace, and holding it at 700 °C for 24 hours. Figure 5.3.9 presents the thermoelectric properties of the same sample before and after annealing. There are no obvious changes of all the properties before and after annealing. Only the thermal conductivity of the annealed sample is increased at room temperature which may be due to the reduction of phonon scattering from defects. The thermal and electrical properties

do not change at high temperatures and the sharp change of thermal diffusivity after 500 ^{o}C can still be observed, so the atomic disorder may not be caused by the ball-milling and hot-pressing process. Perhaps such disorder is intrinsic and thermodynamically stable in this VCoSb compound. Detailed structural analysis and calculations are needed in further studies to figure out whether there is such atomic disorder in the VCoSb samples.

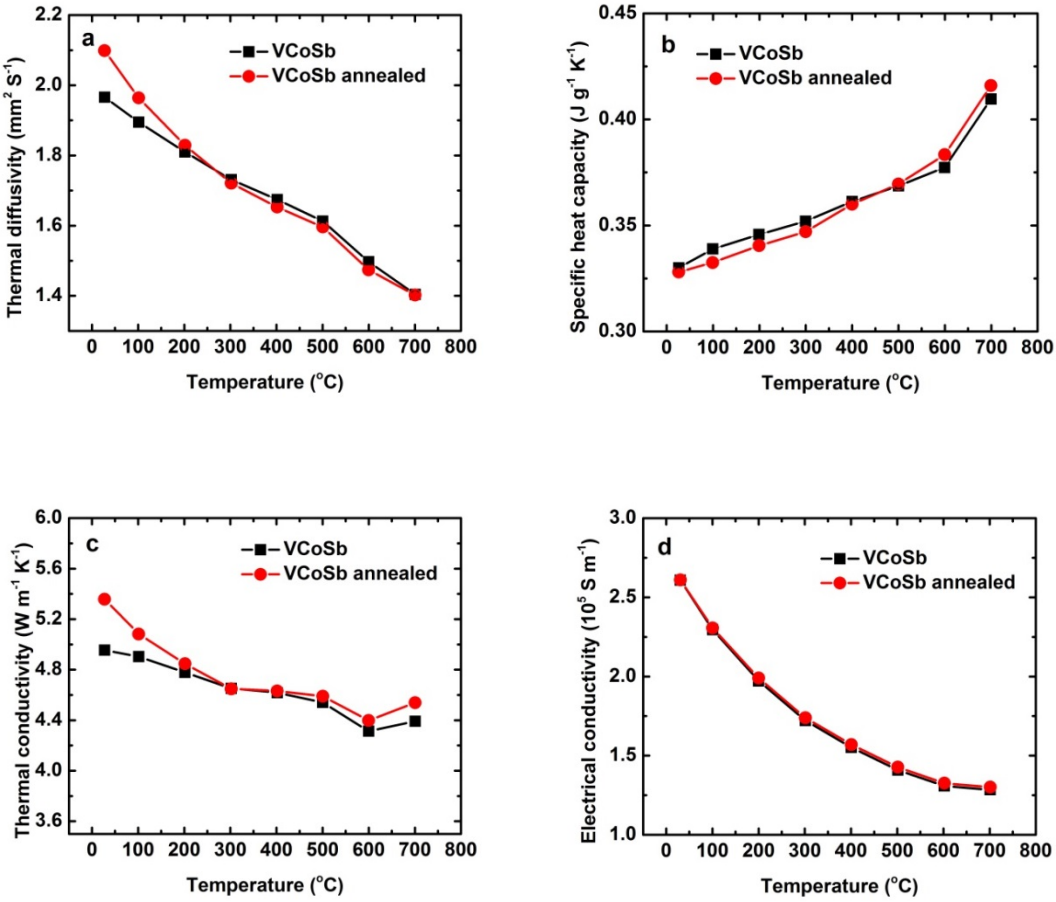

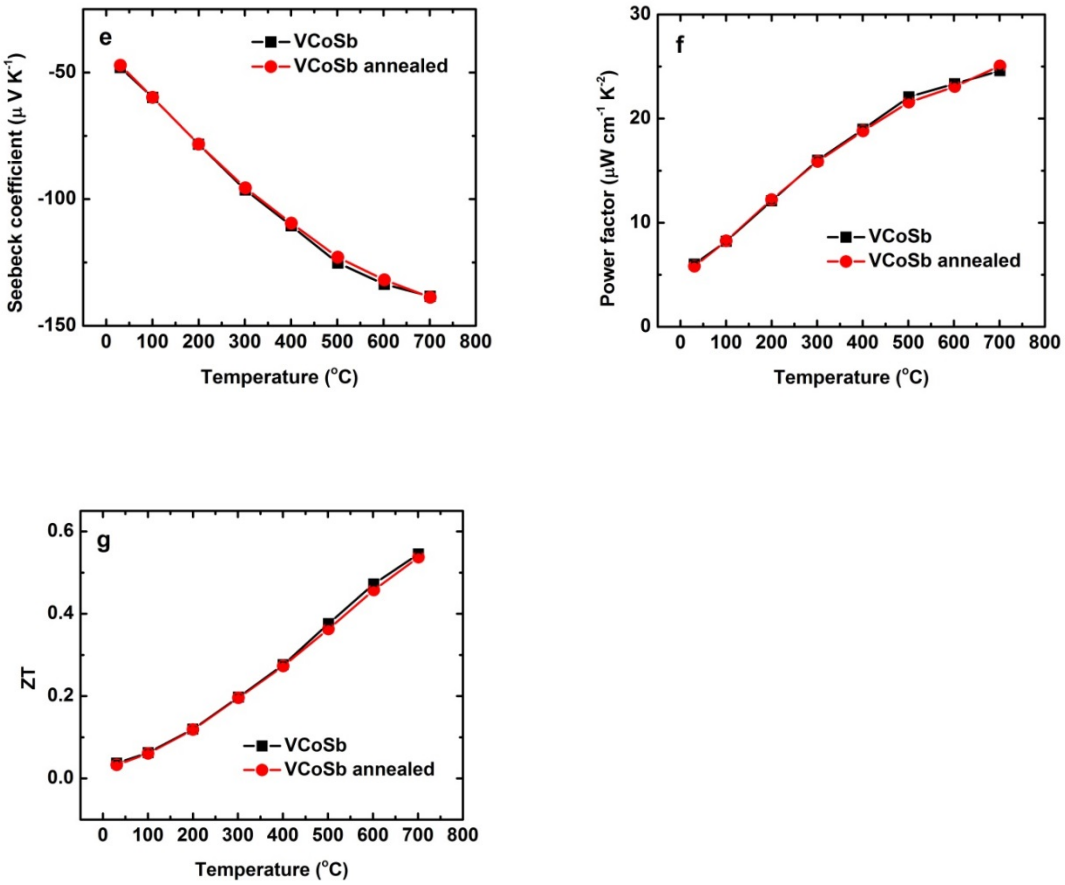

Figure 5.3.9 Temperature-dependent thermal diffusivity (a), specific heat capacity (b), thermal conductivity (c), electrical conductivity (d), Seebeck coefficient (e), power factor (f), and ZT (g) of VCoSb sample, and the VCoSb sample annealed at 700 °C for 24hours.

5.3.4 Doping in VCoSb

Since good thermoelectric materials usually have carrier concentrations in the range of 10^{19} cm^{-3} to 10^{20} cm^{-3} [6], doping to decrease the carrier concentration may further improve the thermoelectric properties for this VCoSb compound. Thus, we also did a series of different concentrations of Sn doping at the Sb site and Ti doping at the V site to reduce the carrier concentration.

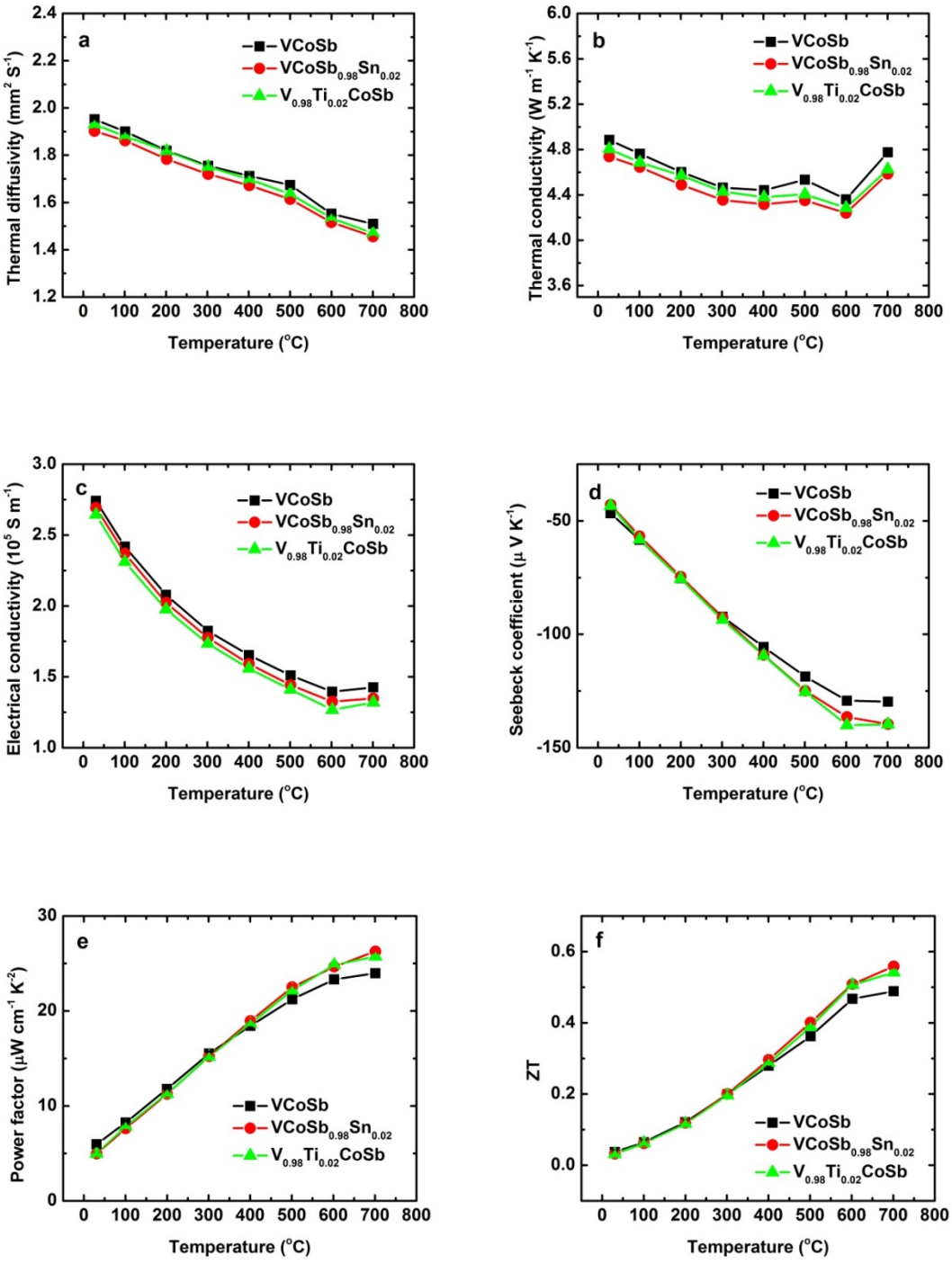

Figure 5.3.10 Temperature-dependent thermal diffusivity (a), thermal conductivity (b), electrical conductivity (c), Seebeck coefficient (d), power factor (e), and ZT (f) of VCoSb, $VCoSb_{0.98}Sn_{0.02}$, and $V_{0.98}Ti_{0.02}CoSb$.

The results of 2 at% Sn doping ($VCoSb_{0.98}Sn_{0.02}$) and 2 at% Ti doping ($V_{0.98}Ti_{0.02}CoSb$) are presented in Figure 5.3.10. It shows that the thermal and electrical conductivity can be suppressed slightly by Sn and Ti doping. The Seebeck coefficients are almost the same below 400 °C and only show some improvement at high temperatures for the doped samples. Higher power factor values are noticed after 400 °C. As a result, the ZT has some improvement at high temperatures and the peak value around 0.56 is achieved at 700 °C for both the doped samples.

5.4 Conclusions

In conclusion, half-Heusler compounds VCoSb with VEC of 19 are successfully synthesized by arc-melting, ball-milling, and hot-pressing. Despite the high carrier concentration due to the VEC of 19, the electrical conductivity is not very high since the mobility is low. Moreover, the Seebeck coefficient around -130 μV/K at 600 °C is abnormally high considering the very high carrier concentration. By the nanostructuring approach, the thermal conductivity can be reduced and the power factor can be improved simultaneously compared to the ingot. Lower hot-pressing temperature results in some porosity and increasing the ball-milling time from 5 hour to 9 hours does not change the thermoelectric properties. A peak power factor of 25 $\mu W\ cm^{-1}\ K^{-2}$ and ZT of about 0.5 are achieved at 700 °C for all the nanostructured samples. Finally, when VCoSb is doped with 2 at% Sn ($VCoSb_{0.98}Sn_{0.02}$) and 2 at% Ti ($V_{0.98}Ti_{0.02}CoSb$) respectively, the ZT value can be enhanced to 0.56 at 700 ^{o}C.

References

[1] J. Tobola, J. Pierre, S. Kaprzyk, R.V. Skolozdra, M.A. Kouacou. Journal of Physics: Condensed Matter 10 (1998) 1013.

[2] J. Toboła, J. Pierre. Journal of Alloys and Compounds 296 (2000) 243-252.

[3] J. Yang, H. Li, T. Wu, W. Zhang, L. Chen, J. Yang. Advanced Functional Materials 18 (2008) 2880-2888.

[4] L. Huang, R. He, S. Chen, H. Zhang, K. Dahal, H. Zhou, H. Wang, Q. Zhang, Z. Ren. Materials Research Bulletin 70 (2015) 773-778.

[5] K. Kaczmarska, J. Pierre, J. Beille, J. Tobola, R. Skolozdra, G. Melnik. Journal of Magnetism and Magnetic Materials 187 (1998) 210-220.

[6] G.J. Snyder, E.S. Toberer. Nature Materials 7 (2008) 105-114.

Chapter 6

Exploring the Thermoelectric Properties of Unconventional Half-Heuslers

6.1 Introduction

The history of Heulser compounds can be traced back to the year 1903 when Fritz Heusler discovered that an alloy with the composition Cu_2MnAl behaves like a ferromagnet, although none of its constituent elements is magnetic by itself [1]. Heusler compounds represent a large family of materials with composition AB_2X known as full-Heuslers and ABX called half-Heuslers. Figure 6.1.1 is the periodic table, in which the colored elements can form a huge number of Heusler compounds by different combinations according to the color scheme.

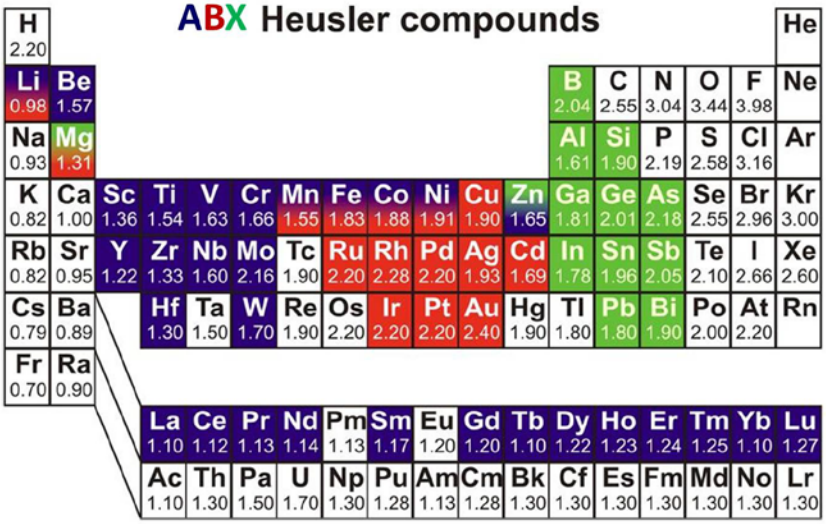

Figure 6.1.1 Periodic table. Heusler compounds can be formed by combination of the different elements according to the color scheme [1].

For thermoelectric applications, half-Heusler compounds with valence electron count of 18 are favorable because they are usually narrow bandgap semiconductors. Besides the intensively studied half-Heuslers MNiSn for n-type and MCoSb for p-type (M=Ti, Zr, and Hf), in fact there is still a large class of half-Heusler compounds which meet the criterion of VEC = 18 for semiconductors. However, only a few of them have been studied for thermoelectric properties, such as NbCoSn, YNiBi, HfPtSn, ErPdSb, NbIrSn, and so on [2-6]. Ono et al. reported that the 10 at% Sb doped NbCoSn had a power factor of 22 x 10^{-4} W m^{-1} K^{-2} at around 500 ^{o}C and the peak ZT value can reach 0.3 at 500 ^{o}C [6]. YNiBi was reported to have a peak ZT value of 0.12 [7]. Both of them have a much lower ZT than the conventional MNiSn based half-Heuslers. For other studied half-Heuslers such as HfPtSn, ErPdBi, and NbIrSn, their ZT values are not comparable to MNiSn or MCoSb either and they contain expensive and rare earth elements which are not practical in large scale applications.

Recently, the NbFeSb based half-Heuslers are found to be good p-type thermoelectric materials [8-11]. Giri et al. reported that the Ti and Sn doped $Nb_{0.6}Ti_{0.4}FeSb_{0.95}Sn_{0.05}$ was a p-type semiconductor, and its peak ZT value was around 1 at 700 ^{o}C which is comparable to the MCoSb based p-type half-Heuslers [9]. Fu et al. found that with heavier Hf dopant, $Nb_{1-x}Hf_xFeSb$ (x = 0.12 and 0.14) had a ZT value of 1.5 at 1200 K, which is the highest ZT value for p-type half-Heuslers up to now [11]. With better thermoelectric performance and lower cost, NbFeSb based p-type half-Heuslers have taken over the conventional MCoSb based ones to make thermoelectric devices.

Although MNiSn and MCoSb have long been the best n-type and p-type half-Heuslers for thermoelectric applications, there exist other half-Heuslers which may have better

thermoelectric performance, such as NbFeSb. Therefore, synthesizing and studying the thermoelectric properties of half-Heuslers with unconventional compositions is as important as optimizing the thermoelectric properties of the well-known ones. Thus in this chapter, we focus on exploring the thermoelectric properties of unconventional half-Heuslers. The thermoelectric properties of two half-Heusler compositions: VFeSb and YNiSb are studied and discussed in the following two sections.

6.2 Thermoelectric Properties of VFeSb

6.2.1 Introduction

NbFeSb based half-Heuslers have been found to be good p-type thermoelectric materials. Its similar composition VFeSb is in fact an intrinsic n-type semiconductor. Theoretical calculations show that VFeSb has an energy gap of around 0.45 eV and the gap arises between the L point at the top of the valence band and the X point at the bottom of the conduction band [12, 13]. Experimental studies found that the room temperature Seebeck coefficient of VFeSb is -110 $\mu V\ K^{-1}$, which demonstrates that it is n-type without any doping [13]. In this section, the VFeSb based half-Heuslers are synthesized and their thermoelectric properties are studied. To optimize the thermoelectric performance, cobalt doping at the Fe site is tried to increase the electrical conductivity and enhanced ZT value is obtained. To suppress the thermal conductivity, alloying Nb at the V is carried out too. Finally, a peak ZT value of 0.45 at 600 ^{o}C is achieved in the $V_{0.9}Nb_{0.1}Fe_{0.95}Co_{0.05}Sb$ sample.

6.2.2 Experimental Procedures

VFeSb, $VFe_{1-x}Co_xSb$ (x = 0.02, 0.05, and 0.1), and $V_{1-y}Nb_yFe_{0.95}Co_{0.05}Sb$ (y = 0.1, 0.2, and 0.3) samples were prepared by the nanostructuring approach of arc-melting, ball-milling, and hot-pressing. Firstly, the ingots of the samples were made by arc-melting vanadium pieces (99.7%, Alfa Aesar), iron granules (99.98%, Alfa Aesar), antimony rod (99.8%, Alfa Aesar), cobalt pieces (99.9+%, Alfa Aesar), and niobium foil (99.8%, Alfa Aesar) according to the stoichiometry. To ensure the homogeneity, the ingots were arc-melted under Ar protection at least three times and flipped over every time. Then the alloyed ingots were ball-milled for 5 hours. The bulk samples were prepared by hot pressing the nanopowders in a graphite die. After hot-press, the graphite die was taken out immediately to let it cool down slowly. The disks of 12.7 mm in diameter and around 2 mm in thickness were prepared for measurements.

The measurement errors were estimated to be 3% for electrical conductivity, 5% for Seebeck coefficient, and 3% for thermal diffusivity, which results in an uncertainty of 11% for ZT. For better readability, all the figures are plotted without error bars.

6.2.3 N-type Half-Heusler VFeSb

The XRD pattern of VFeSb sample is shown in Figure 6.2.1. All the indexed peaks correspond to the cubic half-Heusler phase. Small amount of impurity phases are found and peaks of impurity are marked by star in the pattern.

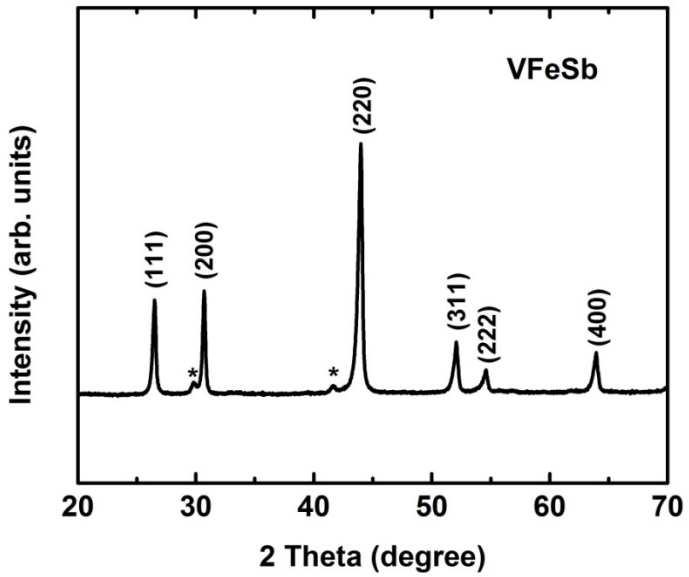

Figure 6.2.1 XRD pattern of VFeSb.

The temperature-dependent thermoelectric properties of VFeSb are measured and shown in Figure 6.2.2. The thermal conductivity in Figure 6.2.2 (a) is calculated by multiplying the thermal diffusivity, the density, and the specific heat capacity of the sample. The thermal diffusivity is measured by the lasherflash. The Cp is calculated based on the Dulong–Petit law, that is Cp = 3R/M, where R is the gas constant and M is the molar mass. The calculated Cp is 0.327 J g^{-1} K^{-1} for VFeSb. The density of the sample is 7.562 g cm^{-3}, measured by Archimede's method. The relative density of the sample is 98.5% (experimental value vs theoretical density of 7.675 g cm^{-3}) meaning that the sample has high compaction.

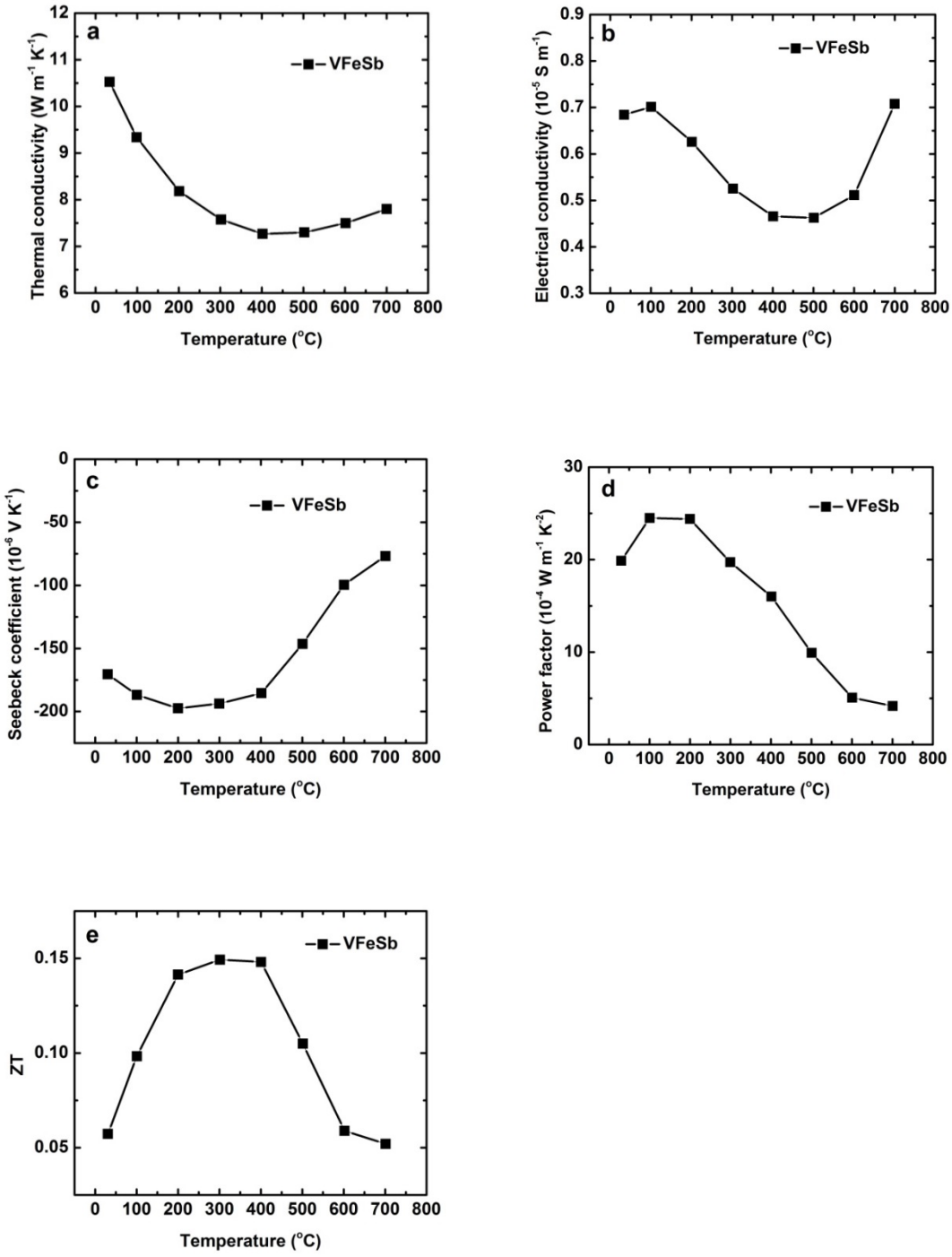

Figure 6.2.2 Temperature-dependent thermal conductivity (a), electrical conductivity (b), Seebeck coefficient (c), power factor (d), and ZT (e) of VFeSb.

The thermal conductivity of VFeSb is very high with room temperature thermal conductivity of 10.5 W m^{-1} K^{-1}. The thermal conductivity decreases with temperature at first and then increases after 400 ^{o}C due to the bipolar effect. The electrical conductivity of VFeSb is low only around 0.7 x 10^{-5} S m^{-1} at room temperature, so doping to enhance the electrical conductivity is needed. As the temperature increases, the electrical conductivity decreases at first, and start to increase at high temperatures because of thermal excitation of intrinsic charge carriers.

The Seebeck coefficient (Figure 6.2.2 (c)) of the undoped VFeSb is negative, so it is an n-type semiconductor. The Seebeck coefficient of VFeSb at room temperature is -170 μV K^{-1}, and the high Seebeck coefficient means that VFeSb may be promising thermoelectric material. The Seebeck coefficient also increases with temperature and then decreases after 200 ^{o}C due to the bipolar effect. The bandgap of VFeSb is estimated to be 0.19 eV by the Goldsmid-Sharp bandgap formula $E_g = 2eS_{max}T_{max}$. The bandgap of VFeSb is small so the bipolar effect can easily occur in this compound. The power factor is shown in Figure 6.2.2 (d). The highest power factor of 25 x 10^{-4} W m^{-1} K^{-2} is obtained at 100 ^{o}C and 200 ^{o}C. The ZT values (Figure 6.2.2 (e)) of the undoped VFeSb is low. The peak ZT is only around 0.15 at 300 ^{o}C and 400 ^{o}C.

6.2.4 Co doping in VFeSb

Since the Seebeck coefficient of VFeSb is high and its electrical conductivity is low, doping to increase the carrier concentration may enhance its thermoelectric properties. Thus, cobalt doping at the Fe site is tried to optimize the electrical properties. Samples doped with 2 at%, 5 at%, and 10 at% Co are prepared respectively.

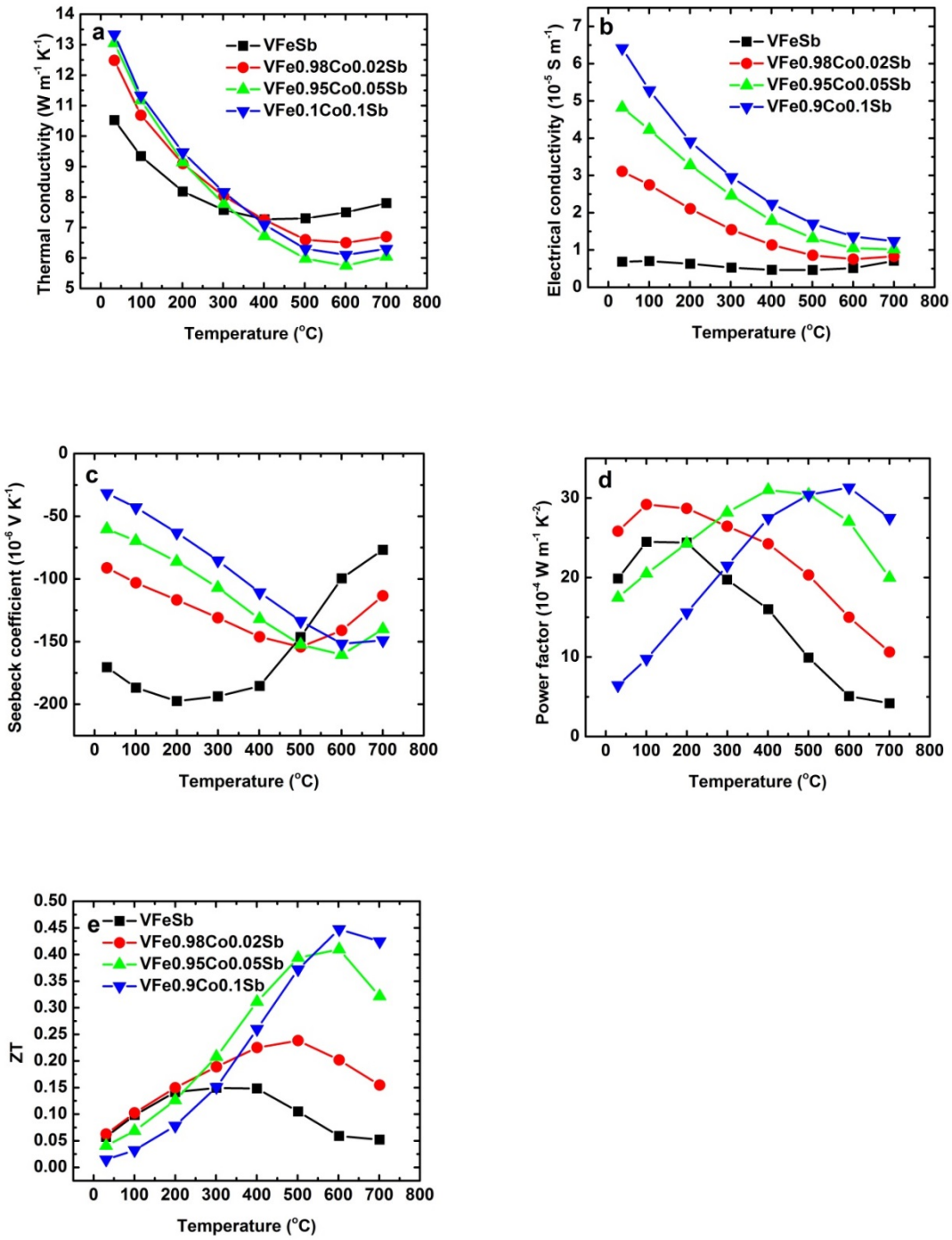

Figure 6.2.3 Temperature-dependent thermal conductivity (a), electrical conductivity (b), Seebeck coefficient (c), power factor (d), and ZT (e) of $VFe_{1-x}Co_xSb$ (x = 0.02, 0.05, and 0.1)

Figure 6.2.3 (a) presents the temperature-dependent thermal conductivities of the samples. At room temperature, all the samples doped with Co possess higher thermal conductivity than the undoped sample, and the higher the doping level the larger the thermal conductivity is. However, when the temperature is higher than 400 ^{o}C, the thermal conductivity of the samples with Co is lower than the undoped one, which is due to the suppression of bipolar effect. In Figure 6.2.3 (b), the electrical conductivity is increased by Co doping because of the increased carrier concentration. When the Co ratio increases, the electrical conductivity keeps increasing at room temperature. For the doped samples, the electrical conductivity decreases with temperature showing the typical behavior of degenerate semiconductors. Figure 6.2.3 (c) shows the measured Seebeck coefficient for all the samples. At room temperature, the Seebeck coefficient drops quite a lot after Co doping because the carrier concentration is increased. After 500 ^{o}C, all the samples with Co possess higher Seebeck coefficient than the undoped sample because the bipolar effect is suppressed. The bandgap of the samples are calculated from the Goldsmid-Sharp bandgap formula. The bandgaps for samples with 0 at%, 2 at%, 5 at%, and 10 at% Co are 0.19 eV, 0.24 eV, 0.28 eV, and 0.27 eV respectively. So the bandgap is enlarged by Co doping. Therefore the suppression of bipolar effects can be ascribed to the enlarged bandgap and the enhanced extrinsic carrier concentration.

As shown in Figure 6.2.3 (d), compared to the VFeSb sample, the sample doped with 2 at% Co has higher power factor values over the whole temperature range and the peak power factor of 30 x 10^{-4} W m^{-1} K^{-2} is achieved at 100 ^{o}C. As the Co doping level increases, the peak of power factor moves to higher temperatures. With 5 at% and 10 at% Co doping, the highest power factor above 30 x 10^{-4} W m^{-1} K^{-2} is attained at 400 ^{o}C and 600 ^{o}C,

respectively. Due to the suppressed thermal conductivity and the enhanced power factor at high temperatures, all the samples doped with Co show improved ZT values at above 300 ^{o}C as shown in Figure 6.2.3 (e). The maximum ZT value of 0.45 is achieved at 600 ^{o}C in the sample doped with 10 at% Co, which is about 200% enhancement compared to the sample without Co.

6.2.5 Alloying Nb in VFeSb

Since the thermal conductivity of VFeSb is high with a room temperature thermal conductivity of 10.5 W m^{-1} K^{-1}, reducing the thermal conductivity of VFeSb is important in pursuing higher ZT. As alloying effects have been proven to be an effective approach to suppress thermal conductivity, Nb substitution of V is carried out trying to reduce the thermal conductivity. $V_{1-y}Nb_yFe_{0.95}Co_{0.05}Sb$ (y = 0.1, 0.2, and 0.3) samples are prepared. The thermoelectric properties of them are measured and presented in Figure 6.2.4. As shown in Figure 6.2.4 (a), the thermal conductivity is decreased in the whole temperature range with Nb substitution. As Nb concentration increases, the thermal conductivity keeps decreasing. The room temperature thermal conductivity is reduced to 7.2 W m^{-1} K^{-1} with 30% Nb, which is about 30% reduction compared to the sample without alloying.

The electrical conductivity is shown in Figure 6.2.4 (b). When Nb substitutes V in $VFe_{0.95}Co_{0.05}Sb$, the electrical conductivity is decreased. The reason for the decrease of electrical conductivity may be that there are more alloying scatterings for charge carriers as well, so the carrier mobility is reduced.

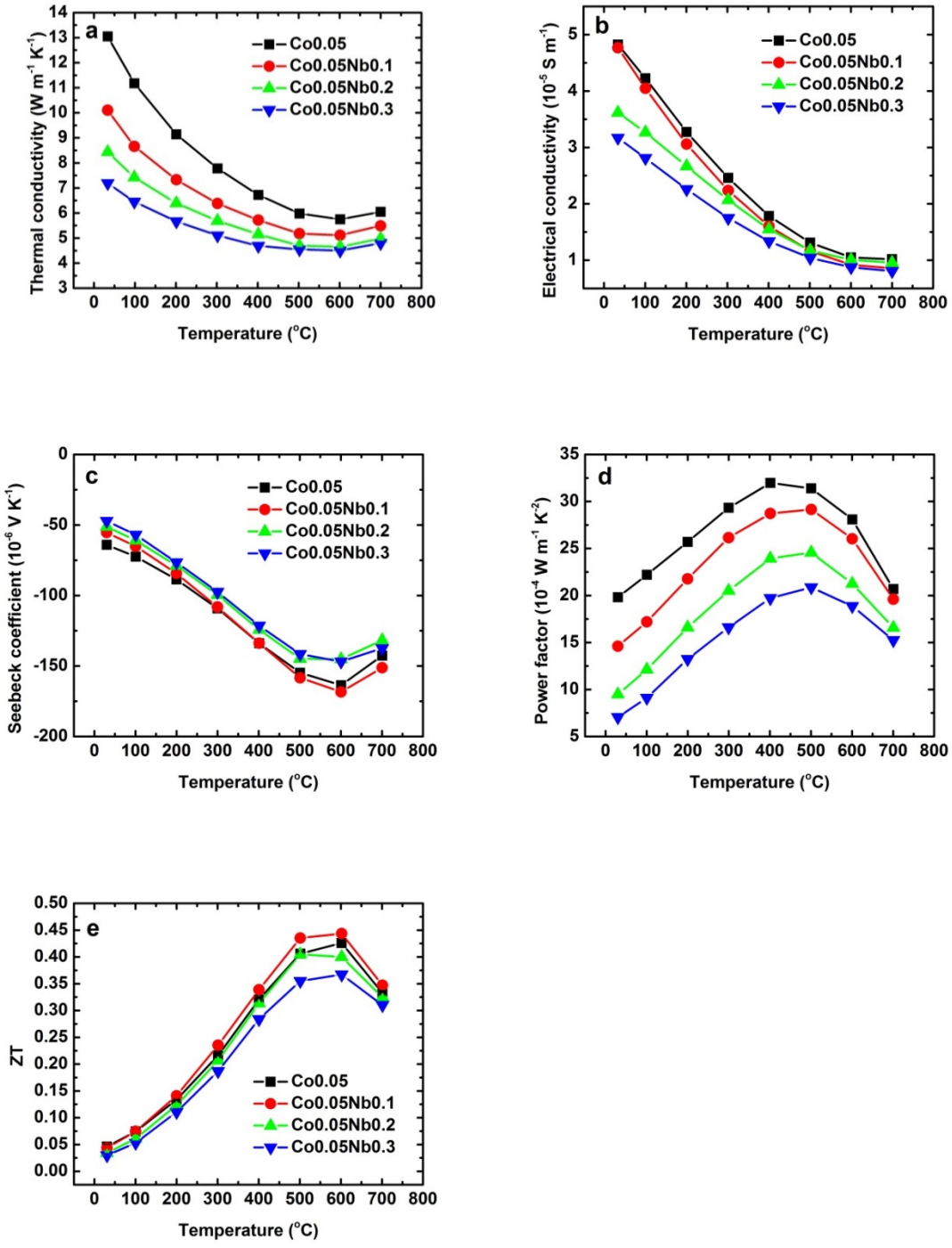

Figure 6.2.4 Temperature-dependent thermal conductivity (a), electrical conductivity (b), Seebeck coefficient (c), power factor (d), and ZT (e) of $V_{1-y}Nb_yFe_{0.95}Co_{0.05}Sb$ (y = 0.1, 0.2, and 0.3).

The Seebeck coefficient is given in Figure 6.2.4 (c). The Seebeck coefficient is also decreased when Nb substitutes V. This is surprising, because usually when the electrical conductivity decreases, the Seebeck coefficient will increase. As NbFeSb is found to be a good p-type thermoelectric material, when V is substituted by Nb in this n-type VFeSb half-Heusler, the Seebeck coefficient may be deteriorated by the p-type characteristic of NbFeSb. Thus the Seebeck coefficient is decreased with Nb substitution. Because both the electrical conductivity and Seebeck coefficient are reduced when alloying Nb at the V site, the power factor is decreased. As shown in Figure 6.2.4 (d) with higher Nb concentration, the power factor continues decreasing at all temperatures. The peak power factor drops from 32 x 10^{-4} W m^{-1} K^{-2} in sample $VFe_{0.95}Co_{0.05}Sb$ to 21 x 10^{-4} W m^{-1} K^{-2} in sample $V_{0.7}Nb_{0.3}Fe_{0.95}Co_{0.05}Sb$. As a result, although the thermal conductivity is suppressed by alloying Nb with V, the ZT is not improved due to the decrease of power factor. As given in Figure 6.2.4 (e), only the sample with 10% Nb shows slight improvement of ZT. The other two samples alloyed with 20% and 30% have even lower ZT values than the unalloyed one.

6.2.6 Conclusions

The half-Heusler compound VFeSb is synthesized by the nanostructuring approach of arc-melting, ball-milling and hot-pressing. The Seebeck coefficient at room temperature of VFeSb is -170 μV K^{-1} demonstrating that it is an n-type semiconductor. The high thermal conductivity and low electrical conductivity of VFeSb limit the ZT only to 0.15. To enhance the electrical conductivity, cobalt doping at the Fe site is carried out. Higher power factor of 30 x 10^{-4} W m^{-1} K^{-2} is obtained with Co doping compared to the undoped

VFeSb of which the peak power factor is 25 x 10^{-4} W m^{-1} K^{-2}. With the increase of Co doping concentration, the peak of the power factor moves to higher temperatures due to suppressed bipolar effect. As a result, the highest ZT value of 0.45 is achieved at 600 ^{o}C in the sample doped with 10 at% Co. On the other hand, to reduce the thermal conductivity, V is substituted by Nb to provide more alloying scatterings for phonons. Although the thermal conductivity is decreased by alloying Nb at the V site, the electrical properties become worse at the same time which may be owing to the p-type properties of NbFeSb. Thus the ZT is not further improved with Nb substitution.

6.3 Thermoelectric Properties of YNiSb

6.3.1 Introduction

The compound YNiSb crystallizes in the half-Heusler structure with Y, Ni, and Sb atoms occupying (0, 0, 0), (1/4, 1/4, 1/4), and (1/2, 1/2, 1/2) positions, respectively. Larson et al. calculated the band structure of YNiSb and found that it was a semiconductor with a narrow bandgap of 0.28 eV [14]. In spite of the basic differences in the nature of bonding, the energy band structure in the neighborhood of the Fermi energy is remarkably similar in ZrNiSn and YNiSb. Later Oestreich et al. synthesized this YNiSb compound by arc-melting stoichiometric mixtures of the elements and annealed for 10-30 days at 1100 K to improve their homogeneity [15]. The Seebeck coefficient at room temperature was found to be +31.7 μV K^{-1}, so it is p-type. They also obtained the bandgap value of 0.18 eV for YNiSb from the resistivity measurements using the equation $\rho \approx \exp(E_g/2k_BT)$. In this section, the half-Heusler compounds YNiSb are synthesized and their thermoelectric properties are studied. The Seebeck coefficient of YNiSb is 85 μV K^{-1} at room

temperature and increased to 120 μV K^{-1} at 200 ^{o}C. A peak power factor of 9.3 x 10^{-4} W m^{-1} K^{-2} and a maximum ZT of 0.13 are achieved at 500 ^{o}C for YNiSb. To enhance the electrical conductivity, p-type dopants Mg, Co, and Sn is tried at the Y, Ni, and Sb site respectively. The electrical conductivity can be increased by doping. However, the ZT values do not have too much improvement.

6.3.2 Experimental Procedures

Since Sb has a high vapor pressure and evaporates greatly during arc-melting, YNi ingot was first prepared by arc-melting Y pieces (99.9% Alfa Aesar) and Ni slug (99.98%, Alfa Aesar) with the atomic ratio of 1:1. Then the YNi ingot was mixed with Sb rod (99.8%, Alfa Aesar) in nominal YNiSb ratio through high-energy ball-milling. The YNiSb compound was formed by the mechanical alloying. The bulk samples were prepared by hot pressing the nanopowders in a graphite die. After hot-press, the graphite die was taken out immediately to let it cool down slowly. The disks of 12.7 mm in diameter and around 2 mm in thickness were prepared for measurements. The other samples with dopants $YNiSb_{0.98}Sn_{0.02}$, $Y_{0.99}Mg_{0.01}NiSb$, and $YNi_{0.95}Co_{0.05}Sb$ were prepared through the same way.

The measurement errors were estimated to be 3% for electrical conductivity, 5% for Seebeck coefficient, and 3% for thermal diffusivity, which results in an uncertainty of 11% for ZT. For better readability, all the figures are plotted without error bars.

6.3.3 P-type Half-Heusler YNiSb

The XRD pattern of YNiSb sample is shown in Figure 6.3.1. All the indexed peaks correspond to the cubic half-Heusler phase. A small amount of impurity phases are found and peaks of impurity are marked by star in the pattern.

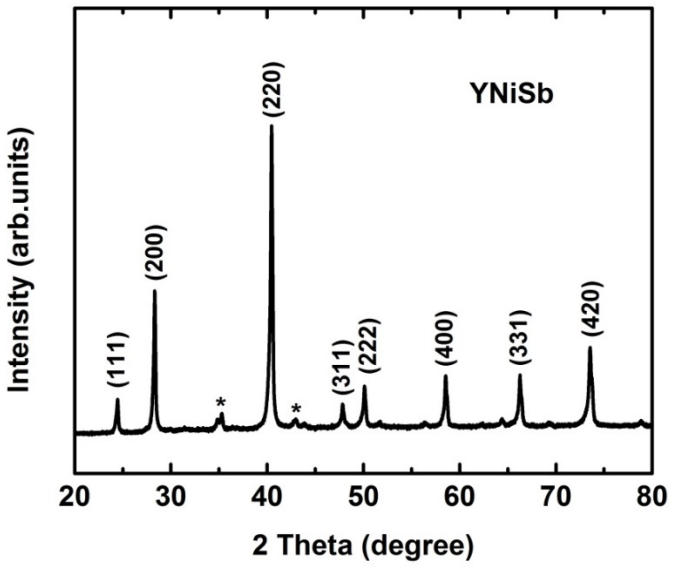

Figure 6.3.1 XRD pattern of YNiSb.

The thermoelectric properties of YNiSb sample are summarized in Figure 6.3.2. The density of the sample is 7.016 g cm^{-3}, measured by Archimede's method. The relative density is 98.4% calculated via dividing the measurement value by the theoretical density of 7.130 g cm^{-3}. The high relative density means that the sample has high compaction. The specific heat capacity of YNiSb is calculated through Cp = 3R/M, and the calculated Cp is 0.278 J g^{-1} K^{-1}. The thermal conductivity is then calculated by multiplying the thermal diffusivity measured by lasherfalsh, the density, and Cp. As shown in Figure

6.3.2 (a), at room temperature, the thermal conductivity value of 4.3 W m^{-1} K^{-1} for YNiSb is not too high. However, after 200 ^{o}C the thermal conductivity increases dramatically. A high thermal conductivity of 7.0 W m^{-1} K^{-1} is reached at 700 ^{o}C. The increase of the thermal conductivity is due to the thermal excitation of intrinsic charge carriers. The temperature-dependent electrical conductivity is shown in Figure 6.3.2 (b). The electrical conductivity increases when temperature rises, showing the typical characteristic of semiconductor. The electrical conductivity of the YNiSb sample without any doping is low, only 0.24 x 10^{-5} S m^{-1} at room temperature.

The Seebeck coefficient of YNiSb is presented in Figure 6.3.2 (c). The room temperature Seebeck coefficient of YNiSb is 85 μV K^{-1}, higher than the reported value of 31.7 μV K^{-1} in the literature [15]. As temperature increases, the Seebeck coefficient increases at first with a peak value of 120 μV K^{-1} at 200 ^{o}C and 300 ^{o}C, and then drops due to the bipolar effect. The bandgap of YNiSb is estimated to be 0.14 eV by the formula $E_g = 2eS_{max}T_{max}$. This bandgap value is close to the value of 0.18 eV reported by Oestreich et al [15]. Since the bandgap of YNiSb is so small, the bipolar effect is severe in this compound. Figure 6.3.2 (d) shows the power factor. The power factor increases with temperature and then begins to decrease after 500 ^{o}C. As the electrical conductivity of the sample is low and the Seebeck coefficient drops quite a lot at high temperatures, a peak power factor of only 9.3 x 10^{-4} W m^{-1} K^{-2} is obtained at 500 ^{o}C. The ZT values of YNiSb are given in Figure 6.3.2 (e). A maximum ZT of 0.13 is achieved at 500 ^{o}C for YNiSb.

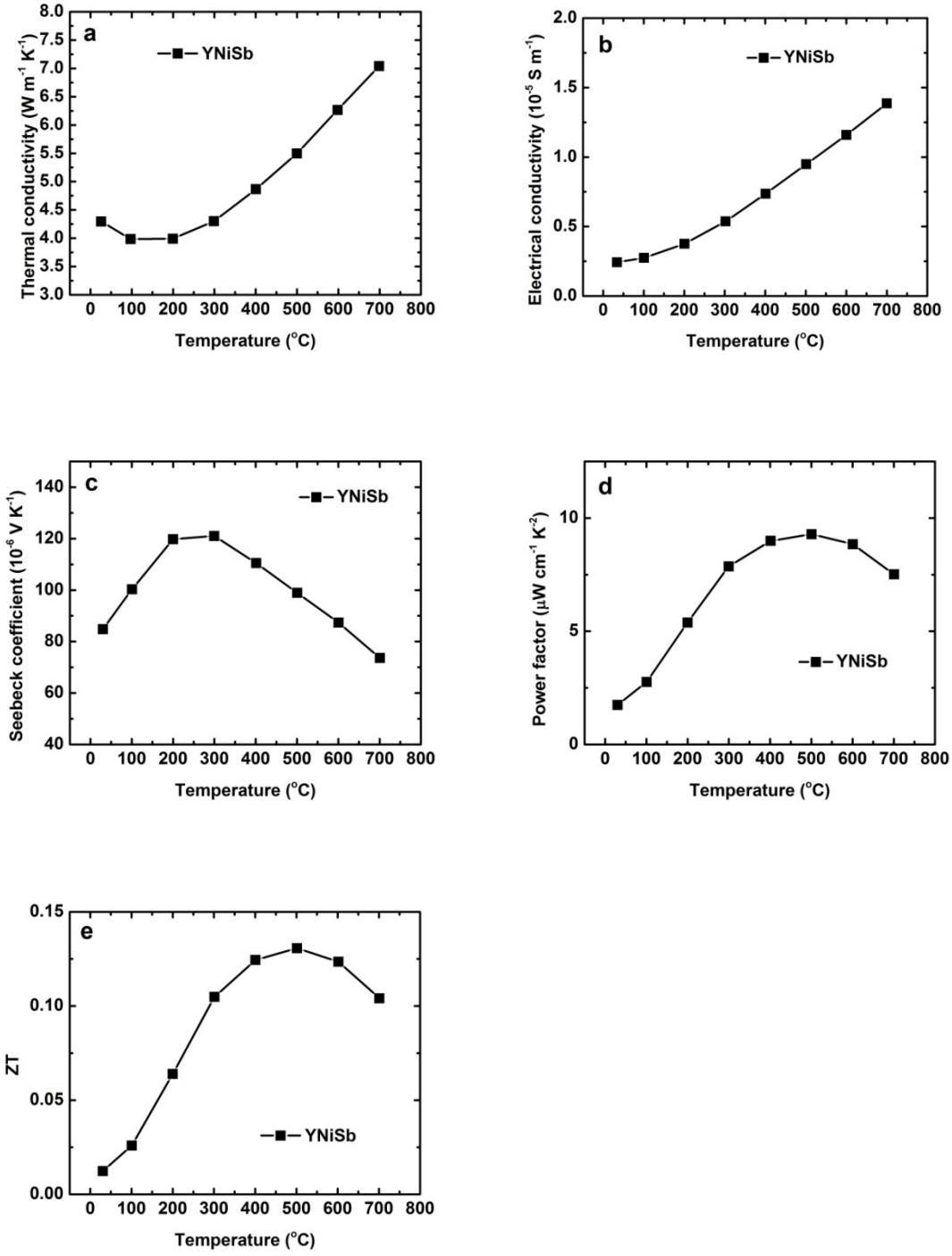

Figure 6.3.2 Temperature-dependent thermal conductivity (a), electrical conductivity (b), Seebeck coefficient (c), power factor (d), and ZT (e) of YNiSb.

6.3.4 Doping in YNiSb

As discussed above, the electrical conductivity of YNiSb is 0.24 x 10^{-5} S m^{-1} at room temperature which is too low for a good thermoelectric material, so doping to enhance the carrier concentration is needed. 1 at% Mg, 5 at% Co, and 2 at% Sn doping at the Y, Ni, and Sb site in YNiSb is carried out respectively. The thermoelectric properties of $YNiSb_{0.98}Sn_{0.02}$, $Y_{0.99}Mg_{0.01}NiSb$, and $YNi_{0.95}Co_{0.05}Sb$ are shown and compared to the undoped YNiSb sample in Figure 6.3.3. As shown in Figure 6.3.3 (a), with 2 at% Sn doping, the thermal conductivity doesn't change too much. For the 1 at% Mg doped sample, below 400 ^{o}C the thermal conductivity is increased in comparison with the undoped sample due to the increased electronic thermal conductivity. Above 400 ^{o}C, the thermal conductivity of $Y_{0.99}Mg_{0.01}NiSb$ is lower than YNiSb probably because the higher extrinsic carrier concentration suppresses the bipolar effect. The thermal conductivity of the sample doped with 5 at% Co is increased at all temperatures compared to the undoped one.

The electrical conductivities of all the samples are presented in Figure 6.3.3 (b). With 2 at% Sn doping, the electrical conductivity only shows a small enhancement, so for Sn doping at the Sb site, the doping concentration of 2 at% is still too low. Higher Sn doping level should be tried to further enhance the electrical conductivity. For the sample doped with 1 at% Mg at the Y site, the electrical conductivity is increased significantly. The room temperature electrical conductivity is increased from 0.24 x 10^{-5} S m^{-1} to 2.12 x 10^{-5} S m^{-1}. The electrical conductivity of $Y_{0.99}Mg_{0.01}NiSb$ decreases with temperature showing the typical behavior of degenerate semiconductors. With only 1 at% Mg doping, the

electrical conductivity exhibits such a large enhancement, which means that Mg is an effective p-type donor for YNiSb. When YNiSb is doped with 5 at% Co at the Ni site, the electrical conductivity is also increased but not as high as the Mg doped one.

For the Seebeck coefficient (Figure 6.3.3 (c)), the sample doped with 2 at% Sn has increased Seebeck coefficient compared to the undoped sample below 300 ^{o}C. It is noteworthy that the electrical conductivity and the Seebeck coefficient are enhanced simultaneously with 2 at% Sn doping. Perhaps by Sn doping the band structure is modified and resonant states are introduced near the fermi level, as the circumstance found in V-doped ZrNiSb [16]. For the $Y_{0.99}Mg_{0.01}NiSb$ sample, the Seebeck coefficient is decreased a lot due to the increase of carrier concentration. The peak of the Seebeck coefficient for this sample moves to higher temperatures due to the suppression of bipolar effect. For the sample with 5 at% Co doping, the Seebeck coefficient is also decreased compared to the undoped sample.

The power factors of all the samples are shown in Figure 6.3.3 (d). The sample doped with 2 at% Sn has enhanced power factor below 500 ^{o}C owing to the simultaneously enhanced electrical conductivity and Seebeck coefficient. A maximum power factor of 10 x 10^{-4} W m^{-1} K^{-2} is achieved at 400 ^{o}C. For the sample doped with 1 at% Mg, although the electrical conductivity is increased quite a lot, however the Seebeck coefficient drops at the same time, so only small improvement of power factor is noticed below 500 ^{o}C compared to the undoped sample. For the 5 at% Co doped sample, the power factor is decreased at all temperatures in comparison to the undoped one, because the decrease of Seebeck coefficient is more than the increase of electrical conductivity. Thus Co may be not a good dopant for the YNiSb compound.

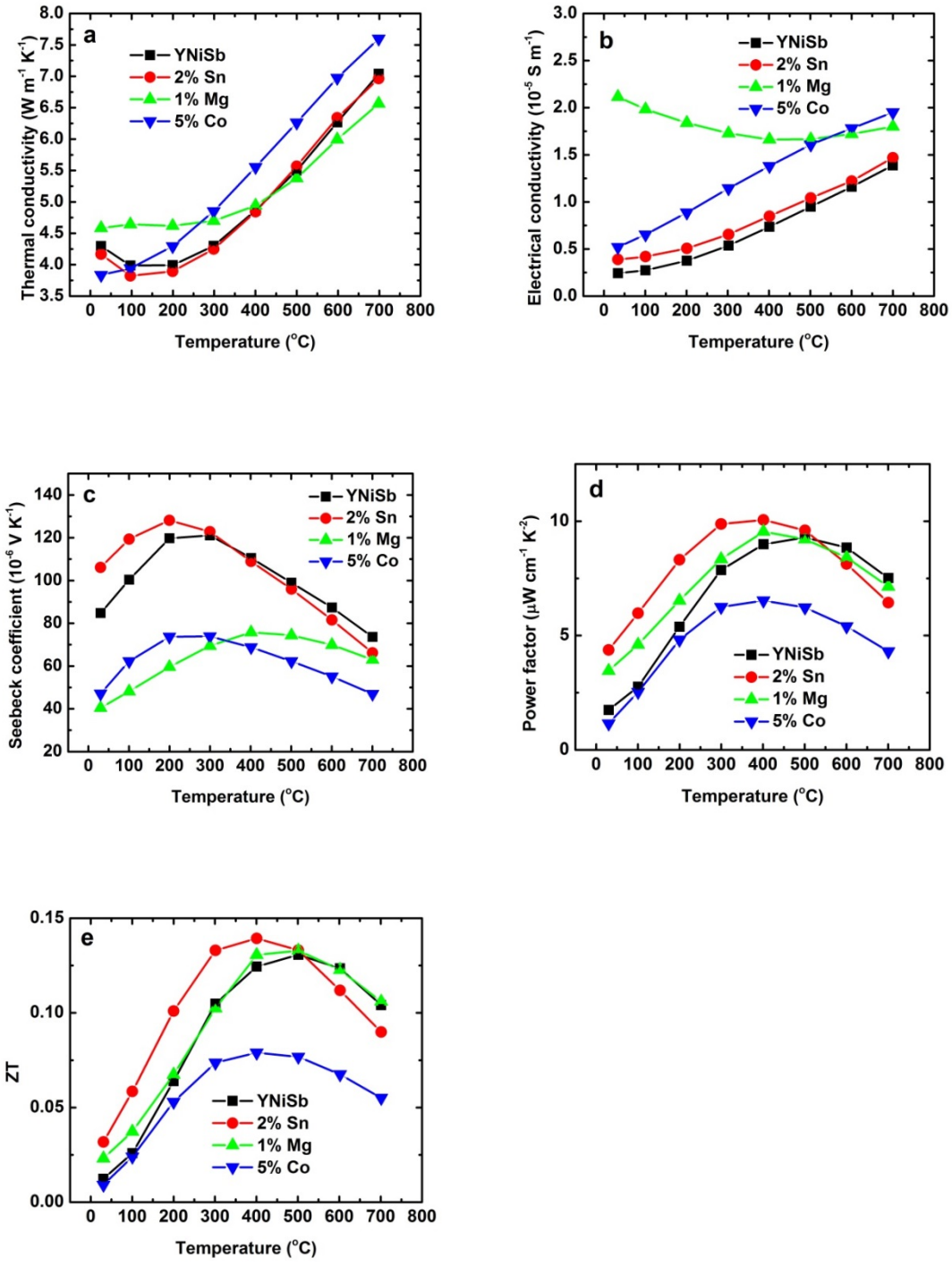

Figure 6.3.3 Temperature-dependent thermal conductivity (a), electrical conductivity (b), Seebeck coefficient (c), power factor (d), and ZT (e) of YNiSb, $YNiSb_{0.98}Sn_{0.02}$, $Y_{0.99}Mg_{0.01}NiSb$, and $YNi_{0.95}Co_{0.05}Sb$.

The ZT values are calculated and shown in Figure 6.3.3 (e). For the 2 at% Sn doped sample, below 500 ^{o}C the ZT is enhanced compared to the undoped one. A peak ZT value around 0.14 for the $YNiSb_{0.98}Sn_{0.02}$ sample is achieved at 400 ^{o}C, slightly higher than maximum ZT value of the undoped YNiSb sample. The ZT values of the 2 at% Mg doped sample do not have too much difference with the undoped sample. However, with 5 at% Co doping, the ZT values are decreased in the whole temperature range, which means Co doping cannot improve the thermoelectric properties of YNiSb. Future studies with higher Sn doping levels to further increase the electrical conductivity may be available for the improvement of ZT. For the Mg doping, since Mg is a strong p-type donor here, lower doping concentration than 1 at% may also be tried to optimize the electrical properties.

6.3.5 Conclusions

To avoid the evaporation of Sb during arc-melting, the YNiSb sample is prepared by arc-melting to form the YNi ingot first, then ball-milling the YNi ingot and Sb together in nominal YNiSb ratio, and finally hot-pressing to obtain the bulk sample. With a Seebeck coefficient of 85 $\mu V\ K^{-1}$ at room temperature, YNiSb is found to be a p-type semiconductor. The electrical conductivity of YNiSb is quite low only 0.24×10^{-5} S m^{-1} at room temperature, so both the power factor and ZT is not good. A maximum ZT of only 0.13 is attained at 500 ^{o}C for YNiSb. To enhance the electrical conductivity, 1 at% Mg, 5 at% Co, and 2 at% Sn doping at the Y, Ni, and Sb site in YNiSb is carried out respectively. For the $YNi_{0.95}Co_{0.05}Sb$ sample, although the electrical conductivity is increased, the Seebeck coefficient drops more. Both the power factor and ZT is decreased,

so Co is not a good dopant for YNiSb. With only 1 at% Mg doping at the Y site, the electrical conductivity at room temperature is increased to 2.12 x 10^{-5} S m^{-1}, which means that Mg is a strong p-type dopant for YNiSb. Small improvement of power factor is noticed but the ZT values don't change for $Y_{0.99}Mg_{0.01}NiSb$. Lower Mg doping concentration could be tried to optimize the electrical properties. Finally for the $YNiSb_{0.98}Sn_{0.02}$ sample, the power factor is enhanced below 500 ^{o}C due to the simultaneously enhanced electrical conductivity and Seebeck coefficient. A peak ZT value around 0.14 is achieved at 400 ^{o}C. Since the electrical conductivity of the Sn doped sample is still not high enough, higher Sn doping concentrations can be tried to optimize the thermoelectric properties of YNiSb.

References

[1] T. Graf, C. Felser, S.S. Parkin. Progress in Solid State Chemistry 39 (2011) 1-50.

[2] H. Hohl, A.P. Ramirez, C. Goldmann, G. Ernst, W. Bernd, E. Bucher. Journal of Physics: Condensed Matter 10 (1998) 7843.

[3] K. Mastronardi, D. Young, C.-C. Wang, P. Khalifah, R. Cava, A. Ramirez. Applied physics letters 74 (1999) 1415-1417.

[4] T. Sekimoto, K. Kurosaki, H. Muta, S. Yamanaka. Journal of Applied Physics 99 (2006) 103701.

[5] Y. Kimura, A. Zama. Applied Physics Letters 89 (2006) 2110.

[6] Y. Ono, S. Inayama, H. Adachi, T. Kajitani. Japanese Journal of Applied Physics 45 (2006) 8740.

[7] S. Li, H. Zhao, D. Li, S. Jin, L. Gu. Journal of Applied Physics 117 (2015) 205101.

[8] C. Fu, T. Zhu, Y. Pei, H. Xie, H. Wang, G.J. Snyder, Y. Liu, Y. Liu, X. Zhao. Advanced Energy Materials 4 (2014) 1400600.

[9] G. Joshi, R. He, M. Engber, G. Samsonidze, T. Pantha, E. Dahal, K. Dahal, J. Yang, Y. Lan, B. Kozinsky. Energy & Environmental Science 7 (2014) 4070-4076.

[10] C. Fu, T. Zhu, Y. Liu, H. Xie, X. Zhao. Energy & Environmental Science 8 (2015) 216-220.

[11] C. Fu, S. Bai, Y. Liu, Y. Tang, L. Chen, X. Zhao, T. Zhu. Nature Communications 6 (2015).

[12] L. Jodin, J. Tobola, P. Pecheur, H. Scherrer. Thermoelectrics, 2001. Proceedings ICT 2001. 20th International Conference on: IEEE, 2001. p.240-246.

[13] L. Jodin, J. Tobola, P. Pecheur, H. Scherrer, S. Kaprzyk. Physical Review B 70 (2004) 184207.

[14] P. Larson, S. Mahanti, S. Sportouch, M. Kanatzidis. Physical Review B 59 (1999) 15660.

[15] J. Oestreich, U. Probst, F. Richardt, E. Bucher. Journal of Physics: Condensed Matter 15 (2003) 635.

[16] J. Simonson, D. Wu, W. Xie, T.M. Tritt, S. Poon. Physical Review B 83 (2011) 235211.

Chapter 7

Summary

This dissertation is focused on the experimental studies of the thermoelectric properties for n-type half-Heuslers. It covers two aspects: (1) improving the thermoelectric properties of the nanostructured n-type half-Heusler $Hf_{0.25}Zr_{0.75}NiSn$ (in chapter 3 and chapter 4); (2) exploring the thermoelectric properties of other unconventional half-Heulser compositions (in chapter 5 and chapter 6). All the half-Heusler samples are successfully synthesized by the nanostructuring approach of arc-melting, ball-milling, and hot-pressing.

To improve the electrical properties of $Hf_{0.25}Zr_{0.75}NiSn$, Nb doping at the Hf/Zr site is carried out. With Nb doping, the carrier concentration is increased as well as the electrical conductivity indicating that Nb is an effective electron donor in this n-type half-Heusler. With optimized carrier concentration, the highest power factor of ~47 $\mu W\ cm^{-1}\ K^{-2}$ and peak ZT of ~0.9 are achieved with Nb doping from 1.8 at% to 2.2 at% at 700 ^{o}C. The calculated maximum output power density around 22 $W\ cm^{-2}$ and highest leg efficiency around 12% can be obtained in Nb-doped samples with a leg length of 2 mm, a cold side temperature of 50 °C and a hot side temperature of 700 °C. Similarly, V and Ta doped samples are also synthesized and their thermoelectric properties are studied as well. The highest power factor of 50 x 10^{-4} $W\ m^{-1}\ K^{-2}$ and the maximum ZT value of 1.1 is attained at 600 ^{o}C in the Ta-doped $(Hf_{0.25}Zr_{0.75})_{0.995}Ta_{0.005}NiSn$ sample.

To reduce the thermal conductivity, further alloying Ti at the Zr site is tried. The thermoelectric properties of $Hf_{0.25}Zr_{0.75-x}Ti_xNiSn_{0.99}Sb_{0.01}$ (x = 0, 0.1, 0.2, 0.3) samples are studied. The results show that the thermal conductivity can be suppressed and more than 20% reduction in thermal conductivity at room temperature is achieved by alloying 30% Ti. However, the electrical conductivity as well as the power factor is decreased with Ti substitution, so the ZT value does not have obvious improvement. To have a better understanding of the effects of Ti substitution, three unalloyed samples $TiNiSn_{0.99}Sb_{0.01}$, $ZrNiSn_{0.99}Sb_{0.01}$, and $HfNiSn_{0.99}Sb_{0.01}$ are synthesized as well. It turns out that $TiNiSn_{0.99}Sb_{0.01}$ has poorer electrical properties than the other two compounds, because the narrower bandgap in $TiNiSn_{0.99}Sb_{0.01}$ leads to stronger bipolar effects. This may be the reason for the worse electrical properties when further alloying Ti in $Hf_{0.25}Zr_{0.75}NiSn_{0.99}Sb_{0.01}$.

Another approach to enhance the thermoelectric properties of a material is to incorporate nanoinclusions. Thus the thermoelectric properties of half-Heuslers with InSb nanoincluions are studied. The samples with nominal composition $Hf_{0.25}Zr_{0.75}NiSn$ with *x* mole InSb (*x* = 0, 0.005, 0.01, 0.012, 0.015, 0.018, 0.02) are prepared. The existence of InSb nanoinclusions in the samples is confirmed by the TEM analysis. Both the carrier concentration and carrier mobility are enhanced with InSb. The carrier concentration is optimized by varying the ratios of InSb. The highest power factor of 55 x 10^{-4} W m^{-1} K^{-2} at above 400 ^{o}C and a peak ZT value of 1.15 is achieved at 700 ^{o}C in the sample with 1.8 mol% InSb. The ZT is 45% higher than the sample without InSb.

Besides, the thermal stability of the $Hf_{0.25}Zr_{0.75}NiSn_{0.99}Sb_{0.01}$ sample is studied. It is always doubtful whether the criteria of thermal stability can be met by nanostructured

materials especially under operating at high temperatures. Thus the thermal stability of the nanostructured half-Heulser compound is studied by annealing in air at 600 ^{o}C for 1 day, 3 days, and 7 days respectively. Although the grain size keeps increasing with annealing time, the thermoelectric properties do not change even after 7 days annealing. Therefore, the high thermal stability of the nanostructured $Hf_{0.25}Zr_{0.75}NiSn_{0.99}Sb_{0.01}$ samples is confirmed.

To search for new potential candidates for thermoelectric applications, other unconventional half-Heusler compositions are studied. With VEC = 19, VCoSb was thought to be a metal, so it's never been studied as a thermoelectric material before. Here, the thermoelectric properties of VCoSb are reported for the first time. Despite the high carrier concentration due to the VEC of 19, the electrical conductivity of VCoSb is not very high since the mobility is low. The Seebeck coefficient around -130 μV/K at 600 °C is abnormally high considering the very high carrier concentration. A peak power factor of 25 μW cm^{-1} K^{-2} and ZT of 0.5 are achieved at 700 °C. By 2% Sn doping at the Sb site or 2% Ti doping at the V site, the ZT value can be further enhanced to 0.56 at 700 ^{o}C.

Finally, two other half-Heuslers VFeSb and YNiSb are studied. The high thermal conductivity and low electrical conductivity of VFeSb limit its ZT only to 0.15. To optimize the thermoelectric performance, cobalt doping at the Fe site is carried out to increase the electrical conductivity and enhanced ZT value is obtained. To suppress the thermal conductivity, alloying Nb at the V is tried. Finally, a peak ZT value of 0.45 at 600 ^{o}C is achieved in the $V_{0.9}Nb_{0.1}Fe_{0.95}Co_{0.05}Sb$ sample. For YNiSb, with a Seebeck coefficient of 85 μV K^{-1} at room temperature, it is found to be p-type. The electrical conductivity of YNiSb is quite low only 0.24 x 10^{-5} S m^{-1} at room temperature, so both

the power factor and ZT is not good. A maximum ZT of only 0.13 is attained at 500 ^{o}C for YNiSb. To enhance the electrical conductivity, the effects of Mg, Co, and Sn doping at the Y, Ni, and Sb site are discussed respectively.

Appendix

List of publications

1. Hao Zhang, Yumei Wang, Keshab Dahal, Jun Mao, Lihong Huang, Qinyong Zhang, Zhifeng Ren, "Thermoelectric properties of n-type half-Heusler compounds $(Hf_{0.25}Zr_{0.75})_{1-x}Nb_xNiSn$", *Acta Materialia* (2016) 113, 41-47.

2. Hao Zhang, Yumei Wang, Lihong Huang, Shuo Chen, Keshab Dahal, Dezhi Wang, Zhifeng Ren, "Synthesis and thermoelectric properties of n-type half-Heusler compound VCoSb with valence electron count of 19", *Journal of Alloys and Compounds* (2016) 654, 321-326.

3. Udara Saparamadu, Jun Mao, Keshab Dahal, **Hao Zhang**, Fei Tian, Shaowei Song, Weishu Liu, "The effect of charge carrier and doping site on thermoelectric properties of $Mg_2Sn_{0.75}Ge_{0.25}$", *Acta Materialia* (2017) 124, 528-535.

4. Lihong Huang, Yumei Wang, Jing Shuai, **Hao Zhang**, Siqi Yang, Qinyong Zhang, Zhifeng Ren, "Thermal conductivity reduction by isoelectronic elements V and Ta for partial substitution of Nb in half-Heusler $Nb_{(1-x)/2}V_{(1-x)/2}Ta_xCoSb$", *RSC Adv*. (2015) 5, 102469-102476.

5. Lihong Huang, Ran He, Shuo Chen, **Hao Zhang**, Keshab Dahal, Haiqing Zhou, Hui Wang, Qinyong Zhang, Zhifeng Ren, "A new n-type half-Heusler thermoelectric material NbCoSb", *Materials Research Bulletin* (2015) 70,773-778.

6. Ran He, Sonika Gahlawat, Chuanfei Guo, Shuo Chen, Tulashi Dahal, **Hao Zhang**, Weishu Liu, Qian Zhang, Eyob Chere, Kenneth White, and Zhifeng Ren, "Studies on mechanical properties of thermoelectric materials by nanoindentation", *Phys. Status Solidi A* (2015) 212, 2191-2195.

7. Weishu Liu, Chuanfei Guo, Mengliang Yao, Yucheng Lan, **Hao Zhang**, Qian Zhang, Shuo Chen, Cyril P. Opeil, Zhifeng Ren, "Bi_2S_3 nanonetwork as precursor for improved thermoelectric performance", *Nano Energy* (2014) 4, 113-122.